Development of a Ground-Based High-Resolution 3D-SAR System for Studying the Microwave Scattering Characteristics of Trees

Justin F. Penner

A thesis submitted to the faculty of
Brigham Young University
in partial fulfillment of the requirements for the degree of

Master of Science

David G. Long, Chair
Brian A. Mazzeo
D. J. Lee

Department of Electrical and Computer Engineering

Brigham Young University

December 2011

ABSTRACT

Development of a Ground-Based High-Resolution 3D-SAR System for Studying the Microwave Scattering Characteristics of Trees

Justin F. Penner

Department of Electrical and Computer Engineering

Master of Science

This thesis presents the development of a high-resolution ground-based 3D-SAR system and investigates its application to microwave-vegetation studies. The development process of the system is detailed including an enumeration of high-level requirements, discussions on key design issues, and detailed descriptions of the system down to a component level. The system operates on a 5.4 GHz (C-band) signal, provides a synthetic aperture area of 1.7 m x 1.7 m, and offers resolution of 0.75 m x 0.3 m x 0.3 m (range x azimuth x elevation). The system is employed on several trees with varying physical characteristics. The resulting imagery demonstrates successful 3D reconstruction of the trees and some of their internal features. The individual leaves and small branches are not visible due to the system resolution and the size of the wavelength. The foliage's outline and internal density distribution is resolved. Large branches are visible where geometry is favorable. Trunks are always visible due to their size and normal-facing incidence surface and their return has the strongest contribution from their base. The imagery is analyzed for dependencies on radar and tree parameters including: incidence angle, signal frequency, polarization, inclusion size, water content, and species. In the current work, a single frequency (5.4 GHz) and polarization (HH) is used which leaves the door open for future analysis to use other frequencies and polarizations. The improved resolution capabilities of the 3D-SAR system enables more precise backscatter measurements leading to a greater understanding of microwave-vegetation scattering behavior.

Keywords: microwave remote sensing, synthetic aperture radar, ground-based SAR, three-dimensional imaging, volume imaging, vegetation, trees

ACKNOWLEDGMENTS

I wish to express appreciation to my advisor Dr. Long for assisting me through the research process and also to Stephen Preston for his dedication and comradery during our partnership in developing the scanner. I also wish to extend special mention to Craig Stringham for writing the post-processing code and for providing technical support for the μASAR; to Don Dawson and Joe Bussio from the EE shop for their involvement in the scanner's mechanical construction; to Joe Winkler for assisting me with tree measurements; to Stephen Carlson for providing the CAD drawings; and to the many students in the MERS lab who lent a hand to transport the scanner. I also wish to express my deepest gratitude to my wife Lindsey for her constant support and love.

Table of Contents

List of Tables

List of Figures

Chapter 1

Introduction

Space-borne and airborne microwave systems provide scientists with powerful tools for studying the health of large ecosystems. These systems provide a non-invasive low-cost solution to acquiring physical measurements of a forest. Studies include: monitoring temporal changes such as deforestation, growth rates, and seasonal patterns [1, 2, 3, 4]; species classification [5, 6, 7]; and estimating physical properties such as biomass, fractional coverage, and forest moisture [3, 8, 9, 10].

These studies may rely on microwave scattering models which accurately describe the microwave-vegetation interactions. Because of the complexity of these interactions, these models rely heavily on empirical data for validation. Currently, most empirical data is acquired from a vegetation canopy using an airborne or space-borne system [11, 12, 13]. This data is 2D and represents backscatter values of a canopy which includes contributions from the leaves, branches, trunks, and underlying soil. A limitation of this data is that the individual inclusions cannot be directly studied and aggregate models are required to determine the relative contributions from each.

In attempt to study the inclusions individually, indoor laboratory experiments have been carried out to obtain direct backscatter measurements on individual leaves and branches [14]. However, this approach provides isolation to the inclusions removing them from their natural environment has some consequences. For instance, multiple reflections between inclusions cannot be observed. Also, a branch segment has a different shape and water content and produces a slightly different re-radiation pattern than that of an intact branch.

Another approach to obtaining empirical data is using three-dimensional synthetic aperture radar (3D-SAR). This is a less common technology but it may have some key strengths for the application of trees. Specifically, it may be capable of resolving the indi-

vidual tree inclusions without removing them from their natural environment. Toward this end, this thesis investigates the option of a high-resolution ground-based 3D-SAR system for studying the scattering characteristics of trees. This research provides answers to the following questions: 1) what are the design requirements of the required imaging system, 2) how effective are 3D reconstruction algorithms on trees, 3) how are the various inclusions represented in SAR imagery, and 4) what does their appearance teach us about the scattering interactions? These answers will provide an increased understanding of microwave-vegetation scattering behavior which in turn will improve vegetation studies.

1.1 Previous Studies

As mentioned earlier, the success of many vegetation studies rely on the availability of empirical data to validate vegetation scattering models. The following discussion describes some common modeling approaches as well as attempts to validate these models using empirical data.

A simple vegetation model is a water-cloud model which is described by Attema [15]. In this model the vegetation volume is assumed to consist of a collection of small water droplets that are identical in size and uniformly distributed. This model assumes that the scattering and absorption properties of the vegetation volume are strongly related to its volumetric water content, m_v. This model is considered semi-empirical because it does provide a total physical description of the vegetation but instead relies on regression analysis to determine relationships between m_v and scattering and extinction cross-sections. Thus, the availability of good empirical data is critical for the accuracy of this model.

A more descriptive model is proposed by Karam [11]. This model works on a vegetation canopy and decomposes it into three layers: a crown layer, a trunk layer, and an irregular ground surface. The crown layer consists of branches modeled as finite-length cylinders grouped into different sizes each with an orientation distribution and leaves modeled as randomly oriented dielectric discs. The trunk layer consists of randomly positioned and vertically oriented cylinders. The model also accounts for multiple reflections between the ground, trunk, and crown. The author validates his model using data of a walnut orchard from the NASA Earth Observing System (EOS) [16]. He compares the EOS data against

his model-calculated values of normalized radar backscattering cross-section (σ^0) which are determined by taking physical measurements from the orchard (measurements include inclusion size, permittivity, orientation, and density) and using them as inputs to his model. While his results are good, the comparison is limited since the EOS data only provides 2D σ^0 measurements of the canopy and not of the individual inclusions or layers.

In some instances, backscatter measurements are performed on individual leaf or branch samples, often inside an an anechoic chamber [14]. In another study, Karam collects backscatter measurements on an isolated leaf and an isolated branch segment [17]. These measurements are outdoors at an unobstructed site where an antenna is directed vertically upward at the target (supported by nylon threads) which eliminates interference from neighboring obstructions. The targets used for measurements are an aspen leaf and a birch branch segment. For validation, Karam uses leaf and branch backscatter models developed by Allan and McCormick [18]. Since this measurement setup provides isolation to individual vegetation inclusions, it offers more precise model validation than canopy measurements. One disadvantage is that a branch segment has a different geometry than a full intact branch which is likely to result in a different scattering pattern. Also, this setup does not allow for multiple reflections between inclusions to be observed.

1.2 Contributions of this Work

This thesis documents the development of a high-resolution ground-based 3D-SAR system. A semi-formal development process is followed and described. High-level requirements are laid out, design decisions are justified, and a comprehensive system description is provided down to the component level. In addition to its involvement in the current work, this system has been used to study snow-pack as detailed in Stephen Preston's thesis [19], and is available for future research projects relating to 3D microwave imaging.

This thesis contributes to the body of published work on microwave-vegetation remote sensing. Whereas the majority of the aforementioned work is 2D in nature, the data provided in this work is 3D and at higher resolution than most previous studies. The additional resolution provides insight into the vegetation scattering process to enable more precise backscatter measurements which can then be used to improve models.

1.3 Outline of this Document

This thesis is organized into seven chapters. Chapter 2 provides some background information radar systems including introductions to basic radar and synthetic aperture radar (SAR).

Chapter 3 describes some of the basic microwave scattering characteristics of vegetation. Due to the geometric complexity of vegetation, describing the scattering interactions exactly is unrealistic. Instead, approximate models are use to simplify the vegetation's physical attributes and common models are discussed.

Chapter 4 provides documentation for the ground-based 3D scanner system and describes the development process including high-level requirements, basis for important design decisions, and thoughts on alternate implementations. This chapter serves two purposes. One is to provide the general reader with an understanding of the system which is responsible for generating the imagery presented in the following chapters. The second purpose is to provide the relevant documentation for future developers to continue with development without having to repeat process.

Chapter 5 describes the tree scattering experiments conducted in August 2010. Topics include tree selection, conducting the experiments, post-processing, and image preparation and presentation. At the end, an overview of the generated 3D imagery is given.

Chapter 6 provides an analysis of the tree imagery generated from the four experiments described in Chapter 5. In this analysis, the scattering characteristics of the vegetation are investigated including the representations of the different vegetation parts, including the leaves, branches, and trunk; and also the attenuation behavior of the foliage volume. Another objective of this chapter is to verify the radar scanner's reliability. Since the system is a new build and has had little formal testing, these results indicate that the system is operating correctly.

Chapter 7 summarizes the results of this thesis including strengths and limitations and suggests future research to be done in this area.

Chapter 2

Principles of Basic Radar and Synthetic Aperture Radar

This chapter provides background information on radar systems beginning with an introduction to basic radar and followed by an introduction to synthetic aperture radar (SAR).

2.1 Principles of Basic Radar

The discussion on basic radar begins with a generalized description of a basic radar system including its basic function, components, and coordinate system. Following, discussion are given to range measurements, range resolution, angular beam pattern, angular resolution, and the radar equation.

2.1.1 A Basic Radar System

In simplified terms, a radar system transmits pulses of electromagnetic energy and measures the returned echoes. The transmitted pulses interact with a scatterer (or scatterers). Some of the energy is absorbed by the scatterer while the rest is dispersed, or scattered, in many directions. From the portion of signal returned to the receiver, the radar can derive information about the scatterer including range, velocity, direction, and reflectivity.

A radar uses a spherical coordinate system as shown in Fig 2.1. In this coordinate system, the antenna look direction is along the $+x$ axis. This axis corresponds to *range*. Similarly, the y and z axes correspond to *azimuth* and *elevation* respectively. The angle ϕ is called *azimuth angle* while θ is called *elevation angle*.

The radar in this figure represents a *monostatic* configuration since the transmitter and receiver are collocated. In this configuration, the transmitting and receiving duties may be performed by a single antenna (as is the case in the figure) or by two collocated

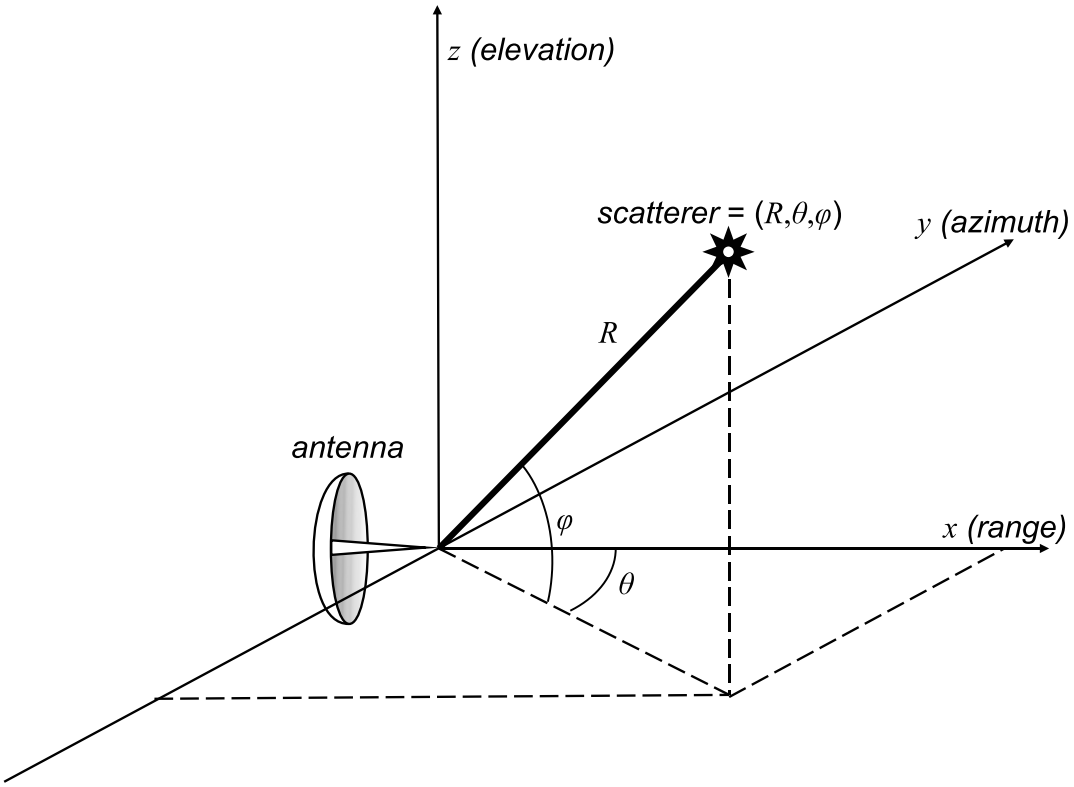

Figure 2.1: Spherical coordinate system for radar measurements

antennas (sometimes referred to as *pseudo-monostatic*). Conversely, a radar which comprises a transmitter and receiver which are separated by an appreciable distance is called a *bistatic* radar.

2.1.2 Ranging

The most fundamental function of radar, implied by its name—radio detection and ranging (Radar)—is ranging. The range R to a target is by measured by the transmitted signal's time of flight t to the target and back to the receiver. This calculation is possible because the velocity of electromagnetic energy is known to be the speed of light c. The range is given by

$$R = ct/2. \tag{2.1}$$

The factor of two in the equation is a result of the two-way path of the signal.

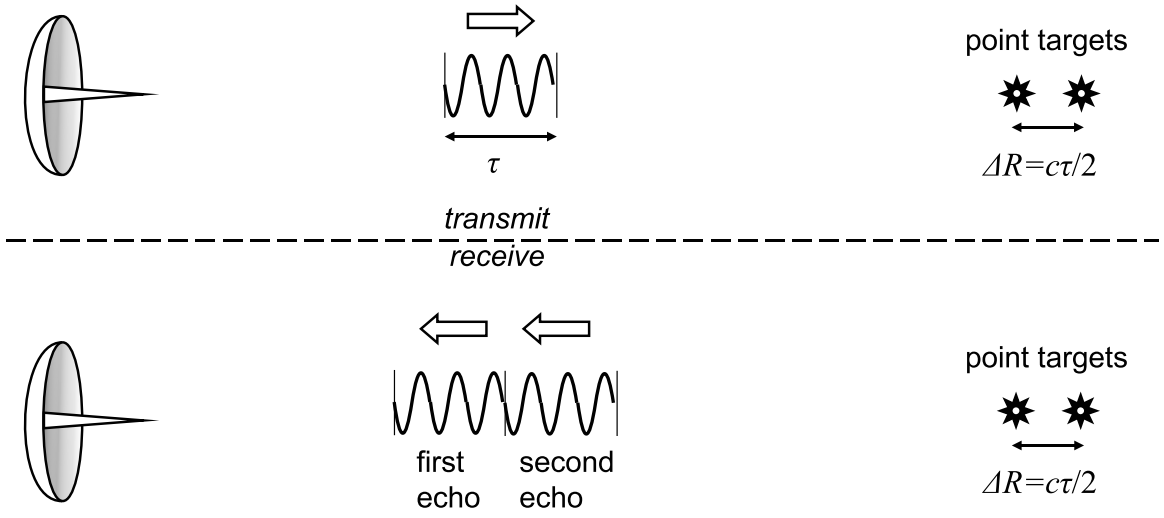

Figure 2.2: Geometry for describing conventional pulse range resolution

2.1.3 Range Resolution

The precision of a range measurement is called *range resolution* and is determined by the length of the transmitted pulse τ in pulse modulated systems or, the frequency bandwidth β in frequency modulated systems.

In the case of pulse modulation, if two targets are too closely spaced, their return echoes overlap and the radar is unable to separately resolve them. This idea is illustrated in Figure 2.2. If a pulse is transmitted towards two scatterers separated by a distance of $c\tau/2$, the trailing edge of the echo pulse from the near scatterer arrives at the receiver at the same time as the leading edge of the echo pulse from the far scatterer. This is considered the minimum requirement to resolve two scatterers in range. Thus, range resolution in a pulse modulated system is defined by

$$\Delta_R = \frac{c\tau}{2}. \tag{2.2}$$

In the case of frequency modulation, range resolution is given by

$$\Delta_R = \frac{c}{2\beta} \tag{2.3}$$

where β is the system bandwidth. Eqs. (2.2) and (2.3) are related by $\tau = 1/\beta$.

2.1.4 Antenna Gain Pattern

A radar uses a *directional antenna* (or *beam antenna*) to increase performance and reduce interference from unwanted sources. With a directional antenna, the transmit signal is channeled through an aperture which causes the signal to spread out in a diffraction pattern referred to as the *antenna gain pattern*. The gain pattern is shown in Fig. 2.3: in (a) it is represented in real space and in (b) it is plotted as a function of off-axis angle. Notice that the majority of the energy is centered on zero degrees. This consolidation of energy is referred to as the *main lobe*. The smaller lobes on the both sides and are referred to as *side lobes*. The existence of these side lobes creates an opportunity for ambiguities to arise in target location.

The width of an antenna's beam, or *beamwidth*, is defined formally as either θ_{nn}, the angle between the first nulls or θ_{3dB}, the angle between the two 3 dB points of the main lobe. An approximation for the 3 dB beamwidth is $0.89\lambda/D_{\text{ant}}$ radians [20], where D_{ant} is the width of the antenna; however, the factor of 0.89 is often dropped and antenna beamwidth is approximated by

$$\theta_{\text{3dB}} \approx \lambda/D_{\text{ant}}. \tag{2.4}$$

Thus antenna beam width is a function of the ratio between the wavelength and aperture size.

2.1.5 Angular Resolution

Angular resolution in a basic radar system is a function of beamwidth and range. This concept is illustrated in Fig. 2.4. Here, a radar beam creates a rectangular footprint on the ground (or target plane) which represents a resolution cell. The dimensions of the footprint define azimuth resolution Δ_{AZ} and elevation resolution Δ_{EL} given by

$$\Delta_{\text{AZ}} = R\,\phi_{\text{3dB}}, \tag{2.5}$$

$$\Delta_{\text{EL}} = R\,\theta_{\text{3dB}}. \tag{2.6}$$

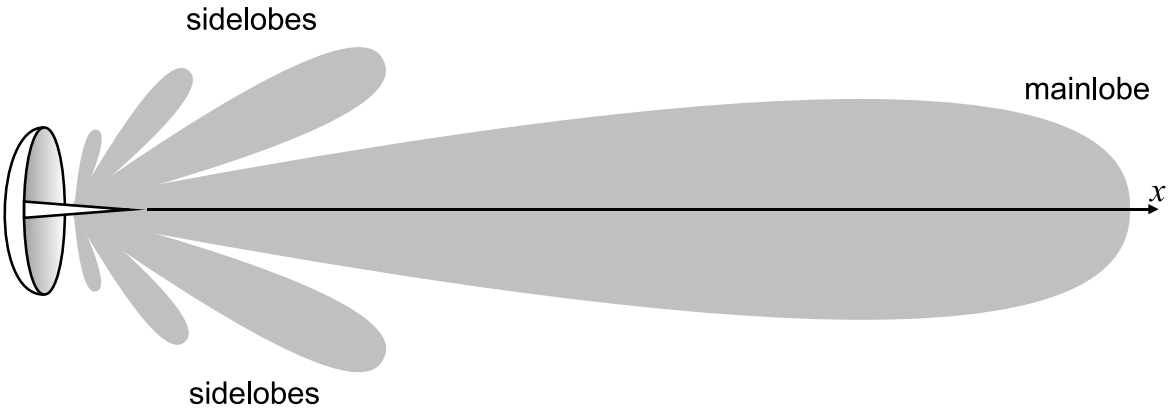

(a) Antenna gain pattern (a) illustrated in real space.

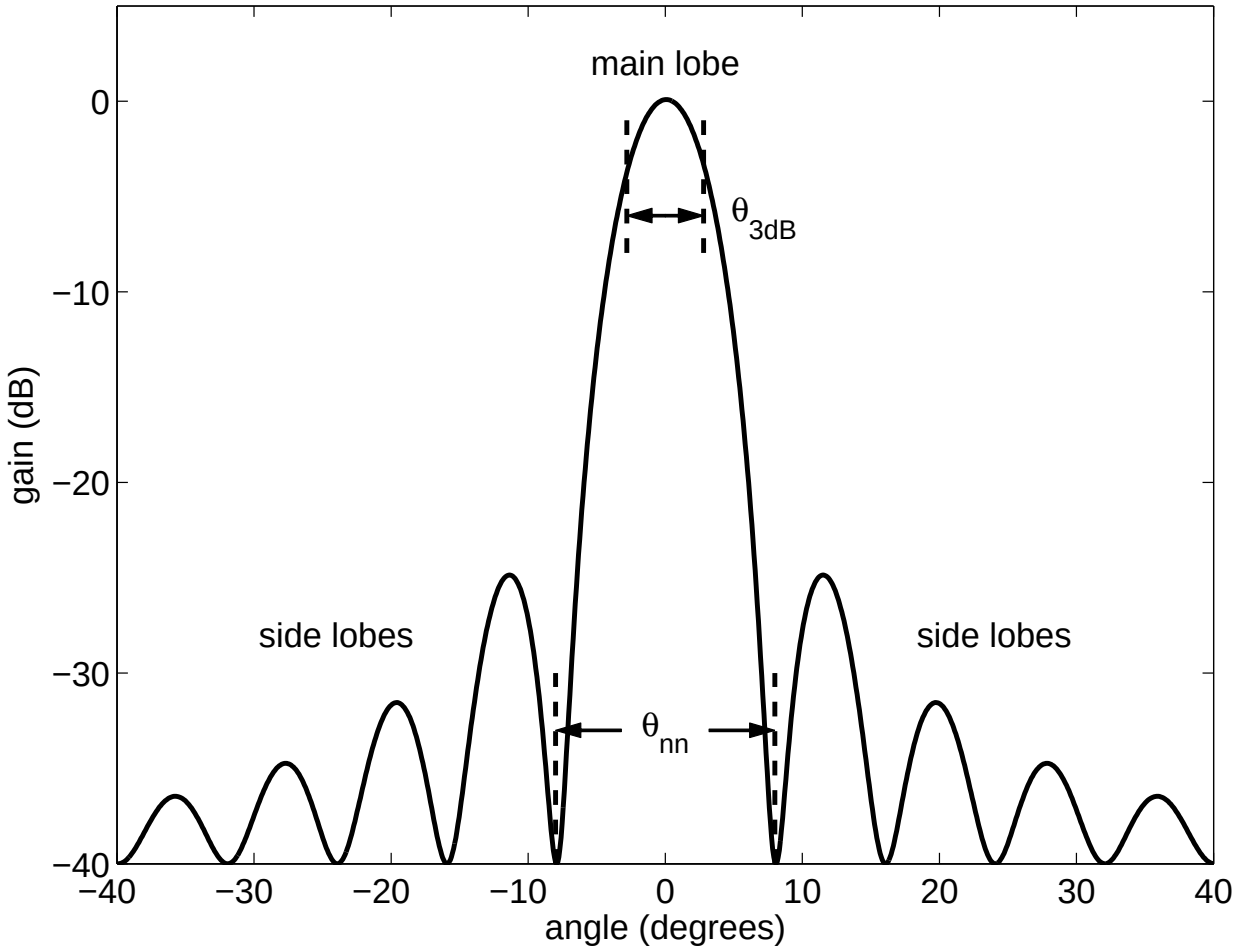

(b) Antenna gain pattern plotted as a function of degrees. Beamwidths $\theta_{3\text{dB}}$ and θ_{nn} are illustrated.

Figure 2.3: Antenna gain pattern (a) illustrated in real space and (b) plotted as a function of elevation angle

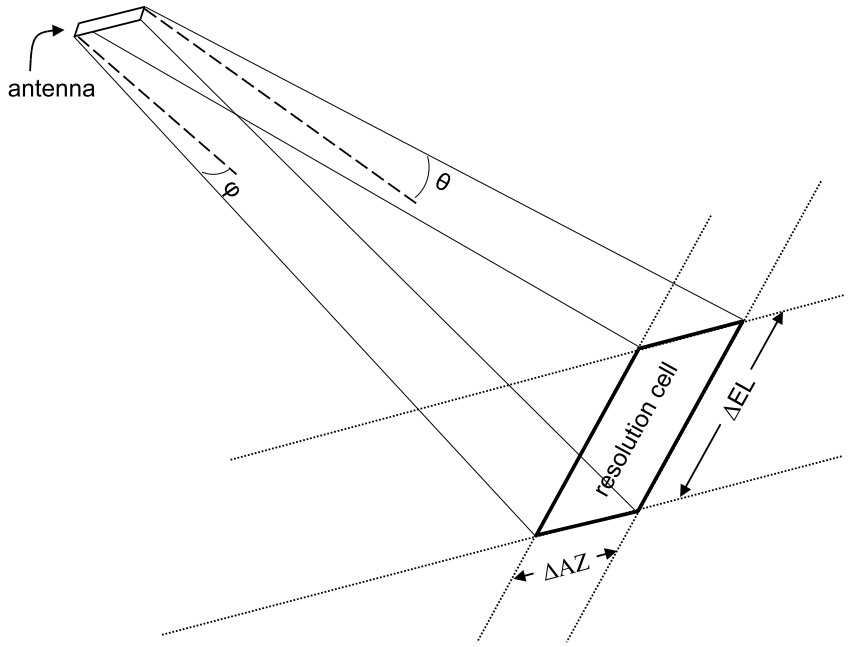

Figure 2.4: Illustration of angular resolutions Δ_{AZ} and Δ_{EL}

Since the values of Δ_{AZ} and Δ_{EL} are dependent on range, they can become very large if R is large, which implies that resolution degrades with increased range.

2.1.6 The Radar Equation

The power transfer between the radar and scatterer is described by the radar equation:

$$P_r = \frac{P_t A_r G_t \sigma}{(4\pi R^2)^2}. \tag{2.7}$$

This equation can be conceptualized by decomposing it into separate terms—Fig. 2.5 provides an illustration. An electromagnetic signal with power P_t is put through a directional antenna with gain G_t. It travels a distance of R_t to the scatterer, incurring a spreading loss of $1/4\pi R_t$. A fraction of the signal, based on the scatterer's radar cross-section σ (see Chapter 3), is reradiated back toward the radar, travels a distance R_r, and incurs a second spreading loss of $1/4\pi R_r$. Finally, a fraction of the reradiated signal is intercepted by the receiver with aperture size A_r. In the case where the transmitter and receiver are collocated, R_t and R_r

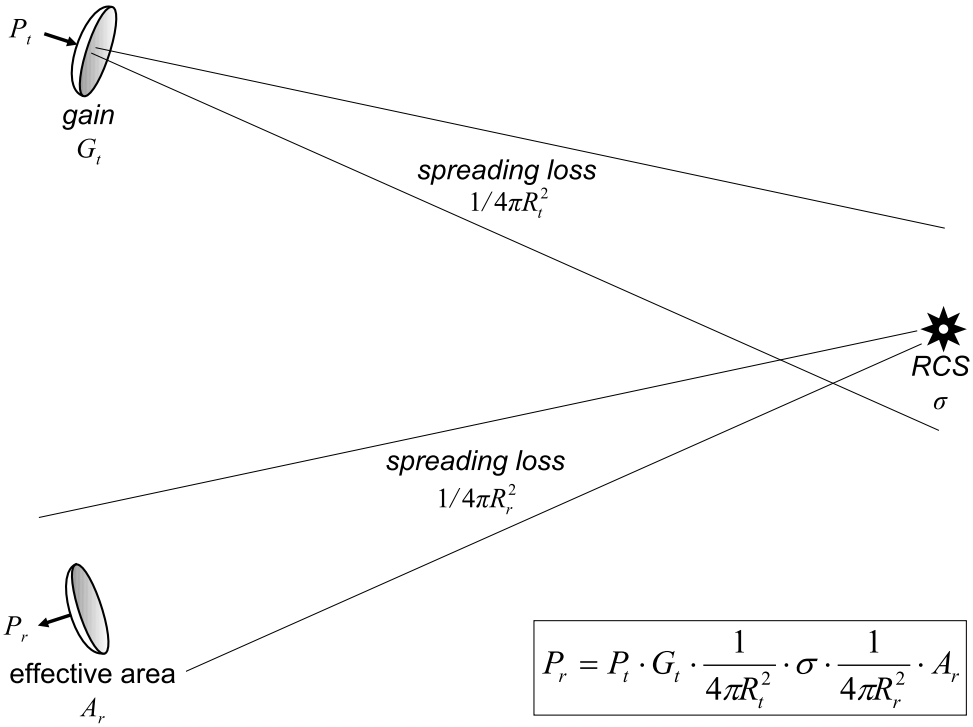

Figure 2.5: Illustration of the radar equation

can be made equal (R). This version of the radar equation applies to a discrete scatterer and assumes no attenuation losses.

2.2 Principles of Synthetic Aperture Radar

Synthetic aperture radar (SAR) is known for generating high-resolution imagery and has many applications of environmental imaging such as deforestation, crop growth, ice flows, and oil spills. SAR achieves high resolution by integrating target observations from a variety of angles. The name *synthetic aperture* comes from the idea that the collection of measurements from different antenna positions can be combined to simulate, or *synthesize*, a much larger antenna. As a result, SAR gains the benefits of a large radar, including a narrow beam and high resolution, but without the costs of constructing, operating, and powering a large system.

2.2.1 SAR Data Collection

SAR data collection entails combining backscatter samples from a variety of antenna positions. The span of samples (or antenna positions) is referred to as the synthetic aperture D_{sar} and the distance between samples is referred to as the spatial sampling period D_s. D_{sar} and D_s are illustrated in Fig. 2.6 along with the overall geometry of the data collection scheme. This particular configuration represents 2D SAR since it consists of a single scanning axis. For 3D SAR, the sampling pattern is a 2D grid.

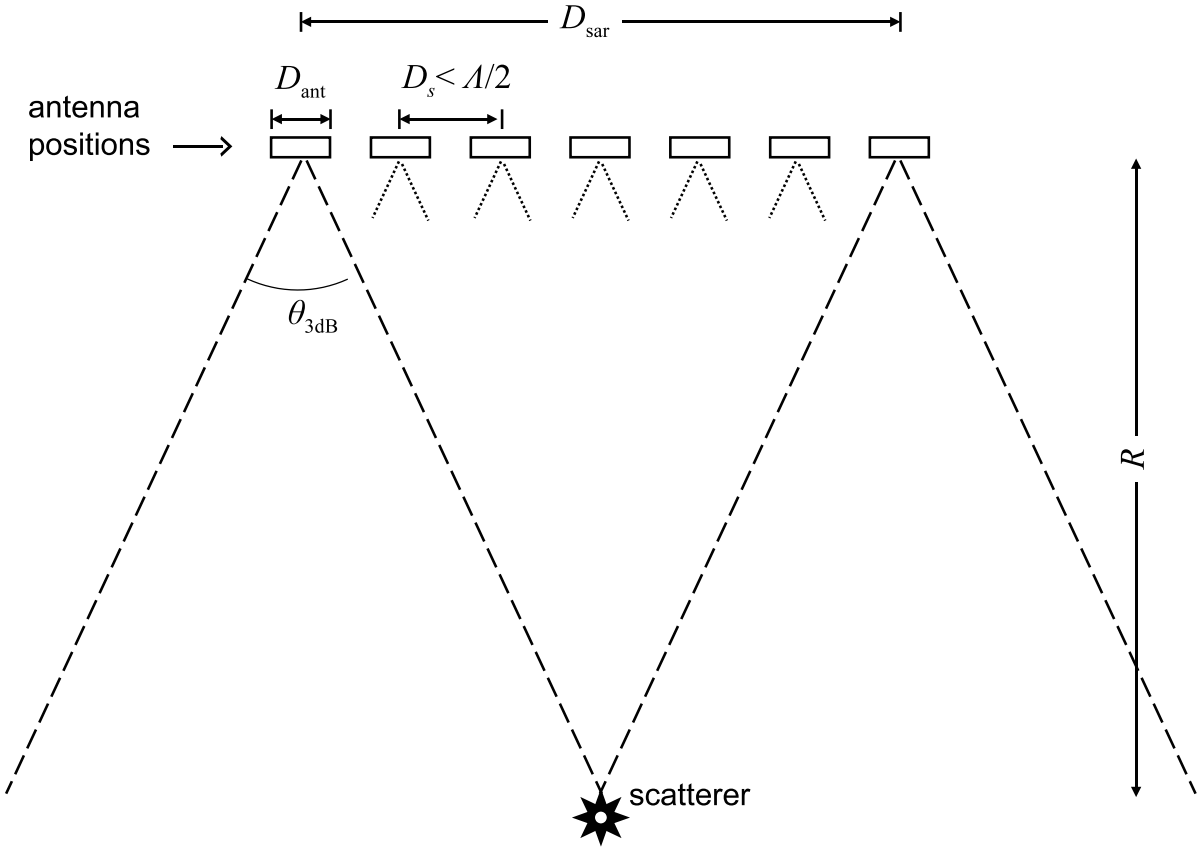

Figure 2.6: Illustration of the SAR data collection process. D_{sar} is the synthetic aperture (span of antenna observations), D_s the is sampling period (distance between antenna observations), and D_{ant} is the physical antenna size.

Spatial Sampling and the Sampling Theorem

SAR data collection employs spatial sampling. Sampling is commonly understood in terms of temporal sampling, but the same principles apply to spatial sampling. While temporal sampling refers to sampling varying in time, spatial sampling refers to sampling varying in position.

The Nyquist sampling theorem (or just *sampling theorem*) states that for a continuous signal to be sampled and remain completely determined, it must be sampled at a frequency higher than twice the highest frequency present in the signal. In terms of the sampling period, this implies

$$D_s < \frac{\Lambda}{2}. \tag{2.8}$$

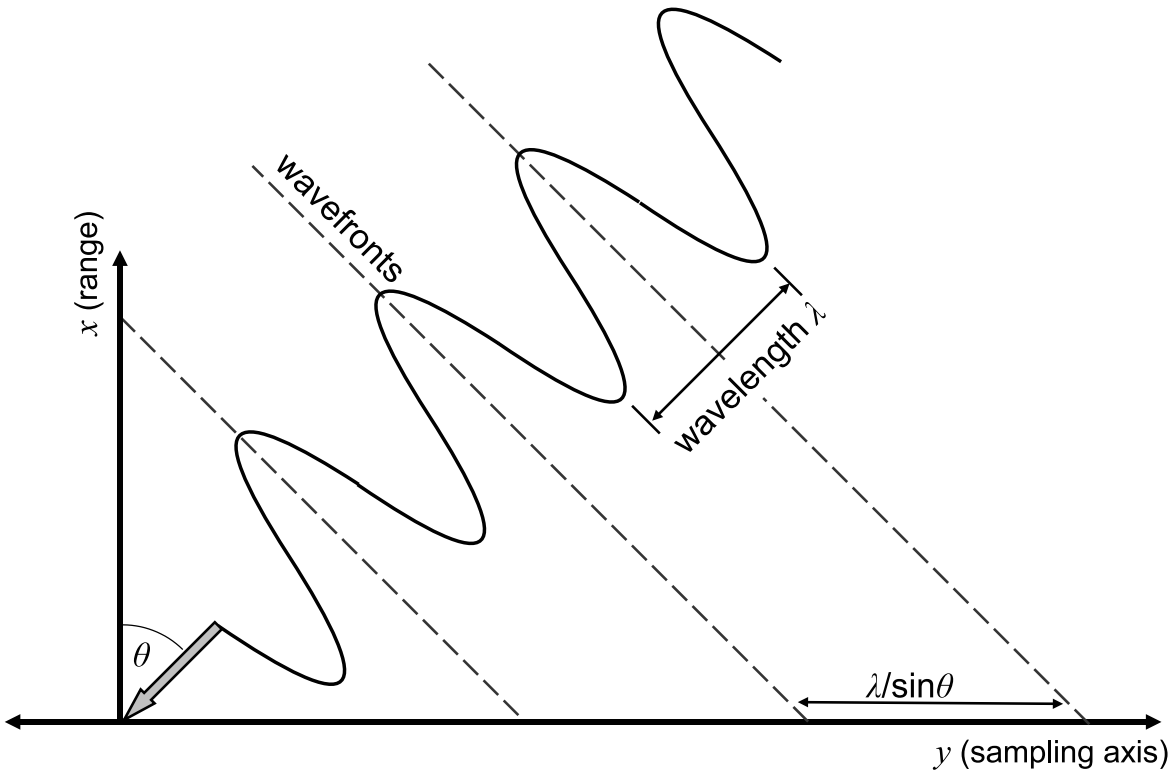

Figure 2.7: Sampling period is $\lambda / \sin\theta$ when sampling axis is not parallel to the traveling wave. Y-axis is sampling axis and x-axis is to range.

where Λ corresponds to the highest frequency in the signal. The price of sampling at a lower frequency is aliasing. In terms of spatial sampling, this means that a target could appear to be at multiple locations in space. To avoid aliasing, we must sample at the Nyquist frequency or higher.

When the sampling axis is not parallel to the traveling wave, the maximum sampling period D_s must be modified slightly. Consider Fig. 2.7, in which the y-axis corresponds to the antenna sampling axis, the x-axis corresponds to range, and the traveling sinusoid corresponds to a scatterer reflection. In this scenario, the sampling period is constrained by

$$D_s < \frac{\Lambda}{2 \cdot 2 \cdot \sin(\theta_{3\text{dB}}/2)} \tag{2.9}$$

where $\theta_{3\text{dB}}$ is the beamwidth and $\theta_{3\text{dB}}/2$ is intended to represent the maximum incidence angle. In comparison with Eq. (2.8), this equation adds a sine term and a factor of 2 which accounts for the signal's two-way path.

After applying the small angle approximation and substituting in Eq. (2.4), Eq. (2.9) becomes

$$D_s < \frac{D_{\text{ant}}}{2}. \tag{2.10}$$

This relationship provides a simplistic rule of thumb for SAR sampling. It states that a maximum sampling period of less than half the size of the antenna is necessary to avoid aliasing.

2.2.2 SAR Data Processing

SAR data processing refers to the process of converting the raw backscatter samples into imagery. This process includes range compression, range interpolation, and an image reconstruction algorithm called backprojection.

Range compression means processing the raw backscatter data to extract range information. Range interpolation means interpolating the range data into specific range measurements. Some interpolation strategies include linear, cubic, and sinc. Using sinc interpolation, range compression and interpolation are performed simultaneously by: multiplying

the raw echoes by the time-shifted transmit pulse, low-pass filtering, zero-padding, and then performing a Fourier Transform [21].

A commonly used algorithm known as backprojection is employed to reconstruct the range compressed SAR data into multi-dimensional imagery. While this algorithm is computationally intensive, it makes no assumptions about the sampling path and as a result, it can be used for a variety of SAR applications including 3D SAR. To understand backprojection conceptually, imagine that a target has many 1D projections, each of which represents a particular antenna observation. In this algorithm, each of these projections are smeared back, or *projected back*, onto the target space and the sum of these smearings reconstruct the original target.

For a pixel located at (x_s, y_s, z_s), the SAR backprojection algorithm can be expressed as [21]

$$A(x_s, y_s, z_s) = \sum_n P(r[n]; n) e^{\Phi_e(r[n])} \tag{2.11}$$

where $A(x_s, y_s, z_s)$ is the complex pixel power, $r[n]$ is the distance from antenna position for pulse n to scatterer location (x_s, y_s, z_s), $\Phi_e(r[n])$ is the expected phase for range $r[n]$, and $P(r[n]; n)$ is the ranged-compressed SAR data interpolated to slant range $r[n]$.

The expression for $r[n]$, the antenna-scatterer distance, is

$$r[n] = \sqrt{(x[n] - x_s)^2 + (y[n] - y_s)^2 + z_s^2} \tag{2.12}$$

where $x[n]$ and $y[n]$ correspond to the antenna position for pulse n where $z[n]$ is assumed to be zero.

The expression for $\Phi_e(r[n])$, the expected phase, is

$$\Phi_e(r[n]) = j4\pi r[n]/\lambda \tag{2.13}$$

where $\lambda = c/f_0$ with c the speed of light and f_0 the radar center frequency.

Equation (2.11) is applied to each pixel in the target space. In 2D SAR, the target space is a surface (typically the ground) measured in dimensions of range and azimuth. In

3D SAR, the target space is a 3D volume in real space measured in dimensions of range, azimuth, and elevation.

2.2.3 SAR Resolution

Traditional SAR systems provide resolution in two dimensions: range and azimuth. Azimuth refers to the direction parallel to the movement of the antenna; in the case of an airplane, this is parallel to the flight path. 3D SAR adds resolution in the elevation.

SAR range resolution is the same as from a basic system since it solely depends on the signal bandwidth. However, there is a subtle difference between range resolution and the resolution that appears in a 2D image. Since the antenna on an aircraft points to the ground at an angle, the distance in true range (or *slant range*) differs from the distance in *ground range* by a sine factor. Specifically, the resolution in ground range is given by

$$\Delta_{Rg} = \Delta_R / \sin\theta \tag{2.14}$$

where θ is the incidence angle.

Azimuth resolution, on the other hand, is obtained differently. Recall that from a basic system, angular resolution is defined by $\Delta_{\mathrm{AZ}} = R/\phi_{\mathrm{3dB}}$. This equation still applies to SAR resolution, but with ϕ_{3dB} replaced by ϕ_{sar}. This new beam width ϕ_{sar} results from the large synthetic aperture created by the antenna's scan length D_{sar}

$$\phi_{\mathrm{sar}} = \lambda D_{\mathrm{sar}}.$$

Thus, azimuth resolution is given by

$$\Delta_{\mathrm{AZ}} = R\phi_{\mathrm{sar}}. \tag{2.15}$$

Similarly, elevation resolution in 3D SAR is given by

$$\Delta_{\mathrm{EL}} = R\theta_{\mathrm{sar}}. \tag{2.16}$$

SAR systems have an interesting quality in that their resolution performance does not degrade with increased range, so long as adequate sampling is performed. Adequate sampling means that (1) the target is illuminated by the entire beam width and (2) the spatial sampling frequency observes the sampling theorem. Why SAR resolution remains unaffected by increased range is explained by two opposing factors: (1) the spreading of the antenna beam which causes a decrease of resolution and (2) the increased exposure time of a target to the antenna beam which causes an increase of resolution. The second factor is further explained by the following logic: an increase of exposure time allows for more observations, which implies a larger synthetic aperture and a narrower synthetic beam leading to a positive effect on resolution. As a rule of thumb, SAR resolution, under these conditions, can be approximated by half the antenna size [20]

$$\Delta_{\mathrm{AZ}} \approx D_{\mathrm{ant}}/2. \tag{2.17}$$

In practice, however, it is difficult to maintain the same resolution at very far ranges due to of SNR considerations. As separation from the target increases, spreading loss increases and a larger antenna (D_{ant}) is required to maintain an adequate SNR. Even so, some SAR-equipped orbiting spacecraft (which are hundreds of kilometers above the earth) manage to produce high-quality imagery with resolution of only a few meters [22].

2.2.4 Imaging

Radar imagery shares some similarities to optical imagery, but also has many fundamental differences (see Figure 2.9 for a side-by-side comparison of an airborne SAR image and an optical image). Some of the main differences are enumerated in the following list.

1. Optical imaging generally relies on external sources of illumination such as the sun (passive sensing); while radar imaging provides its own source of illumination (active sensing). As a result, radar systems function just as well in day or night.

2. The lower frequencies used by radar enable penetration through clouds, rain and in some cases, even vegetation canopies and earth. This enables a radar system to operate during inclement weather conditions or to observe targets obstructed from optical view.

3. While the resolution achieved by SAR systems is considered very good for radar technology, optical systems are capable of much higher resolution.

4. An optical image uses an angular perspective which results in certain geometric distortions such as an object appearing to be smaller with increased distance. A radar image, on the other hand, uses a rectangular perspective with a different distortion geometry.

5. A microwave system obtains range measurements inherently while an optical system must do so via multiple looks.

6. These systems use different regions of the electromagnetic spectrum which result in different scattering characteristics. Microwave wavelengths range from about 1 mm to 1 m while optical wavelengths range from about 390 to 750 nm.

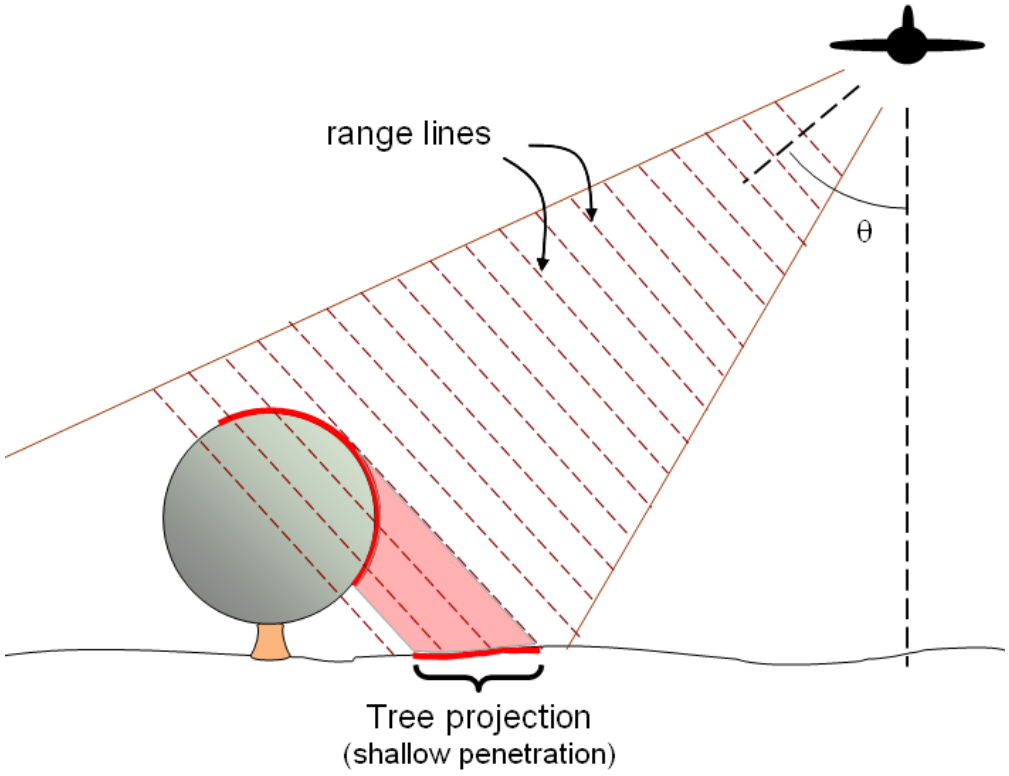

Figure 2.8: Illustration showing acquisition geometry and target layover for airborne-SAR. The airborne platform views the target from an elevated incidence angle of θ. The illuminated portion of the target is projected along the range lines onto the ground.

(a) SAR X-band image

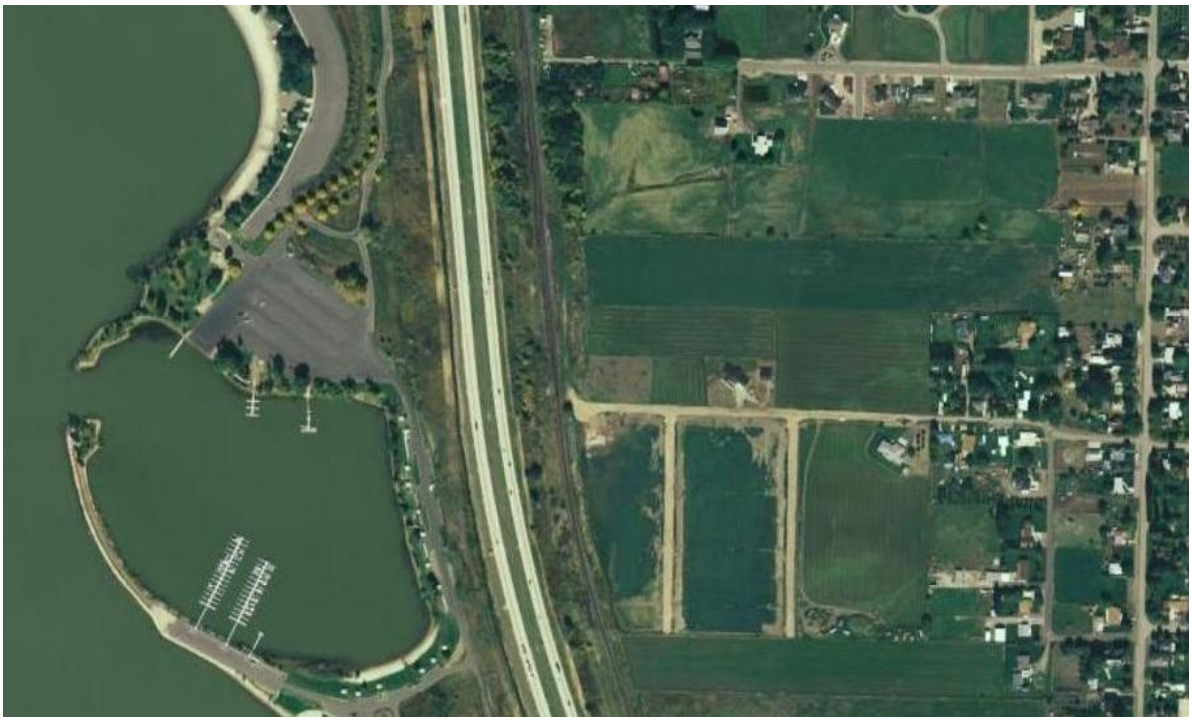

(b) Optical image

Figure 2.9: SAR and optical images of Willard Bay, UT. Area covers 0.85 x 1.35 km with north pointing up. Willard Bay Reservoir on left of image, houses and vegetation on the right, and the I-15 highway in between. (a) SAR image acquired from airborne platform at elevation of 1000 m, incidence angle of 50°, and frequency of 5.4 GHz. (b) Optical image from Google Earth.

2.2.5 Summary

This section has provided an overview of some basic radar principles and an introduction to Synthetic Aperture Radar. SAR data collection entails the integration of backscatter samples from a variety of antenna positions. Generation of a 2D image requires sampling across a single axis while generation of a 3D image requires sampling across a 2D grid. To avoid aliasing, a sampling period of less than half the size of the antenna is necessary.

An data processing algorithm called backprojection was described. This algorithm is computationally intensive but it makes no assumptions about the sampling path and as a result, it is suitable for a variety of SAR applications including 3D SAR.

The resolution capabilities of a SAR system were discussed. It was shown that range resolution is the same as from a basic system since it solely depends on the signal bandwidth; however, resolutions in azimuth and elevation are obtained differently and are vastly improved compared to a real aperture system.

At the end of the chapter, a comparison was made between a SAR and optical imaging technologies. Optical systems have higher resolution but a key advantage of SAR is that it can operate during day, night, or inclement weather conditions.

Chapter 3

Microwave Scattering from Vegetation

This chapter describes some of the basic microwave scattering characteristics of vegetation. Due to the geometric and dielectric complexity of vegetation, describing the scattering interactions exactly is unrealistic. Instead, approximating models are use to simplify the vegetation's physical attributes. For example, leaves can be modeled as dielectric discs and branches as cylinders. Applying microwave scattering fundamentals to these simplified geometries provides some intuition to some of the key microwave-vegetation interactions. These interactions are of interest in Chapter 6 when the 3D SAR imagery is interpreted.

Section 3.1 begins with an introduction to general microwave scattering. This includes discussions on the scattering for different types of targets. Specifically, scattering is discussed for a solid object, a surface, and a homogeneous volume. Section 3.2 provides an overview of popular vegetation microwave scattering models. Most models are classified as physical or semi-empirical. Physical models relate σ^0 to the physical properties of the vegetation which can include water content, density, and inclusion shape and size. Leaves, branches, and trunks are modeled with simplified geometries. Section 3.3 discusses the dielectric properties of leaf and branch material. Finally, Section 3.4 provides a conceptual (non-mathematical) description of the scattering characteristics of each of the vegetation parts. Due to insufficient resolution in radar systems, leaves and small branches must be studied collectively and their scattering behavior is described by volume scattering. On the other hand, trunks and large branches may be individually resolvable, in which case their scattering behavior is described by discrete-target scattering and surface scattering.

3.1 Introduction to Microwave Scattering

When electromagnetic energy moves from one medium to another, it undergoes scattering. Scattering consists of reflections, refractions, and particle scattering. The primary factors influencing the scattering behavior of a medium are its geometric and electrical characteristics.

Geometric characteristics that have a significant influence on scattering behavior include size, shape, orientation, and roughness. Size often determines the spreading of the returned reflections. For a large target, where the incident surface is relatively flat and large in comparison to the wavelength, the re-radiation pattern is angularly narrow and considered specular. These specular returns have high backscatter if the incident surface is normal facing. If a target is very small, reflections are broad and its other geometric characteristics have little effect at non-zero incidence angles. Surface roughness increases scattering (see Section 3.1.3 for further discussion on roughness).

The electrical characteristics of a medium work closely with its geometric characteristics to determine the scattering behavior. One measure of an object's electrical character is the complex dielectric constant ε also known as its permittivity. This parameter is an indication of the reflectivity and conductivity of various materials and is frequency dependent. For microwaves, most natural media have permittivities in the range 3 to 8 when dry. On the other hand, water has a dielectric constant of approximately 80. Thus, the presence of moisture in either soil or vegetation can significantly alter radar backscatter. Changes in backscatter strength from one medium to another are often linked to changes in moisture content much more closely than they are to changes in the media themselves. Because vegetation has large surface areas and often has high moisture content, it is a particularly good reflector of radar energy.

3.1.1 Scattering Terms

The power transfer involved in a scattering transaction is described by

$$P_i = P_a + P_s + P_t$$

where P_i is incident power, P_a is absorbed power, P_s is scattered power, and P_t is transmitted power.

Using the variable x to represent a, s, or t, some additional scattering terms are put forth. The efficiency factor ξ_x is a unit-less ratio between P_x and P_i and is given by

$$\xi_x = P_x/P_i.$$

The cross-section K_x is the *effective* size of a discrete target measured in m^2 and is given by

$$K_x = \xi A_p$$

where A_p is the physical cross-section of the target.

The coefficient κ_x is the *effective* size of a distributed target which is normalized to one unit area for a surface target ($\mathrm{m}^2\mathrm{m}^{-2}$) or one unit volume for a volume target ($\mathrm{m}^2\mathrm{m}^{-3}$). It is given by

$$\kappa_x = K_x\rho$$

where ρ is the target density.

The backscattering cross-section σ is the *effective* size of a discrete target from the perspective of the receive antenna and is given by

$$\sigma = K_s(P_{back})4\pi R^2$$

where P_{back} is the power scattered in the direction of the receive antenna and R is the target range. The purpose of the $4\pi R^2$ term is to provide normalization to an isotropic scatterer. σ is also referred to as *radar cross-section.*

The backscattering coefficient, or *normalized backscattering cross-section*, σ^0 is similar to σ, but is used in the case of a distributed target. It is has units of $\mathrm{m}^2\mathrm{m}^{-2}$ for a surface target or $\mathrm{m}^2\mathrm{m}^{-3}$ for a volume target and is given by

$$\sigma^0 = \sigma\rho.$$

3.1.2 Discrete-Target Scattering

We now consider the scattering from a solid object—first considering a sphere. There are three regions of electromagnetic scattering based on a dimensionless size parameter χ which is defined as $\chi = 2\pi_r/\lambda$. These three regions include Rayleigh, resonance, and geometric (or optical) and are shown in Fig. 3.1 for a conducting sphere where backscattering efficiency $\xi_b = \sigma/\pi r^2$ is plotted against χ. The general behavior is similar for targets of other shapes and conductivities.

In the Rayleigh region ($\chi << 1$) the scattering bodies are particle-like and only have a small interaction to the electromagnetic field. Instead of giving reflections, the particles experience an induced internal electric field which gives rise to secondary radiation.

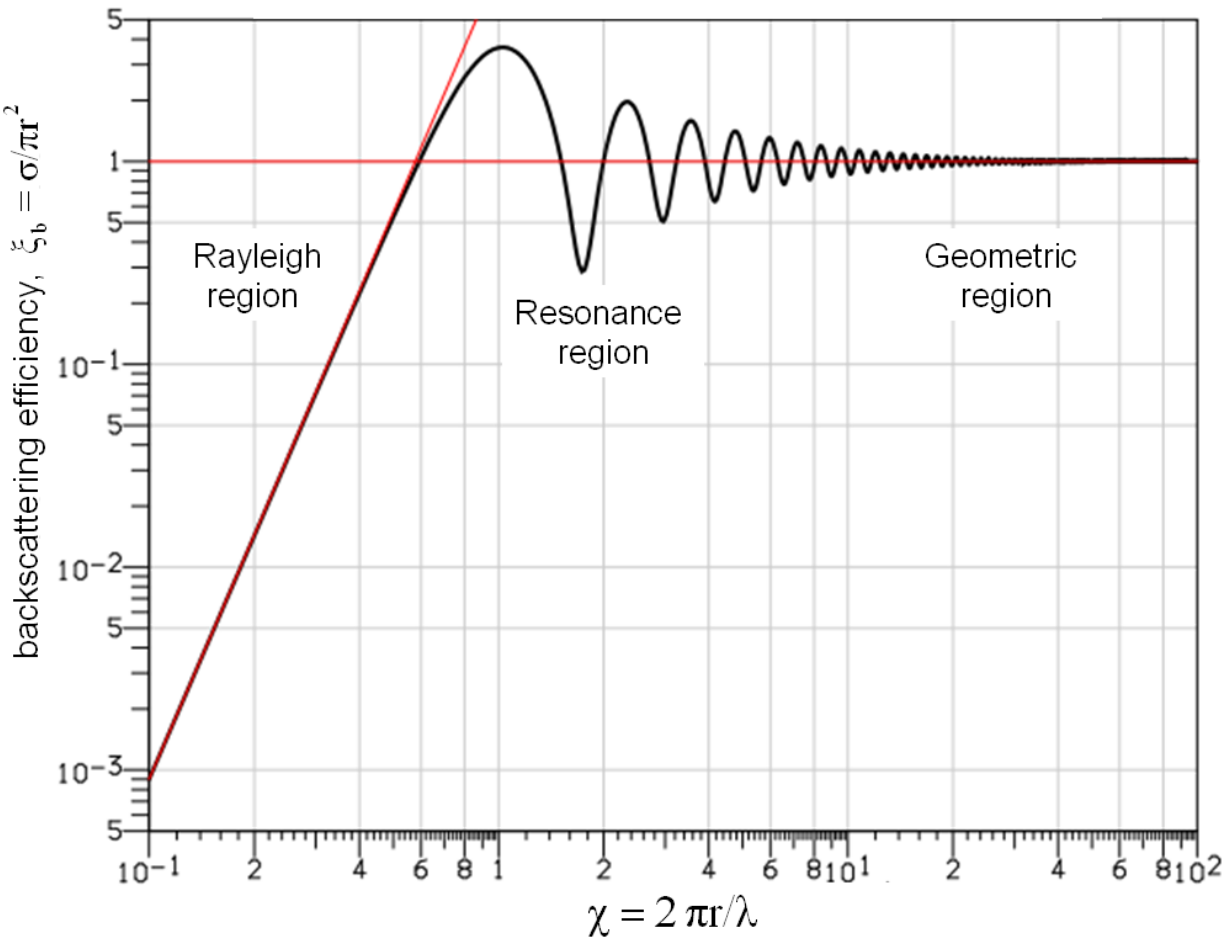

Figure 3.1: Radar backscatter efficiency as a function of χ for a metal sphere of radius r [23]

In the resonance region ($\chi \approx 1$) the scattering bodies are about the same size as the wavelength. Here, scattering values fluctuate strongly and are very frequency dependent. No simple model describes this region, but Gustav Mie provides a solution which is applicable to spheres known as Mie scattering [23].

In the geometric (or optical) region ($\chi >> 1$) the scattering bodies are much larger than the wavelength and behave as surfaces. Thus, the scattering interactions consist of reflections and refractions. The amount of spreading for a given reflection is dependent on the body's size where a larger body reflects a narrower radiation pattern.

In the context of vegetation with a C-band signal, leaves and most branches fall into the resonance region while trunks and large branches fall into the optical region. Leaves also have a Rayleigh component due to their heterogeneous cell structure.

3.1.3 Surface Scattering

The reflections from a general rough surface consist of two components: a specular component and a diffuse component. The diffuse component comprises reflection in all directions while the specular component scatters only in the specular direction.

Figure 3.2(a) illustrates the scattering behavior for different surface-roughness conditions. A perfectly smooth surface theoretically has no diffuse component and an impulse for a specular component, a moderately rough surface has near-equal diffuse and specular components, and a very rough surface has a large diffuse component and a very small specular component.

Figure 3.2(b) gives a plot of backscattering cross-section σ^0 as a function of incidence angle θ for a monostatic radar. The specular component is found at around $\theta = 0^\circ$ and is much stronger than the reflections elsewhere. The diffuse component is found at all angles and its strength decreases with increasing θ. Once again, the distribution of this curve is dependent on the surface roughness. For a *smooth* surface, the reflection is dominated by the specular component and very little scattering occurs at the other angles. On the other hand, for a very rough surface, the specular component is negligible and the curve is nearly flat across all angles.

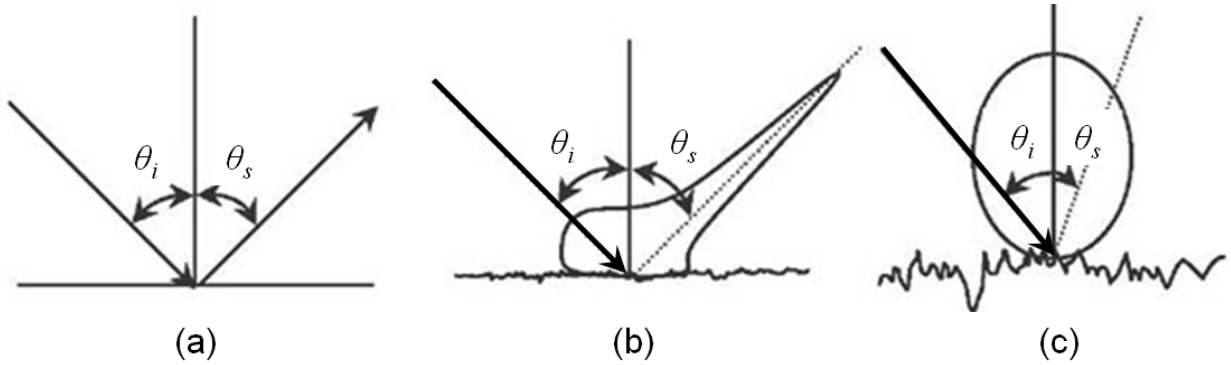

(a) Relative contributions of specular and diffuse scattering components for different surface-roughness conditions: (a) specular, (b) slightly rough, (c) very rough.

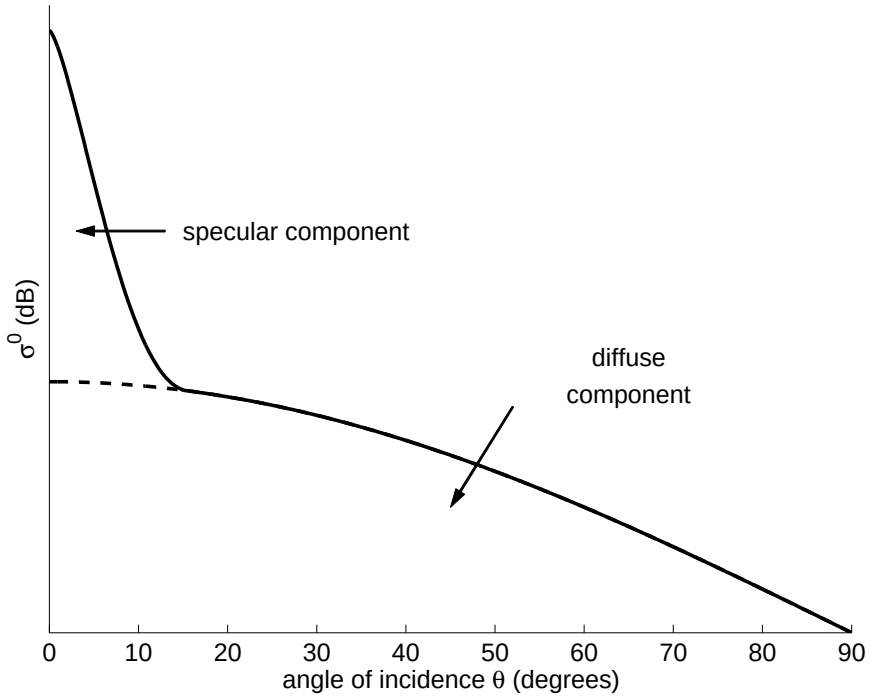

(b) Conceptual plot of normalized backscattering cross-section σ^0 versus incidence angle θ for a monostatic radar. Curve shows general behavior. σ^0 is dominated by a specular component around $\theta = 0°$ and has a diffuse scattering component which decreases slowly with θ.

Figure 3.2: Surface scattering

Criteria for "Smoothness"

Because of differences in scattering behavior, it is important to make a distinction between a rough and a smooth surface. To make this distinction, a comparison is made between wavelength λ and *standard deviation of surface height* σ_h [24]. The Rayleigh criterion for smoothness is

$$\sigma_h < \frac{\lambda}{8\cos\theta} \tag{3.1}$$

where θ is the incident angle. Ulaby [24] states that the Rayleigh criterion is useful as a first-order classifier of surface smoothness or roughness. A smoothness criterion which may be better suited for natural surfaces in the microwave region where the wavelength is on the order of σ_h, is given by the Fraunhofer criterion

$$\sigma_h < \frac{\lambda}{32\cos\theta}. \tag{3.2}$$

This criterion appears to be more consistent with experimental observations [24].

3.1.4 Volume Scattering

Volume scattering occurs when radiation penetrates into a heterogeneous medium. A volume scattering medium can be modeled as a collection of point scatterers each with extinction cross-section K_e and backscattering cross-section σ [15]. On a macro level, the parameters are extinction coefficient κ_e and volume backscattering cross-section σ_v given by

$$\kappa_e = K_e\rho \quad (\mathrm{m}^{-1}), \tag{3.3}$$

$$\sigma_v = \sigma\rho \quad (\mathrm{m}^2\mathrm{m}^{-3}) \tag{3.4}$$

where ρ is the number of scattering particles per unit volume. This model of volume scattering is illustrated in Fig. 3.3. The reflection from an individual particle is small in amplitude and wide in its re-radiation pattern. Collectively, they provide a strong response at all angles of incidence. A plot of backscattering versus incidence angle (as shown in Fig. 3.2(b)) for a volume scatterer tends to be very flat.

Signal power attenuation in a uniform volume scatterer is given by

$$L(z) = e^{-\kappa_e z} \tag{3.5}$$

where L is the one-way loss factor of the volume and z is the depth from the volume surface. This equation assumes that κ_e is uniform throughout. If κ_e is assumed to vary with depth, Eq. (3.5) becomes

$$L(z) = e^{-\int_0^z \kappa_e(z)dz}. \tag{3.6}$$

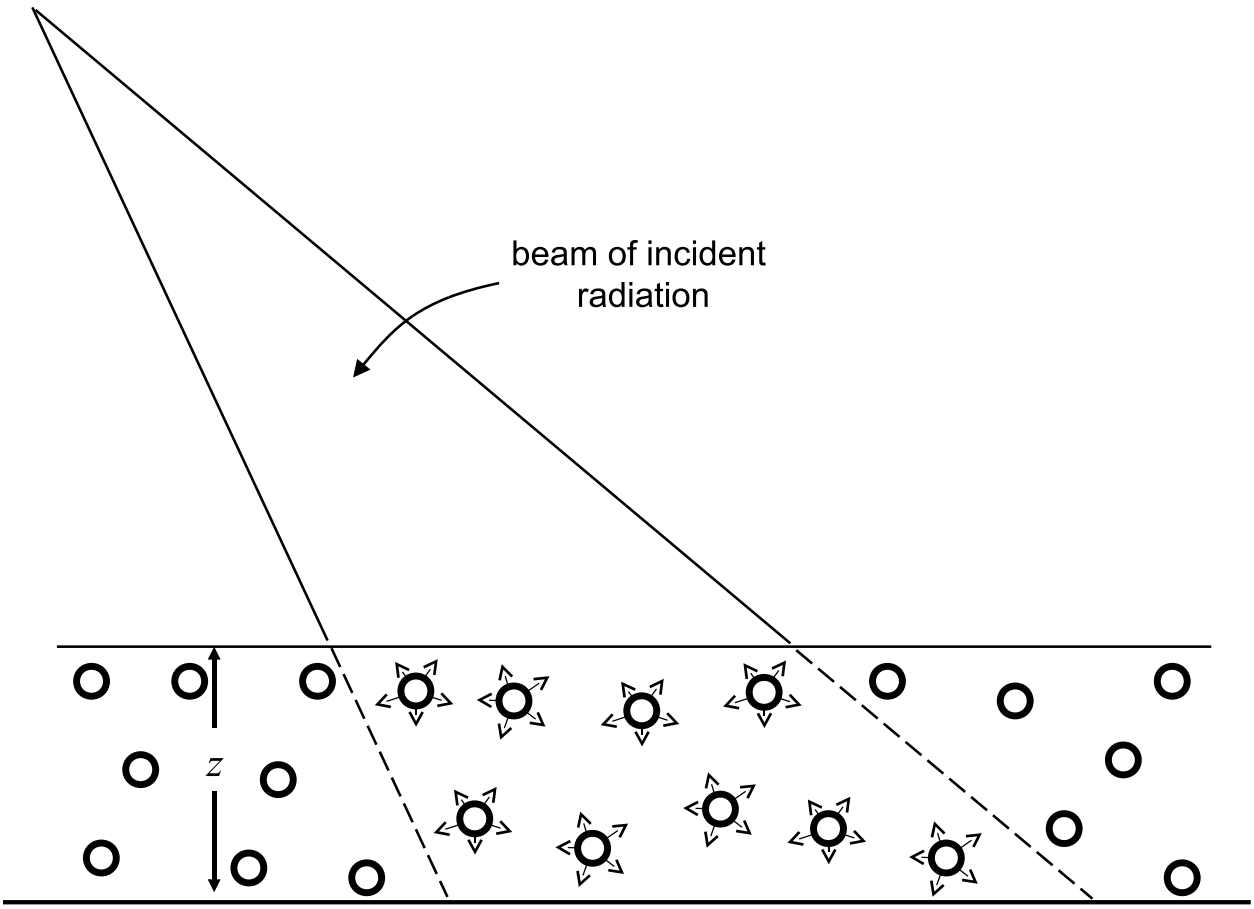

Figure 3.3: An illustration of volume scattering

Furthermore, if no assumptions are made about the distribution of κ_e so that it is allowed to vary in all three dimensions, then the following equation applies:

$$L(z, \phi, \theta) = exp\left(-\int_0^z \kappa_e(z', \theta, \phi)dz'\right) \tag{3.7}$$

which uses azimuth angle ϕ and elevation angle θ as additional arguments to account for the two other spatial dimensions. *Penetration depth* is defined as the distance when the incident power attenuates to e^{-1}.

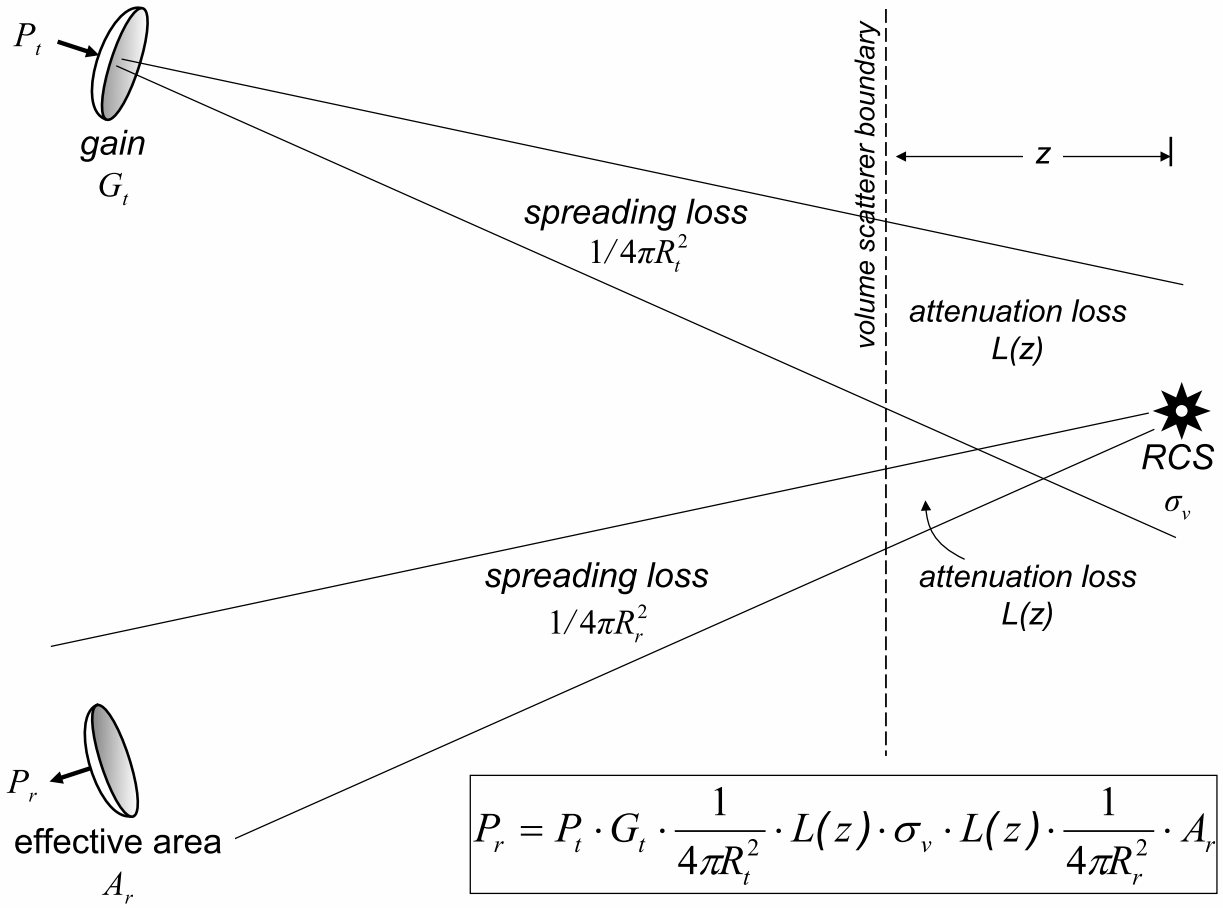

Figure 3.4: Radar equation for an embedded volume scatterer having volumetric backscattering cross-section σ_v (compare with Fig. 2.5)

3.1.5 Radar Equation for a Volume

The radar equation for a discrete scatterer, as derived in Section 2.1.6, is given by

$$P_r = \frac{P_t A_r G_t \sigma}{(4\pi R^2)^2}. \tag{3.8}$$

To extend this equation to a volume, σ is replaced by volumetric backscattering cross-section σ_v and two loss terms are inserted:

$$P_{rv} = \frac{P_t A_r G_t \sigma_v L^2(z)}{(4\pi R^2)^2}. \tag{3.9}$$

The change to v indicates that the scatterer is normalized to one unit volume. The loss terms account for the attenuation experienced while the signal travels twice through the volume. The argument z represents the scatterer's depth from the volume surface. P_{rv} represents the power associated with a single volume scattering unit and not the entire volume. This scenario is illustrated in Fig. 3.4 (compare with Fig. 2.5).

3.2 Overview of Vegetation Scattering Models

Most vegetation scattering models can be classified as physical or semi-empirical. A physical model provides a solution for σ^0 based only on the physical properties of the vegetation such as: water content, density, and inclusion shape and size. A semi-empirical model requires a less exact physical description of the vegetation and relies on one or more modeling constants which are determined empirically using regression analysis.

In most physical models, leaves are modeled as thin dielectric discs and branches as finite-length dielectric cylinders [11, 17, 25]. The simpler models assume randomness in orientation and uniformity in size and density while more descriptive models provide distributions for each of these qualities. Trunks are modeled as finite-length vertical dielectric cylinders intersecting with a flat ground plane [26]. The scattering response from each of these objects is dependent on their geometric and dielectric properties and is described via Maxwell's equations [11, 17, 25]. This thesis does not get into the details of Maxwell's

equations but Section 3.4 discusses the general scattering characteristics of these features on a conceptual level. Dielectric models for leaf and branch material are discussed in Section 3.3.

3.3 Dielectric Models of Vegetation Parts

The dielectric properties of a leaf can be modeled using dielectric mixing theory given that a leaf consists of salt water with a high permittivity, organic material with a moderate to low permittivity, and air with unit permittivity. However, some [25, 27] believe that mixing theory is ineffective for leaves because of such highly contrasting permittivities and volume fractions. As an alternative solution, Matzler [27] derives a semi-empirical dielectric formula given by

$$\varepsilon_{\text{leaf}} = 0.522(1 - 1.32m_d)\varepsilon_{sw} + 0.51 + 3.84m_d \tag{3.10}$$

where ε_{sw} is the complex permittivity of salt water (given by the Debye model) and m_d is the dry-matter fraction. Measurements taken by Johannesson [25] on a variety of deciduous tree species show that the dry matter fraction in leaves varies from 0.1 in the early summer to 0.5 at the beginning of autumn. Real and imaginary values of $\varepsilon_{\text{leaf}}$ are plotted in Fig. 3.5 against frequency for $m_d = 0.1$ and $m_d = 0.5$.

The dielectric formula used for leaves (Eq. (3.10)) can also be used to model the dielectric properties of branches. The justification for this is that branches are also high in saline content, and therefore the influence of the organic matter on microwave interactions is minimal. Measured values [25] for m_d range from 0.35 to 0.40 for the branches and 0.40 to 0.45 for the trunk, which is similar to the value for the leaves at the end of summer. Insertion of $m_d = 0.4$ into Eq. (3.5) results in the permittivity of a branch:

$$\varepsilon_{\text{branch}} = 0.246\varepsilon_{sw} + 2.05. \tag{3.11}$$

These dielectric models indicate that the permittivity of a branch or leaf is highly correlated to water content (in addition to frequency). Since σ^0 increases with the target permittivity, vegetation is expected to produce increased backscatter when it contains a high water content.

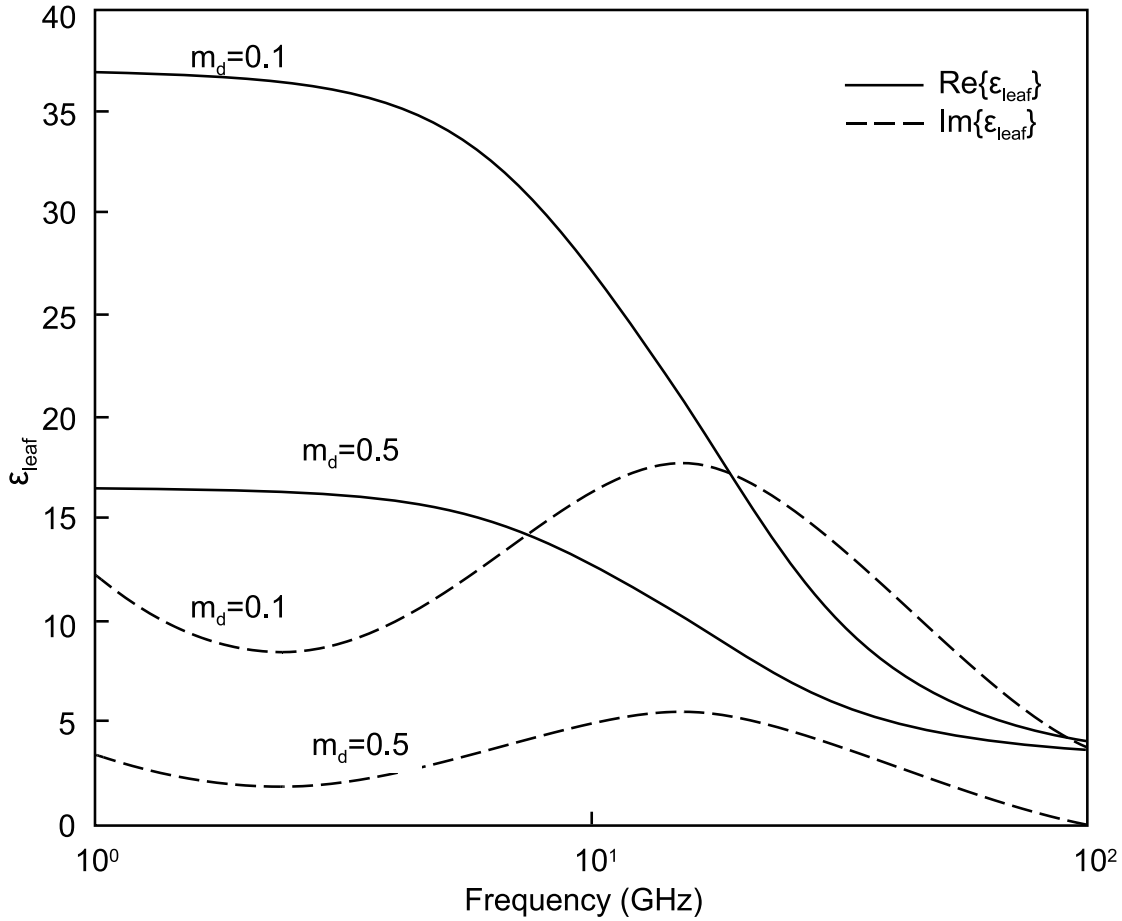

Figure 3.5: Real and imaginary values of $\varepsilon_{\text{leaf}}$ plotted against frequency in Figs. 3.5 for $m_d = 0.1$ and $m_d = 0.5$

3.4 Scattering Characteristics of Vegetation Parts

Based on the geometric and dielectric descriptions given to the vegetation parts in the previous sections, the scattering behavior from these features can be described via Maxwell's equations. Without getting into the detailed mathematics, this section describes the general scattering characteristics of each of the features. Leaves and branches are discussed together because their reflections are difficult to separate. They are collectively treated as a volume scatterer and are described by *resonance* scattering because many of their geometries are near the size of a wavelength. Leaves also have a *Rayleigh* scattering component due to their heterogeneous cell structure. Trunks, due to their large size, are treated as discrete-target

scatterers or surface scatterers and are described by *resonance* and *geometric* scattering. The discussion on trunks also applies to large branches.

3.4.1 Leaf and Branch Scattering

First, we consider the scattering response of an individual leaf or branch. A leaf or branch acts like a small antenna. Since a leaf is small, it produces a wide radiation pattern. On the other hand, a branch produces a radiation pattern which is wide in one direction and narrow in the other as a result of its rectangular geometry. The orientation of the leaf or branch is also important. For a leaf, the backscatter amplitude peaks when the leaf is normal to incidence and decreases as its orientation departs from normal. Similarly, the backscatter amplitude of a branch peaks when the branch is perpendicular to incidence and decreases as the branch's orientation departs from perpendicular. The intersection between two branches has the potential for strong backscatter if the geometry resembles that of a retro-reflector.

The detectability of a particular leaf or branch depends on the strength its return compared to the strength of the return from the surrounding foliage (which can be treated as noise). Considering a well populated tree and a resolution cell of 50 x 50 x 50 cm, a single leaf is not detectable because it is drowned by the many other leaves within the same resolution cell. For a branch to be detectable, it must be sufficiently large so that its signal can be discriminated from the surrounding foliage. However, if a second branch of similar size is found within the same resolution cell, neither branch can be discriminated from the other even if they are detectable from the foliage.

Due to insufficient resolution in most radar systems, all leaves and most branches cannot be individually resolved. As a result, leaves and branches must be studied collectively and treated as a volume scatterer. Recall from Section 3.1.4 that the power received from a volume element inside of a volume scatterer is

$$P_{rv} = \frac{P_t A_r G_t \sigma_v L^2(z)}{(4\pi R^2)^2} \tag{3.12}$$

where L is

$$L(z, \phi, \theta) = exp\left(-\int_0^z \kappa_e(z', \theta, \phi) dz'\right). \tag{3.13}$$

This particular loss equation accounts for κ_e variations in all three dimensions and is most appropriate for vegetation since a tree is rarely uniform in density. Generally, the center of a tree has a lower concentration of leaves and a higher concentration of branch material; while the perimeter of a tree is the reverse. Also, when considering a single tree (opposed to a vegetation canopy) its curved incident surface makes it difficult to base measurements solely on z.

The volumetric cross-sections κ_e and σ_v (see Eqs. (3.3) and (3.4)) can be related to cross-sections of the individual leaves and branches through

$$\sigma_v = \sigma_l \rho_l + \sigma_b \rho_b, \kappa_e = K_{el} \rho_l + K_{eb} \rho_b \tag{3.14}$$

where l and b correspond to leaf and branch.

3.4.2 Trunk Scattering

Recall that a tree trunk is modeled as a finite-length dielectric cylinder intersecting with a flat, homogeneous ground plane. Assuming that the trunk size is significantly larger than the incident wavelength—so that reflections are described by geometric scattering (Section 3.1.2)—this geometry accounts for three types of reflections. First, surface reflections are produced from the trunk midsection. These surface reflections are predominantly specular if the trunk surface is smooth. With the exception of very large trunks, these specular reflections have a wide radiation pattern due to the trunk's finite width and convex incident surface. Second, corner reflections are produced from the intersection between the trunk and ground which resembles the geometry of a dihedral corner reflector. These reflections are very strong and are present at all angles of incidence. The third source of scattering, which is only present at shallow angles of incidence, is multi-path reflections from off the ground. These reflections obscure the final image.

A trunk surface may be considered to be smooth or rough depending on radar wavelength, incidence angle, and surface height distribution. To illustrate this idea, we consider a scenario where the radar wavelength is 5 cm (C-band), the incidence angle is 0 degrees, and the surface height distribution is given by Fig. 3.6. This figure contains a beta distribution

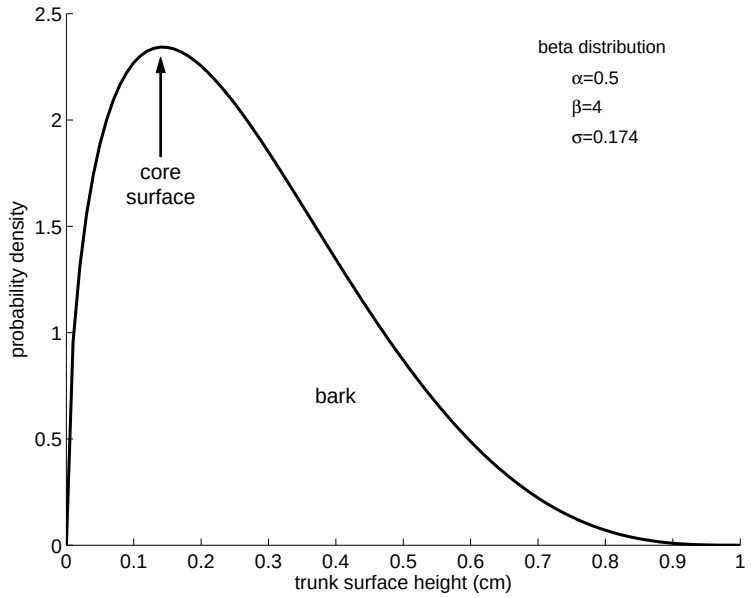

Figure 3.6: Conceptual plot to represent the surface height distribution of a tree trunk. This is a beta distribution with $\alpha = 1.5$ and $\beta = 4.0$ and limits of 0 and 1 cm. The peak corresponds to the mean height of the hard core surface and the right-hand tail corresponds to the bark.

with parameters $\alpha = 1.5$ and $\beta = 4.0$, limits 0 and 1 cm, and standard deviation $\sigma = 0.174$. The peak corresponds to the mean height of the hard core surface and the right-hand tail corresponds to the bark. Applying the Fraunhofer smoothness criterion from Section 3.1.3) results in $\lambda/32\cos\theta = 0.187$ cm and $\sigma_h = 0.174$ cm. Since these two values are on the same order of magnitude, the trunk in this scenario is considered smooth which indicates that the majority of its reflections are specular in nature.

3.5 Summary

This chapter has considered some of the key microwave-vegetation interactions based on popular scattering models. Because of radar resolution limitations, leaves and small branches are collectively studied as a volume scatterer where their scattering behavior is described by *resonance* and *Rayleigh* scattering. Trunks and large branches are studied as discrete-target scatterers and surface scatterers. Their scattering behavior is described by *resonance* and *geometric* scattering. The determination of a *large* branch is dependent on whether the branch's reflection provides enough contrast from the surrounding foliage. We learned that trunks provide three types of scattering: surface reflections from the trunk

midsection, corner reflections from the trunk base, and multi-path reflection from off the ground. We determined that a trunk with a bark thickness of 1 cm or less is considered *smooth* to a C-band signal.

Because of approximations used, the scattering models presented in this chapter are only approximate. The present work helps provide some of the empirical data needed to validate the model predictions.

Chapter 4

Development of a 3D-SAR Imaging System

Developing a 3D SAR imaging system is a significant undertaking because it involves an integration of many components and technologies. It requires a sophisticated radar module, a large and high-precision scanning apparatus, an intelligent software controller, signal processing code, and a variety of electrical and hardware components. Due to the lack of precedence of this type of system, design was a significant portion of the overall development process. The current implementation is relatively simple and is considered a preliminary design concept.

This chapter serves two purposes. One is to provide the general reader with an understanding of the system which is responsible for generating the imagery presented in the following chapters. The second purpose is to provide the relevant documentation for future developers to continue with development without having to repeat process.

This chapter is organized into four sections. Section 4.1 provides a high-level overview of the system. Section 4.2 presents high-level system requirements, discusses key design decisions, and indicates how the high-level requirements are implemented.

Section 4.3 provides a description of the developed system. This description includes a labeled CAD drawing, a system-level functional description, an enumeration of components, and descriptions of the components in the context of their role to the system as a whole. For more detailed descriptions of the individual components, the reader is referred to Appendix A.

Finally, Section 4.4 provides a post-development evaluation which discusses the fulfillment of the high-level requirements. The majority of the discussion is devoted to resolution performance.

4.1 System Overview

A photo of the scanning platform is found in Fig. 4.1. The platform consists of a vertical tower which rides on the rails of a broad horizontal base. The base and tower provide movement for a pair of antennas to provide a scan area of 1.7 m x 1.7 m. The scan area represents the system's synthetic aperture and is the limiting factor on the system resolution (see Section 2.2.3). The system is intended for relatively close targets, on the order of 20 to 100 m. The real antenna beamwidth is 30 degrees, which is an important consideration when attempting to scan tall targets.

Figure 4.1: Photo of scanner

System operation consists of collecting backscatter samples from a grid of antenna positions (separated by 5 cm or less). To accomplish this, the scanner completes multiple passes in one direction while incrementally progressing in the other. Generally, the vertical axis is used as the fast axis and the horizontal is used as the slow axis. A software controller is responsible for the scanner's progress, which can be an hour or two for a full scan and can consist of thousands of samples. Following data collection, post-processing software reconstructs the backscatter data into 3D imagery.

So far, the system has been used for applications of snowpack imaging and vegetation imaging. Two snowpack experiments took place in January and February of 2010 in Snowbird, Utah. The purpose of these experiments was to detect the physical characteristics of a snowpack for the purpose of predicting avalanches. Results from these experiments are found in Stephen Preston's master's thesis [19]. In the summer of 2010, the system was used to image several vegetation targets (trees) on Brigham Young University campus. These experiments are the topic of this thesis.

4.2 High-Level Requirements and Design Decisions

This section provides insight into the system's design process and is intended to assist future developers to make intelligent decisions without having to repeat design steps. First, a list of high-level system requirements is provided. Following, discussions are given to some of the major design decisions.

The following list contains the high-level system requirements.

R1. *The system shall spatially discriminate in azimuth, elevation, and range.* Basis: this requirement is necessary for 3D image generation.

R2. *The system shall be capable of spatial resolution on the order of one foot or less.* Basis: this level of resolution required to discriminate the internal features of volume targets such as vegetation and snow.

R3. *The system shall know the position of the antennas with 1 mm accuracy.* Basis: backscatter phase measurements should have an accuracy of one tenth of a wavelength [28]. This amount of accuracy supports frequencies up to K_a-band.

R4. *The system shall observe the Sampling Theorem (Section 2.2.1) for its spatial sampling.* Basis: failure to observe the Sampling Theorem results in aliasing.

R5. *The system shall be capable of automating full scans.* Basis: due to the number of sample locations, manual operation of a scan would be extremely tedious and time consuming.

R6. *The system shall be portable. Specifically, the system shall be light enough to be carried by two persons and small enough to be transported through standard-sized door openings and loaded onto a truck.* Basis: the system is intended to be used for outdoor field experiments

The following discussions describe some of the major design decisions. For each discussion, the chosen implementation is justified and considered alternatives are presented; and if a choice between two options is arbitrary, it is said so.

Platform Structural Design

Designing the platform's structural framework encompasses several design considerations. Some of these include: how shall it support weight, how shall it provide motion (R1), how shall it provide the required accuracy (R3), how large shall it be, and what material shall it be made of.

The platform's framework consists of a vertical tower which sits on the rails of a rigid base unit resembling an inverted T-shape. This configuration is chosen because it has proven to provide high stability in applications such as microwave near-field scanning [29, 30, 31]. Aluminum is chosen as the frame material since it is sturdy enough to accommodate R3 while being light enough to satisfy R6.

Dictating the platform size, 1.7 m x 1.7 m is allocated for the scanning area. This decision is constrained by R6, which, in part, states *the system shall be small enough to be transported through standard-sized door openings.* As the standard door height is 82 inches, we allocated that amount for the total platform height. The other requirement that is influencing this decision is R2: the resolution requirement. According to Eq. (2.5), resolution in the azimuth and elevation is improved with an increase in synthetic aperture size. So to maximize resolution, the platform is built as large as possible while maintaining

the portability constraint. The final dimensions of the platform come out to be 8 ft x 3 ft across the base and 86 inches in height. This is slightly taller than a standard door height of 82 inches so transportation under a door is accomplished by tilting.

Radar Module and Frequency Selection

A radar module named μASAR is chosen to perform signal handling duties, including generating, modulating, transmitting, receiving, and recording electromagnetic information. Part of the reason this system is chosen is because it has played a role in many BYU research projects in the past and is readily available. It is also compact and extremely parameterizable. Its compactness accommodates the portability requirement R6, especially since it is small enough to be mounted on the mounting plate along side the antennas.

A common option found in previous research projects [32, 33, 34, 35, 36] is a network analyzer. A network analyzer is an effective tool for analyzing microwave backscatter because it offers a large range of frequencies and bandwidths, providing for a more comprehensive spectral analysis of the target being studied (see Preston [19] for further discussion on this option). While the μASAR is only configured for a single frequency band, it offers many conveniences that are pre-tailored for LFM-CW SAR applications and has superior range resolution (see Section A.1 for a description of the μASAR's capabilities).

Antennas

A pair of horn antennas is selected for transmission/reception. Two horn antennas (full-duplex) are used as opposed to one (half-duplex) to accommodate the μASAR since it employs frequency modulation which requires simultaneous transmission and reception.

Horn antennas, in particular, are used because they are common for short-range applications as they are excellent at preserving the phase of the transmitted wave. This preservation of phase translates into more accurate measurements and improved resolution.

Motors and Lead Screws

To enable scanner movement, one motor and one lead screw are employed for each axis. The selection of motors involved considerations of load capabilities, accuracy, and

communication interfacing. These considerations lead to the decision to use STM23S-3RE stepper motors. These particular units feature: the integration of the drive and motor in one compact unit; a rich serial command language with easy interface; and an optical encoder with resolution of 4000 counts per revolution, which translates to 1.3 μm per count when used in conjunction with the system's lead screws.

These motors are preferred for several reasons. Their integrated nature contributes to the portability of the system (R6). Also, the serial command language simplifies communications from a host PC (R5). Finally, the encoder feedback in combination with their precision of movement provides the system with the required positional awareness and accuracy (R3).

The motors are coupled to a pair of acme lead screws, used to convert the radial motion of the motor shafts into translational motion. We invested in high quality, high precision screws to ensure satisfaction of R6. The acme thread form provides very high precision, only surpassed by the very costly square thread form.

Cabling

Cabling is required for transmissions of data and power to the various devices mounted to the scanner. Cabling considerations include power requirements, cable crosstalk, and exposure to repeated movement and flexing. Because cables are connected to moving parts and experience constant flexing, stranded rather than solid conductor wire is used. To reduce crosstalk, either twisted pair or shielding is used. Also, appropriate wire gauges are selected to accommodate power requirements.

System Controller Software

A software controller is created in accordance with R5, which states *the system shall be capable of automating full scans.* The controller is written in C++ and hosted on a PC. The choice of C++ is fairly arbitrary. A PC host is chosen because it is more practical than installing code onto an embedded device such as an FPGA; which would be more compact and portable but would be more difficult to implement due to hardware resource constraints, lack of software support, and lack of a graphical user interface (GUI). The GUI built into

the current software provides a means for selecting parameters, controlling the scan progress, and troubleshooting.

4.3 System Description

This section provides a system-level description of the scanning system. This description includes a high-level description of the functional operation, an enumeration of components, and descriptions of the components in the context of their role to the larger system. More detailed descriptions of the individual components can be found in Appendix A.

When the design elements of the previous section are brought together, they result in the system represented in Fig. 4.2. This drawing includes two opposing perspectives labeled top view and bottom view in which the components are labeled. The system comprises the following components:

- Scanning Platform
- Radar module
- Horn antennas (x2)
- Stepper Motors (x2)
- System Controller Software
- Post-Processing Software

The scanning platform (or scanner) resembles an inverted T-shape configuration consisting of a vertical tower which sits on the rails of a rigid horizontal base unit. The platform stands 7 ft 2 inch tall, weighs approximately 200 lbs, and is constructed of aluminum. Its role is to provide range of motion to the antennas. It provides a range of 1.7 m x 1.7 m, which defines the system's synthetic aperture. The platform provides a pluggable cabling interface for data and power, making for easy relocation set-up. The interface is not shown in the drawing, but it mounted next to the horizontal motor.

The horizontal base unit has dimensions of 8 ft x 3 ft x 9 inches and is constructed of rectangular tubing of 2 x 3 inch and 1/4 inch thickness. The 9 inch height provides clearance

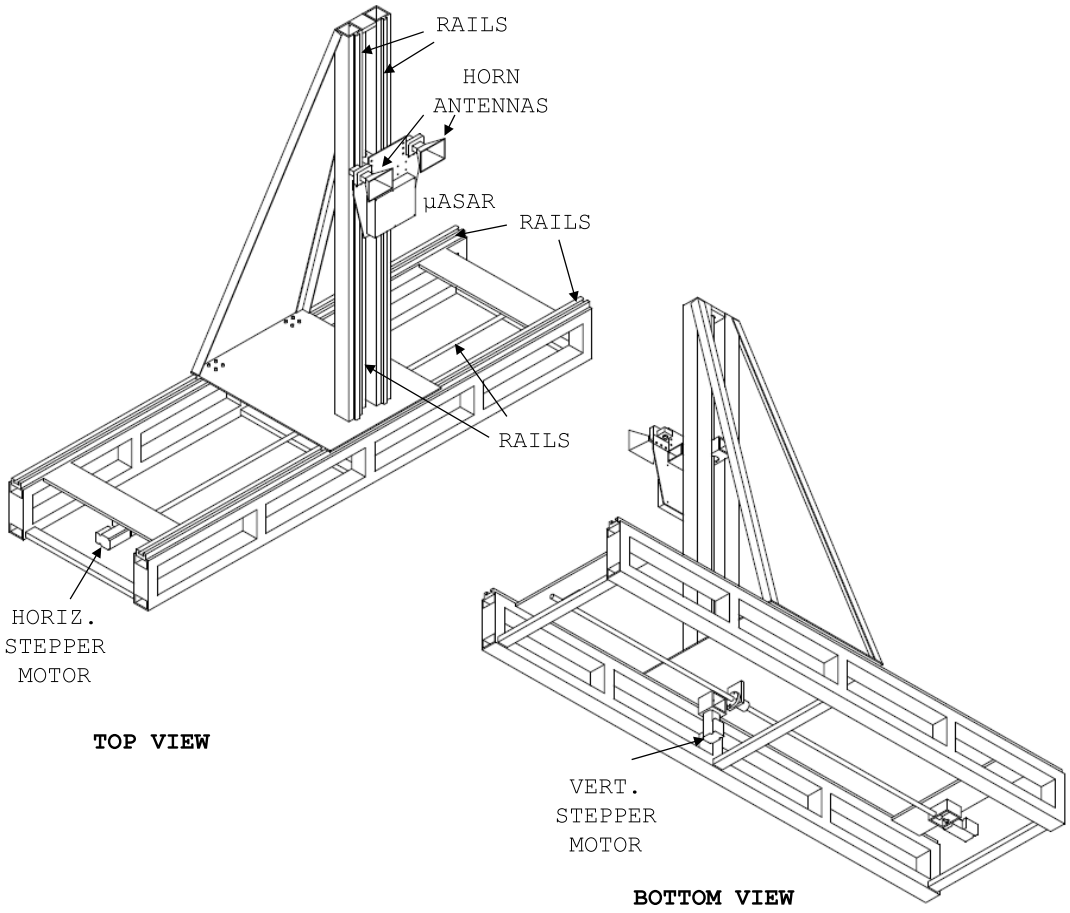

Figure 4.2: Computer drawings of the ground-based system's hardware from opposing perspectives

for the moving parts, including the horizontal screw, mounting blocks, motors, and cabling. The base is spanned by an acme lead screw and two Teflon coated, 20 mm rails.

The vertical tower comprises a base plate, two vertical columns, and two pieces of angle bar. The base plate is 2 ft wide, 3 ft deep, and 1/2 inch thick. The vertical columns are 3 x 3 inch, 1/4 inch thickness, and 73 inch tall and they sit front and center on the base plate. The columns are separated by 3 inches to provide room for the vertical screw, nut, and mounting block. The angle bar extends from the rear corners of the base plate to the top of the vertical columns, acting as braces. Similar to the horizontal base, the tower is spanned by a lead screw and two Teflon coated rails.

The horizontal base provides stability and movement to the vertical tower. The tower sits atop the two rails of the horizontal base and is fastened to a nut on the horizontal lead screw. A rotation of the horizontal lead screw pushes the tower along the horizontal rails. The horizontal screw is strategically positioned toward the front to more efficiently carry the weight of the front-heavy tower. The vertical motion is accomplished in a similar fashion. The antenna mount is situated on the two vertical rails and is fastened to a nut on the vertical lead screw. A rotation of the vertical lead screw pushes the antenna mount along the vertical rails. The mount holds the radar module and antenna pair (seen in top view).

The lead screws are driven by stepper motors. The horizontal axis's motor is mounted at the end of the horizontal base where it is coupled to the horizontal screw (seen in top view). The vertical axis's motor is mounted underneath the vertical tower's moving base plate where it is coupled to the vertical screw (seen in bottom view).

The system controller, installed on an independent PC (not shown in the drawing), manages the automation of a scan. It allows a user to select scan parameters including scan area, sampling intervals, direction, and speed. The progression of a scan consists of making multiple passes across one axis while slowly progressing across the other axis. Each time a designated sampling point is reached, the scanner is paused and two marker packets, which include the scanner position, are sent to the radar module.

Both the system controller and motors perform separate position tracking. Each motor contains an optical encoder which tracks its radial movement for the period that it remains powered on. While these encoder values are available upon request, the software generally does not ask for them. The software keeps its own record in order to eliminate timing delays. Since the movement commands use absolute coordinates, and since the software waits for an acknowledgment upon completion of each command, querying the encoders does not provide any additional information. The only situation where the encoders are queried is in the case of a software crash or loss of power to the PC.

The μASAR (currently acting as the radar module) is configured for full-duplex operation, meaning that it supports separate transmit and receive antennas which operate simultaneously. During scanner operation, the μASAR is continuously transmitting microwave pulses at the target. The received pulses are recorded to a Compact Flash card after some

intermediate processing in the μASAR. The position packets which are received from the system controller software are written to a second Compact Flash card. Both the pulse packets and position packets are time-stamped for later integration. At the completion of a scan, the Compact Flash cards are removed from the μASAR and the data off-loaded for handling by the post-processing code. This code reads the data and performs the reconstruction algorithms described in Section 2.2.2 to generate three-dimensional imagery.

Spatial Sampling Requirement

As discussed in Section 2.2.1, target backscatter must be sampled with a high enough spatial frequency to satisfy the Sampling Theorem. According to Eq. (2.10), spatial sampling for a SAR system must occur at intervals less than half the size of the antenna. For this system with an effective antenna size of 10 cm, spatial sampling must occur at less than 5 cm intervals. This requirement is easily met for this system since the stepper motors are capable of increments of 1.3 μm.

Time of Scan

A time estimation for the execution of a complete scan is calculated from scan size, sampling interval spacing, and motor velocities. The max velocity that the motors can handle is approximately 7 rps or 3.5 cm/sec; above this speed the magnets begin to slip. If a full scan is performed (1.7 m x 1.7 m) with 3 cm intervals, the total distance traveled is 9860 cm, which breaks down to 57 vertical passes and one horizontal pass. Traveling this distance at 3.5 cm/sec takes 2817 seconds. Including pauses at each sampling position, this time increases by a factor of approximately 1.5, resulting in a total time of approximately 70 minutes. This amount of time is long, but acceptable for a field experiment studying stationary trees.

4.4 Post-Development Evaluation

The developed ground-based 3D SAR system described in the previous section satisfies each of the requirements enumerated in Section 4.2 with the exception of the resolution requirement. This requirement states *the system shall be capable of spatial resolution on the*

order of one foot or less. The following discussion describes the actual resolution capabilities of the system.

Resolution Performance

As described in Section 2.2.3, 3D SAR resolution is defined in three dimensions: range, azimuth, and elevation. Range resolution is dependent on radar bandwidth and is defined by Eq. (2.3). Since the highest bandwidth setting on the μASAR is 200 MHz, the best range resolution for this system is

$$\Delta_R = \frac{c}{2\beta} = \frac{3 \cdot 10^8}{2 \cdot 200\text{MHz}} = 0.75 \text{ m}. \tag{4.1}$$

Resolutions in azimuth and elevation are defined by Eqs. (2.15) and (2.16). Note that the approximation of Eq. (2.10) cannot be used since the synthetic aperture is limited by the platform size. Remember that one of the conditions of that approximation is that the target is illuminated by the entire beamwidth. For a 1.7 m scanning aperture, this is only true for ranges less than 1.9 m.

According to Eqs. (2.15) and (2.16), these resolutions are dependent on system frequency and synthetic aperture size. Given an operating frequency f of 5.4 GHz, a synthetic aperture size D_{sar} of 1.7 x 1.7 m, and without specifying range, the azimuth and elevation resolutions for this system are

$$\Delta_{\text{AZ}} = R\phi_{sar} = R\frac{\lambda}{2D_{sar}} = R \cdot \frac{0.056}{2 \cdot 1.7} = 1.6R, \tag{4.2}$$

$$\Delta_{\text{EL}} = R\theta_{sar} = \quad ... \quad = 1.6R. \tag{4.3}$$

Table 4.1 provides resolution values for a variety of ranges.

Returning to the resolution requirement, which requires resolution to be on the order of one foot or less, this requirement is satisfied in azimuth and elevation for ranges of about 20 m or less. However, it is not satisfied in the range dimension and it is not satisfied for all three dimensions when the range is greater than 20 m. As a consequence of this, some of the internal features of a vegetation target, such as small branches, may be difficult to

Table 4.1: System resolution for various ranges ($f = 5.4$ GHz, $D_{sar} = 1.7$ m)

Range	Resolution
5 m	0.082 m
20 m	0.33 m
50 m	0.82 m
100 m	1.63 m
500 m	8.2 m

identify at longer ranges. However, many scattering attributes can still be observed such as: attenuation behavior, foliage boundary definition, and trunk and large branch definitions.

Suggestions for Follow-up Development

The most effective way of increasing resolution for future experiments is to increase the system frequency. The current radar module, the μASAR, only supports C-band; but it is possible to install another radar module with a higher operating frequency. The scanner has the positional accuracy to accommodate frequencies up to K_a-band. The other way to increase resolution is to increase the size of the scan area; however, this requires the construction of a new platform.

Chapter 5

Data Collection

This chapter describes the tree scattering experiments conducted in August 2010. Topics include tree selection, conducting the experiments, post-processing, and image preparation and presentation. At the end, an overview of the generated 3D imagery is given.

5.1 Tree Selection

Selecting appropriate trees as targets is important for the clarity of the resulting imagery. Clarity refers to the visibility of the tree in its entirety (i.e., from front to back); visibility of the internal features, including the leaves, branches, and trunk; and separation from noise and interference. Considerations in tree selection include: overall size (height and width), branch and trunk size, leaf density, accessibility, and diversity.

Tree height and width is limited by the antennas' 30° beamwidth. While increasing range expands the beam, doing so also degrades the image resolution. To maintain good resolution, relatively small trees are selected: between 5 and 10 m in height.

Trees should not be so small that their internal features (i.e., leaves, branches, and trunk) have poor scattering efficiency. For the strongest returns from these features, they should give values of χ near or greater than 1 (see Section 3.1.2). This means that their size is equal to or greater than the incident wavelength (which is 5 cm in this case). If the features are significantly smaller than this, they become Rayleigh scatterers and their scattering efficiency decreases with size (refer to Fig. 3.1). Since leaves consist of a heterogeneous cell structure, their size is less of a factor and their return is maximized by a high leaf density (see Eq. (3.4)).

To eliminate unnecessary interference, trees should be isolated from any potentially bright features (such as buildings, cars, or lamps) which may drown out, obscure, or overlap the tree image.

Accessibility is also an important factor in tree selection. For the sake of simplicity, all trees are selected from on the BYU campus, since performing off-campus experiments requires a large truck to transport the scanner and equipment, additional manpower to lift the scanner onto and off of the truck, and power generators if there is no electrical outlet nearby. Some factors affecting the accessibility of the on-campus trees include: levelness of the ground (i.e., no hill-side), amount of student traffic, proximity to a power source, and presence of an obstruction positioned between the tree and scanner (such as a lamp, handrail, or other tree).

Finally, variability between the trees is desired. For example, trees possessing different foliage densities and leaf types are selected to observe the effect these physical qualities have on attenuation rate.

Ultimately, three trees were selected: a honeylocust, a Norway maple, and a Colorado blue spruce. The honeylocust is found in Fig. 5.2, the maple is found in Figs. 5.3 and 5.4, and the spruce is found in Fig. 5.5.

5.2 Conducting the Experiments

Each scan, or experiment, was conducted in a similar manner. They were each performed during the month of August and completed in a single sitting (4 hours in the longest case). A scan consisted of the collection of backscatter data from an array of sample locations across azimuth and elevation. The azimuth samples spanned 1.7 m and were spaced at intervals of 2.5 cm while the elevation samples spanned 1.7 m and were spaced at intervals of 3.0 cm. Figure 5.1 provides a photograph of the scanner in operation including the computer and additional equipment.

While honeylocust and spruce were scanned a single time, the maple was scanned a second time from a different azimuth angle (approximately 90° apart). The purpose of this additional experiment is to evaluate system repeatability and to understand the dependency on azimuth incidence angle.

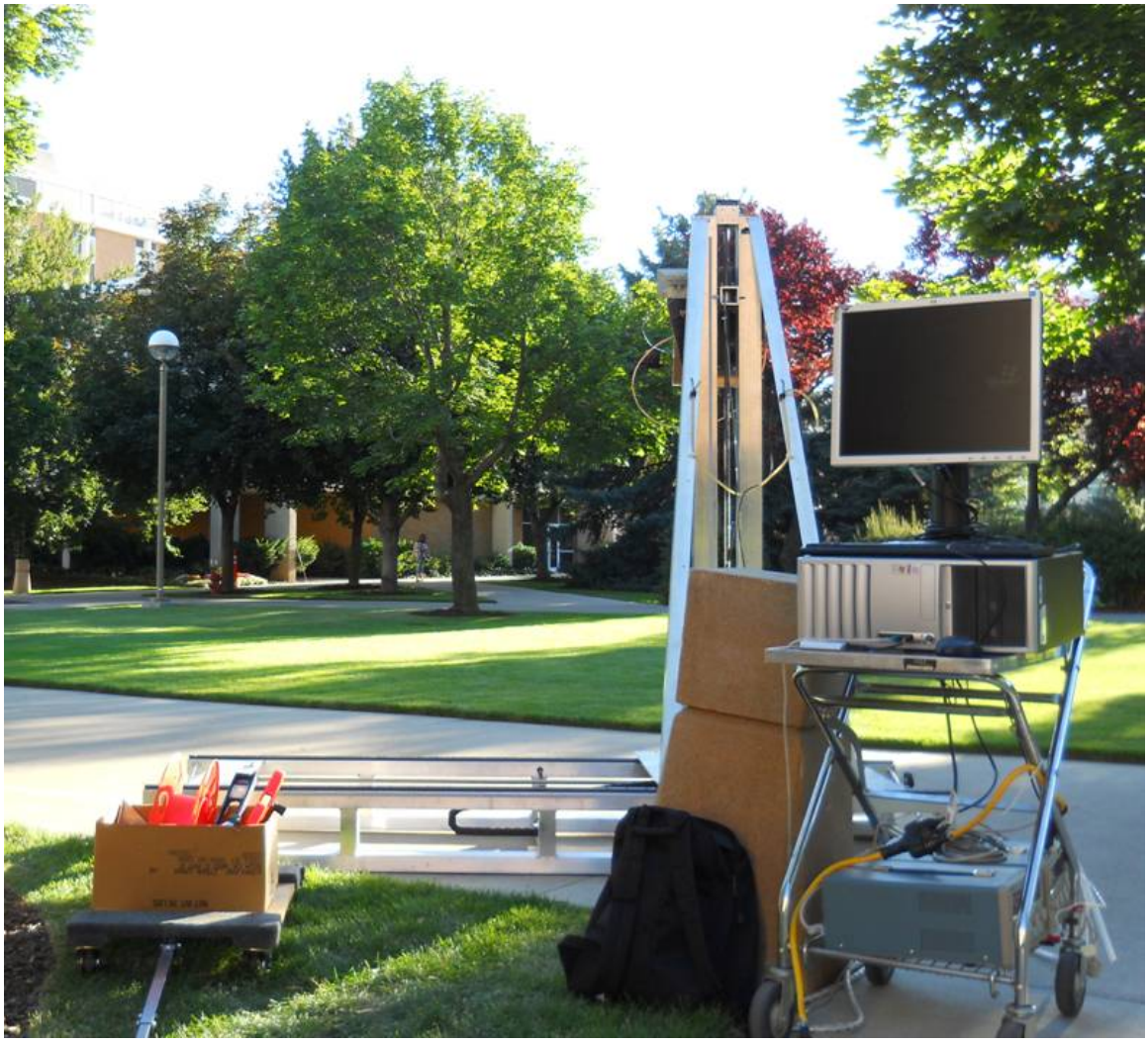

Figure 5.1: Photo of the scanner in operation with accompanying equipment. Normally a laptop computer is used rather than the desktop shown here. (Experiment 2)

5.3 Post Processing

At the completion of a scan, the data is stored on two separate Compact Flash cards: one for is SAR data and the other is for position data. Matlab code retrieves and integrates the data from the two cards, range compresses it, and performs the backprojection algorithm to produce 3D SAR images (see Section 2.2.2).

5.4 Image Preparation and Presentation

After post processing, a few finishing touches are applied to the imagery to make it more presentable. First, the images are appropriately cropped so that the trees occupy most of the image space and unwanted surrounding features are eliminated. Some of these unwanted features include buildings, vehicles, and curbs. As mentioned earlier, these features can be very bright in comparison and can drown out or obscure the tree. In the instance that a competing feature is so close to the tree that it remains in the image after the rectangular crop, and as long as it is not actually overlapping with the tree, it is removed manually. On the other hand, if it is overlapping with the tree it must be left in the image. Following the crop, a simple low-value threshold is applied to remove most of the background noise.

In an ideal situation, this imagery would be presented as a 3D rotating electronic image. However, because of the limitations of the printed page, this imagery is presented as a set of 2D images. While additional presentation schemes are employed in the next chapter, here the imagery is presented as a set of three 2D profile images including front, side, and top views. The gray-scale pixel values correspond to receive power. Axes are labeled elevation, azimuth, and range with units of meters. The physical size of a single pixel is 0.1 m in each of the three dimensions even though the system resolution is coarser. Each set of images is accompanied by an optical image taken from the perspective of the radar. These image sets are found at the end of this chapter in Figs. 5.2-5.5.

5.5 Imagery Overview

The imagery for experiment 1 is found in Fig. 5.2. This imagery provides the best overall results of the four. Some initial observations are that the tree outline is well-represented and the effects of attenuation are evident. The curb in the front and the car in the back (seen in the optical image) are far enough away from the tree that they are eliminated by the rectangular crop. On the other hand, a retro reflector (not shown in the optical image) and the bushes on the left are within the rectangular crop (between 0 and 2 m in azimuth) but have been manually removed.

The imagery for experiment 2 is found in Fig. 5.3. Some manual cropping is also required in this imagery as some isolated reflections are found in the back corners that are

probably associated with the lamp on the left and the small bush on the right. This imagery also demonstrates very good results.

The imagery for experiment 3 is found in Fig. 5.4. Note that this experiment features the same physical tree as the previous experiment. Unfortunately, this imagery does not turn out particularly well. Chunks are missing from the top and front of the tree and the trunk is distorted. A possible cause of this is that the scanner is stationed too close to the tree (15 m compared to 20-25 m for the other trees). At the least, this explains why the top of the tree is missing, since it is completely outside of the radar's physical beam. Additionally, the μASAR may not be capable of handling targets at this proximity. Unfortunately, because of obstructions, moving the scanner farther back was not possible.

The imagery for experiment 4 is found in Fig. 5.5. Since this tree is on the small side, observing its branches and trunk is more difficult, but a comprehensive study on the foliage is still possible. During the experiment, two retro-reflectors were positioned on both sides of the tree for the purpose of more easily locating the tree in the radar imagery (and to verify focus). At that time, I was uncertain of how difficult that would be since it was chronologically the first experiment. These reflectors are represented in the radar imagery as star-bursts (located at 2 and 7 m in azimuth). As a final observation, notice the repeating pattern on the left side of 5.5(c). This pattern originates from the recessed door behind and to the left of the tree which possesses the exact geometry of a retro-reflector. Because of the great intensity of the reflection, its side lobes are visible even 10 m away. No attempt is made to remove this signal since it is located so close to the tree. This is a good example of how nearby features can obscure a tree if they are very bright.

The following chapter investigates these four sets of imagery in more detail.

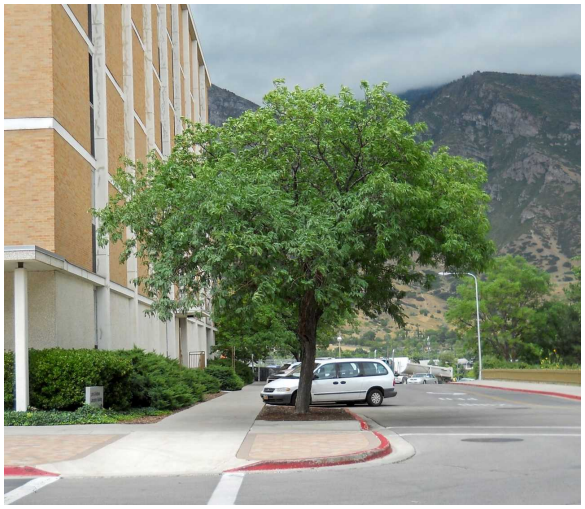

(a) Optical

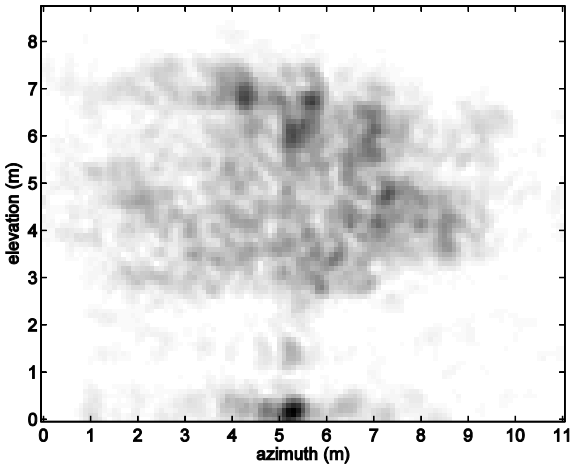

(b) Front view

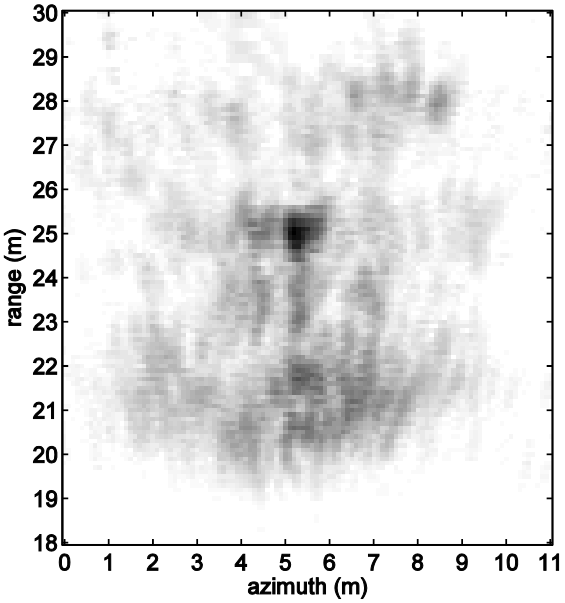

(c) Top view

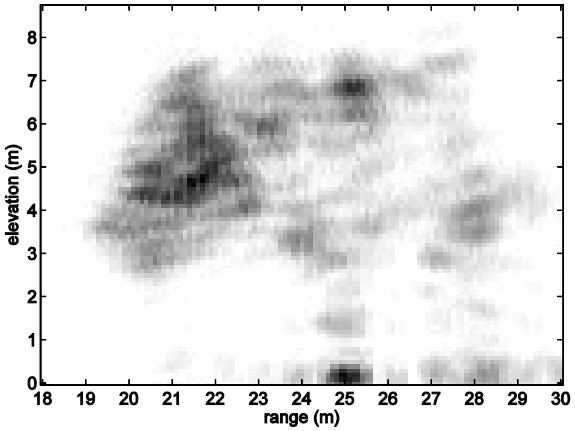

(d) Side view

Figure 5.2: Tree 1 imagery (honeylocust)

(a) Optical

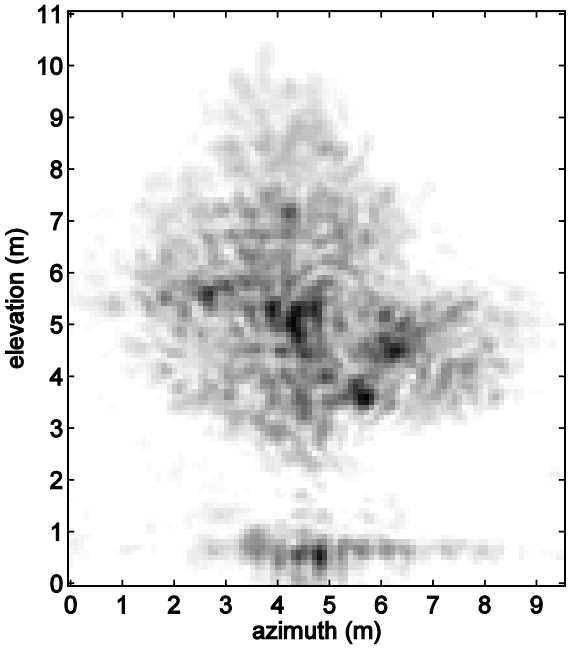

(b) Front view

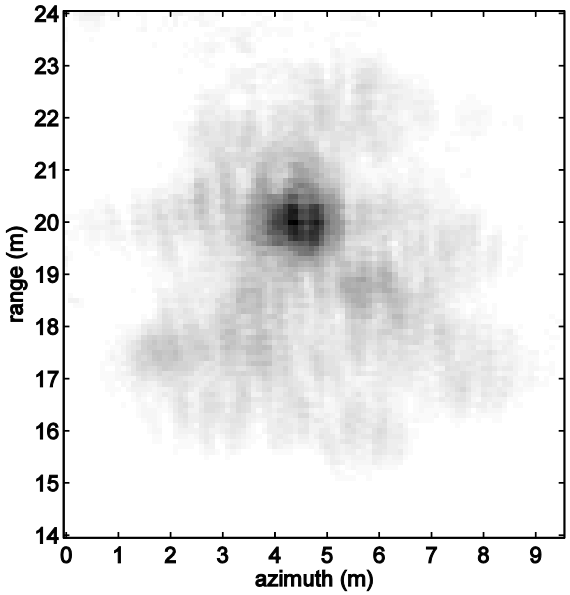

(c) Top view

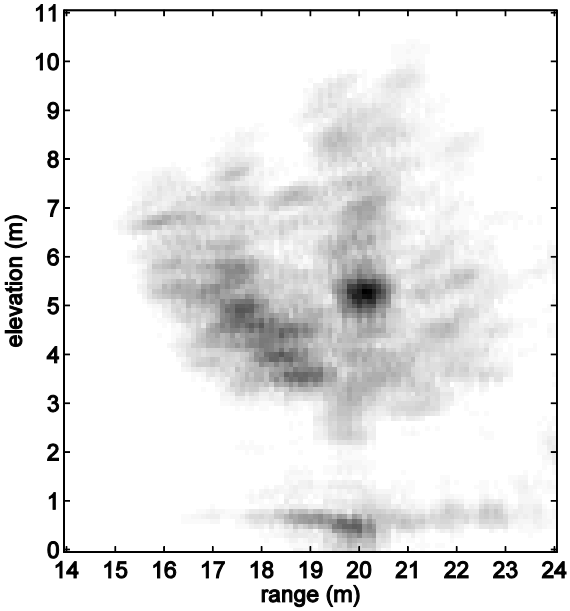

(d) Side view

Figure 5.3: Tree 2 imagery (Norway maple, east view)

(a) Optical

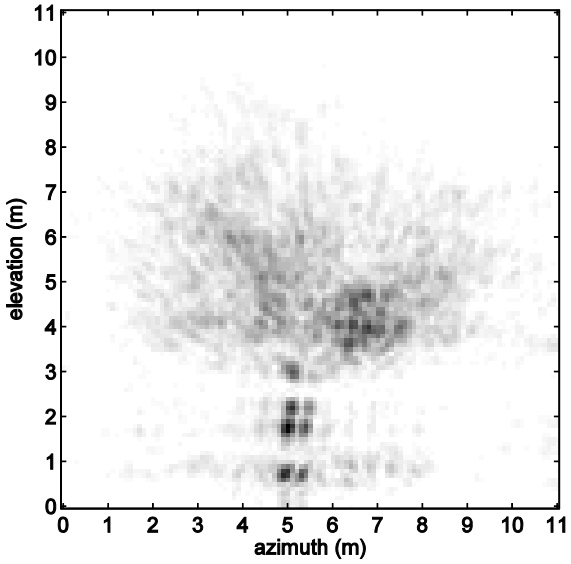

(b) Front view

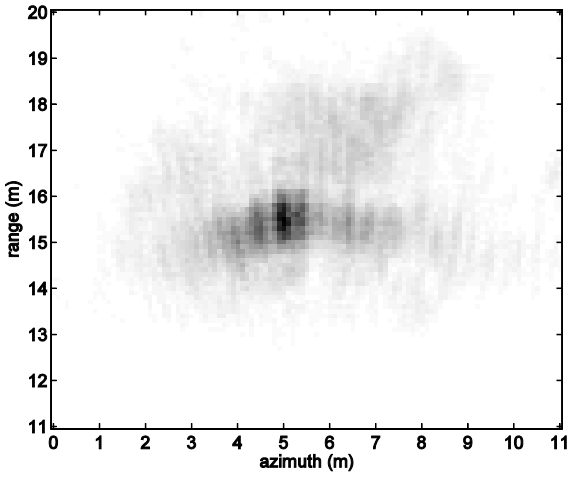

(c) Top view

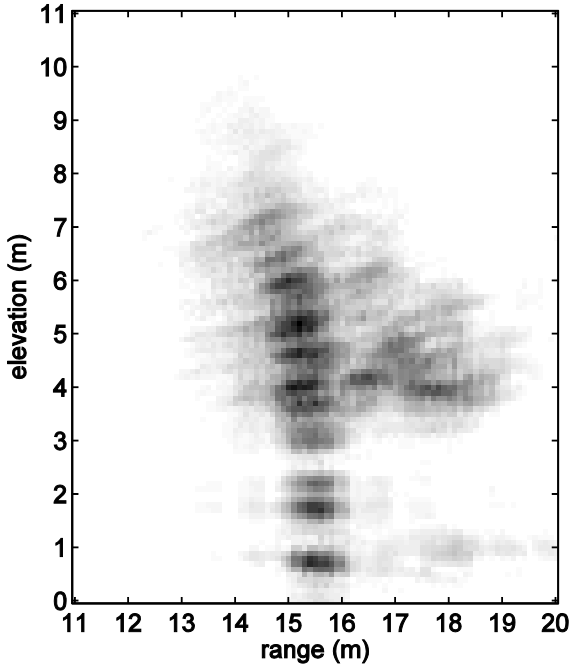

(d) Side view

Figure 5.4: Tree 3 imagery (Norway maple, south view)

(a) Optical

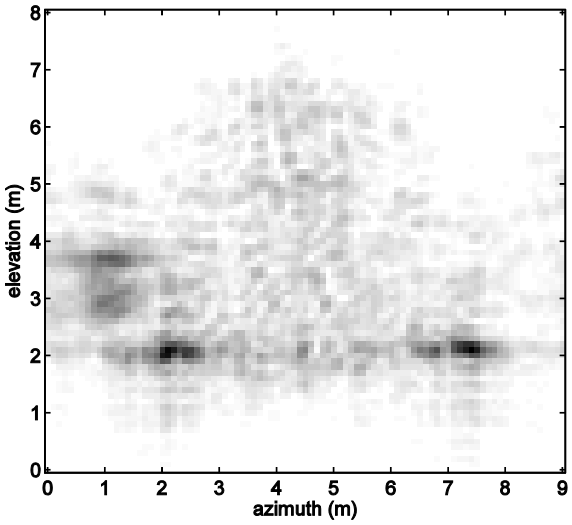

(b) Front view

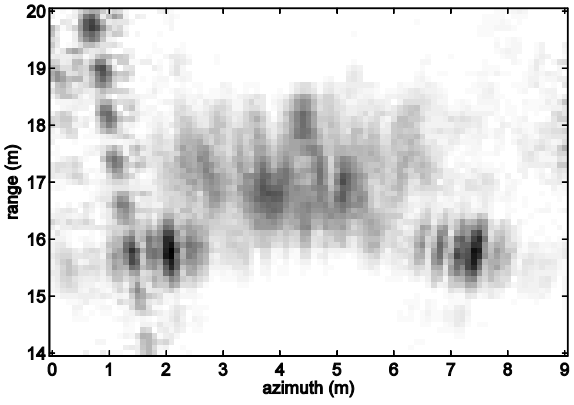

(c) Top view

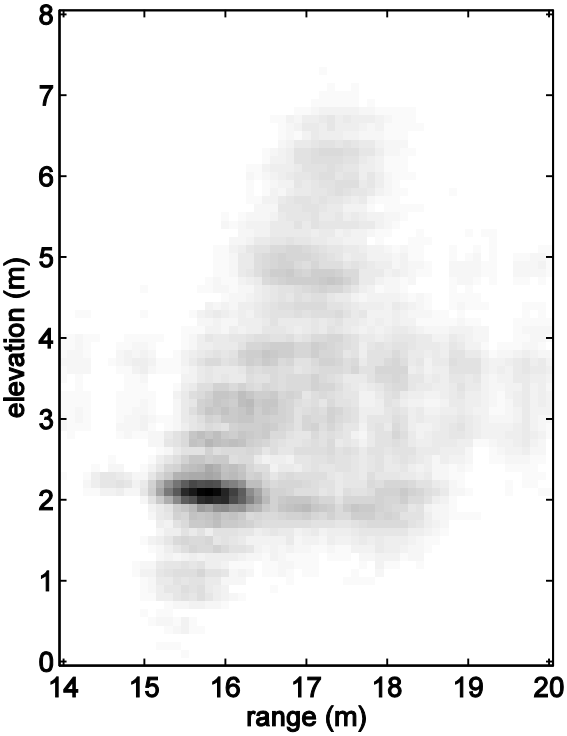

(d) Side view

Figure 5.5: Tree 4 imagery (Colorado blue spruce)

Chapter 6

Imagery Analysis

This chapter provides an analysis of the tree imagery generated from the four experiments described in the previous chapter. In this analysis, the scattering characteristics of the vegetation are investigated including the representations of the different vegetation inclusions, specifically the leaves, branches, and trunk; and also the attenuation behavior of the foliage volume. Another objective of this chapter is to verify the radar scanner's reliability. Since the system is newly built and has had little formal testing, these results indicate whether the system is operating correctly.

In Section 6.1, the 3D reconstruction is evaluated. While the radar imagery is not expected to exactly replicate the physical trees, a resemblance is used to demonstrate successful reconstruction. The radar representations of the leaves, branches, and trunks are investigated. While the trunks are large enough to be resolved by the system's resolution, the leaves and branches are not. However, the branches may produce specular reflections if they create a favorable geometry. For the leaves, fluctuations in density are identified and dimensional measurements (for the foliage as a whole) are compared.

Section 6.2 conducts a repeatability study by comparing the results for the second and third experiments which image the same tree from different azimuth angles. This study is used to demonstrate the system's reliability and to understand a dependency on azimuth incidence angle.

In Section 6.3, the attenuation behavior of the leaves and branches is studied. The attenuation model developed in Chapter 3 is applied to one of the test trees to calculate 3D attenuation data.

Finally, in Section 6.4, data from one of these 3D tree images is used to compute an airborne-SAR-generated 2D tree image. This computation is carried out via a number of

geometric transformations in order to accommodate the frame of reference of an airborne image. The purpose of this study is to: (1) provide traceability for tree features from 2D to 3D and (2) establish that the knowledge gained from the 3D system is applicable to airborne applications.

As a matter of terminology, the phrases "tree image" or "radar tree" or just "tree" are used to specify the radar-generated tree image while the phrases "physical tree" or "optical tree" are used to specify the physical tree. This distinction is made because three physical trees are studied in four tree images.

6.1 Evaluation of the 3D Reconstruction

Based on the images in Figs. 5.2- 5.5 the reconstruction process appears to be effective. Individual leaves and branches are not resolved due to the size of the wavelength, 5 cm, and the system's resolution of 75 cm in range and approximately 40 cm in azimuth and elevation. On the other hand, the image components which are resolved include the trunk, the foliage outline, and density fluctuations within the foliage.

6.1.1 Resemblance to the Physical Trees

Fig. 6.1 provides a side-by-side comparison between the radar and optical images of tree 1 (side views only). In particular, seven feature resemblances are identified and labeled.

1. Four distinct lobes are seen on the top of the profiles. Notice the very small branch sticking out from the right-most lobe which is manifested in the radar image as a very faint patch of signal.

2. The bottom front foliage follows a sideways 'S' curve.

3. The trunk has a forward tilt.

4. A bright localized reflection corresponds to an area of higher vegetation density.

5. The tree center contains a lower density of leaves which corresponds to lower signal return. (The branches located here are poorly visible.)

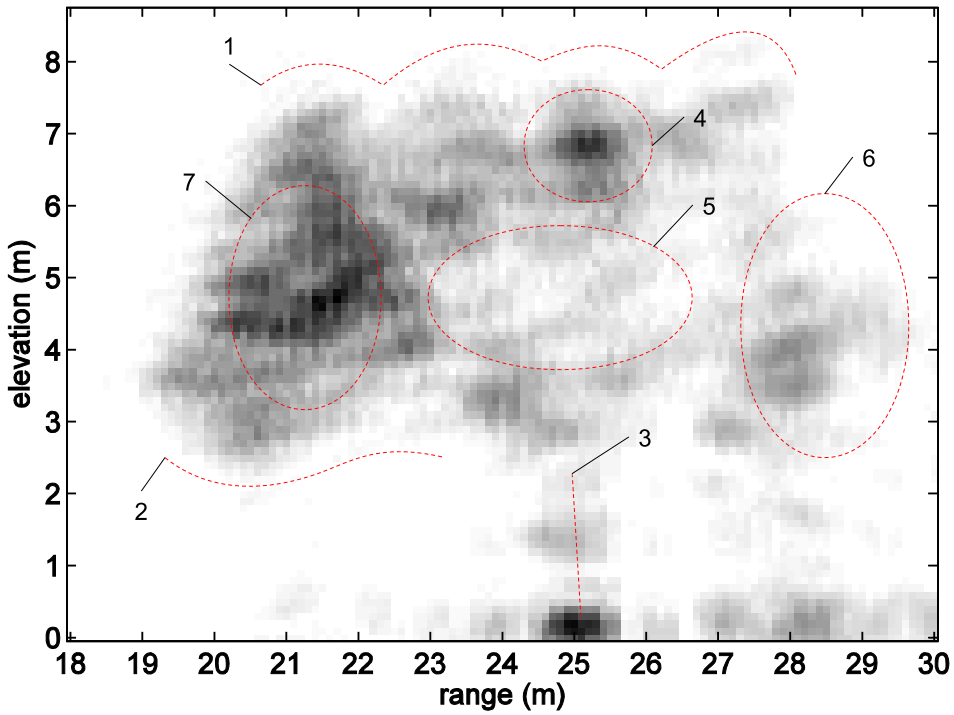

(a) Radar side view

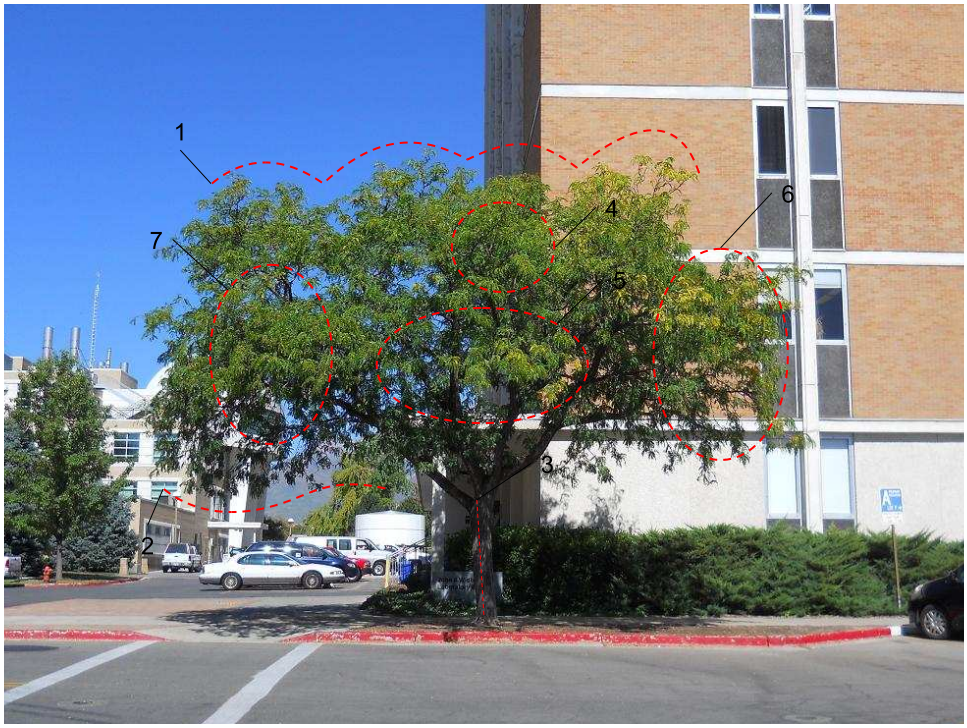

(b) Optical side view

Figure 6.1: Feature-by-feature comparison for tree 1

6. The rear clump of foliage is visible in the radar imagery, although, this seems to defy the principles of attenuation. A possible explanation for its high visibility is the fact that the radar is positioned low to the ground (below 2 m) and may be able to observe the clump by looking up from underneath the foliage.

7. While frontal foliage is generally bright because it is closest to the radar, this particular area is bright because it corresponds to an area of high foliage density.

In Figs. 6.2 and 6.3, trees 1 and 2 are divided into nine, 1 m range slices. This presentation method is used because it enables better isolation of the 3D features, particularly those reflections that are of a local nature.

For both trees, the first slice is small and dim because it contains only a small cross-section at the front of the tree, then the slices become fuller as they progress toward the tree center and as the cross-sections become larger, until the back of the tree is reached where the cross-sections become smaller again and attenuation increases leaving noisy looking images. Notice that the trunk is only visible in one or two of these slices.

Tree 2 is explored first (see Fig. 6.2). In these images, three strong local reflections are circled: two in Fig. 6.2(d) and one in Fig. 6.2(f). In the optical image (Fig. 5.3(a)), these reflections match up with some of the larger branches. The two reflections in Fig. 6.2(d) correspond to branch forking in the physical tree. While these branches are not large, a branch forking with favorable geometry may produce strong retro-reflections. The third reflection, found in Fig. 6.2(f), matches up with the higher end of the trunk. At this particular location, there are a couple of small branches protruding from the trunk in the direction of the radar. Considering the geometry, this appears to create an interior corner facing directly at the radar and is favorable for a strong return.

We next move onto tree 1 found in Fig. 6.3. Here, two local reflections are circled, though they are not especially strong. The reflection in Fig. 6.3(c) can be seen to correspond to significant branch activity which is visible in the optical image (Fig. 5.2(a)). The location of the reflection in Fig. 6.3(e) is not visible in the optical image but its point-like nature indicates that it is likely a specular reflection which is generated from a favorable geometry within the branch network.

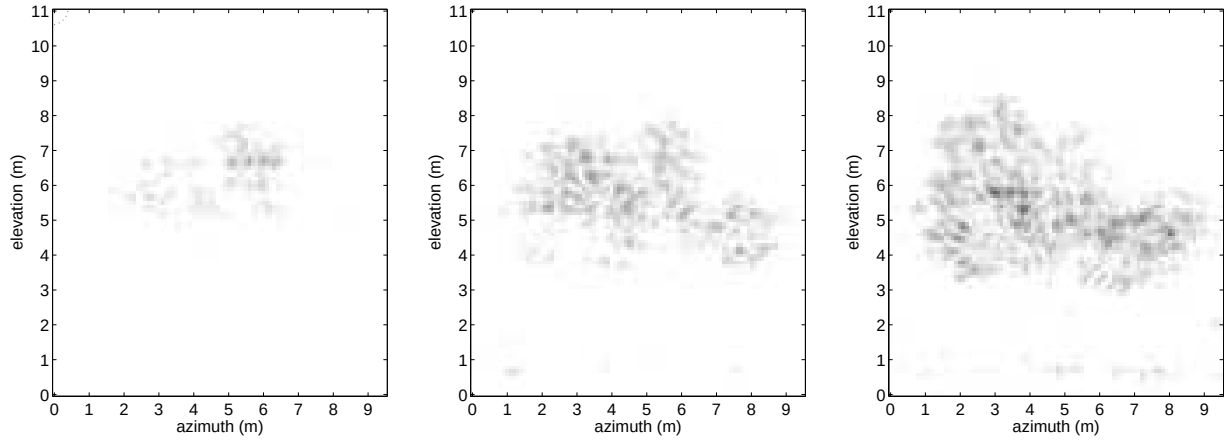

(a) 15 m (b) 16 m (c) 17 m

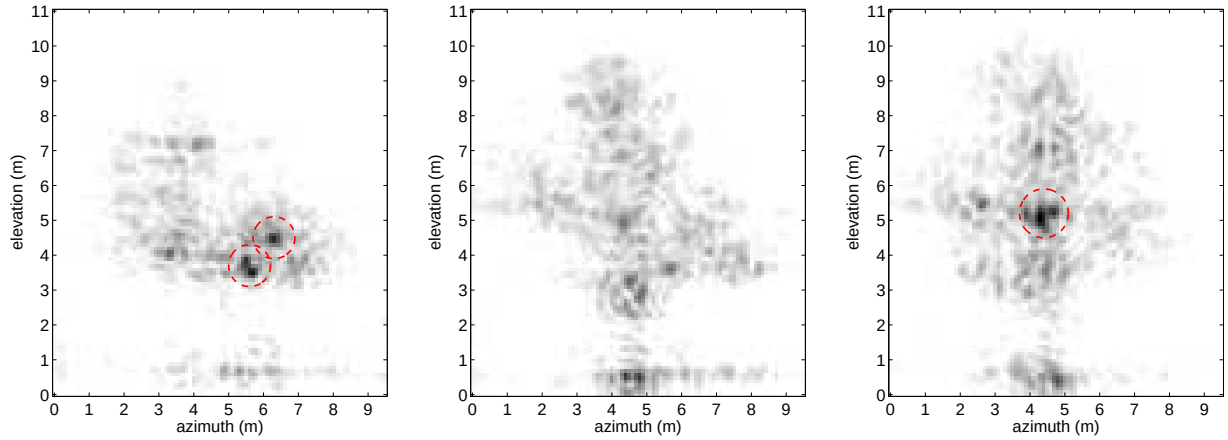

(d) 18 m (e) 19 m (f) 20 m

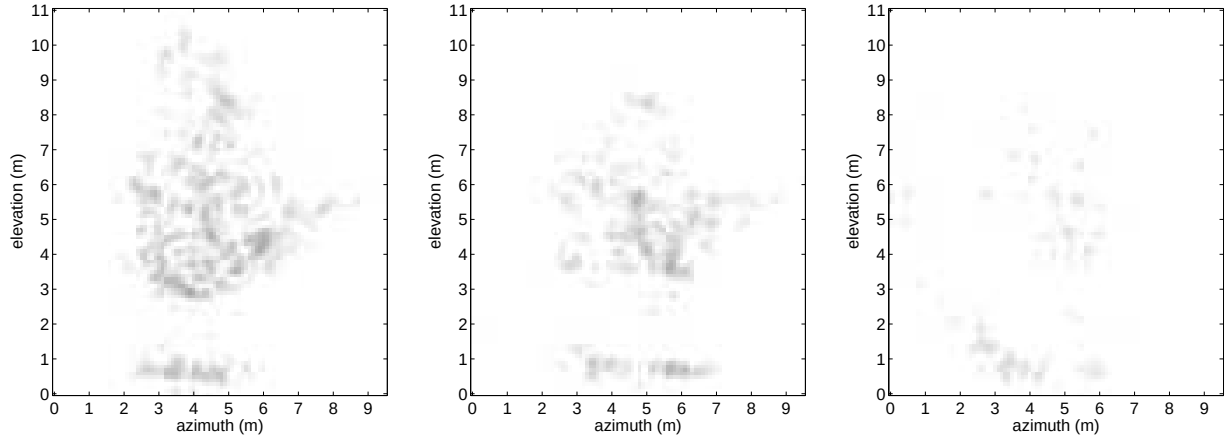

(g) 21 m (h) 22 m (i) 23 m

Figure 6.2: Range slices for tree 2 from 15 m to 23 m. Bright local reflections are circled.

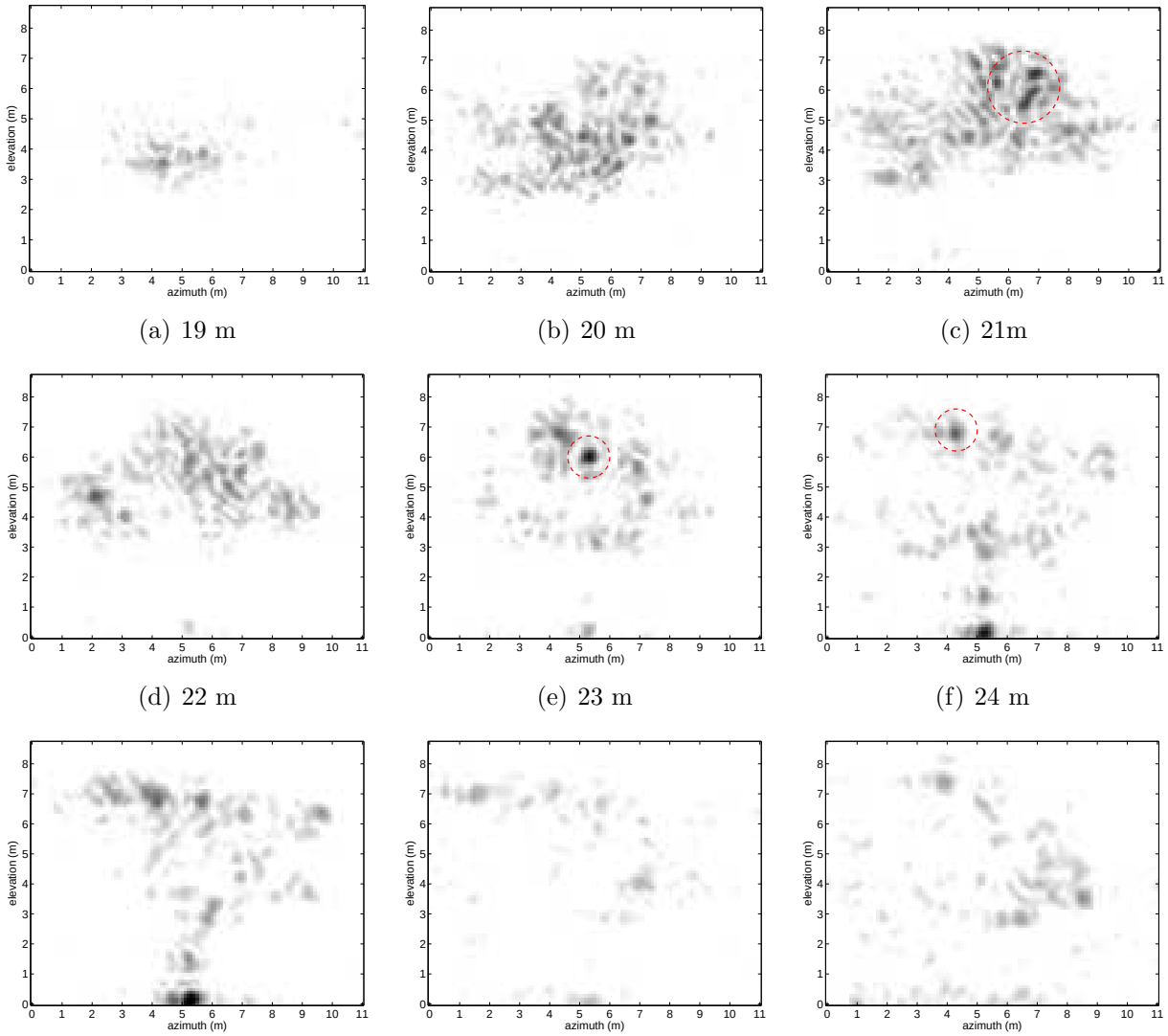

(a) 19 m (b) 20 m (c) 21m

(d) 22 m (e) 23 m (f) 24 m

(g) 25 m (h) 26 m (i) 27 m

Figure 6.3: Range slices for tree 1 from 19 m to 27 m. Bright local reflections are circled.

Surprisingly, Fig. 6.3 shows very little return from lower in the tree where there is an abundance of branches. Part of this issue may be due to orientation. These particular branches make interior corners which face upward and not toward the radar.

6.1.2 Accuracy of Dimensional Measurements

This section investigates the accuracy of the dimensional measurements of the radar-imaged trees by comparing them to measurements of the physical trees. If the radar imagery

is found to underestimate the surveyed measurements, this may suggest that the perimeter leaves are too sparse to be detected. On the other hand, an overestimate may suggest some artificial effect such as side-lobing or simply a lack of resolution.

While acquiring precise measurements from the radar imagery and the physical trees presents some difficultly, measurements are taken with as much care as reasonably possible. Because of noise and resolution constraints, the radar imagery does not provide hard lines to measure from. Therefore, the selection of measuring points is somewhat discretionary. For the physical trees, a theodolite is used for height measurements and a tape measure is used for width measurements.

Five measurements are made for each tree: labeled front, back, left, right, and height (see Fig. 6.4 for the use of these labels). The first four measurements correspond to range or azimuth, using the trunk as a reference point. The height measurement is a measure of the foliage height only. The measurements for each tree are listed in Table. 6.1. The table is somewhat busy, so I will spend some time stepping through it. In the columns are the four trees and in the rows are the five measurement labels. Each table cell uses an $S/R/E$ format where S is the surveyed measurement, R is the radar measurement, and E is the error between the two. Negative error values indicate an underestimation by the radar. Error values larger than 0.5 m are in bold. Since trees 2 and 3 are derived from the same physical tree, their S measurements are the same, though organized differently due to the 90° change in perspective.

The error column tends to show negative values which indicates that the radar imagery consistently underestimates the physical measurements. However, most of the errors

Table 6.1: Foliage measurements for all trees (S/R/E=Surveyed/Radar/Error)

(meters)	Tree 1 S/R/E	Tree 2 S/R/E	Tree 3 S/R/E	Tree 4 S/R/E
Front	6.4/6.0/-0.4	5.1/4.7/-0.4	3.8/2.5/**-1.3**	2.5/2.4/-0.1
Rear	5.5/4.8/**-0.7**	4.3/2.9/**-1.4**	4.5/4.0/**-0.5**	2.3/0.8/**-1.5**
Left	5.1/5.1/0.0	3.8/3.5/-0.3	4.3/3.8/**-0.5**	2.6/2.6/0.0
Right	4.9/4.7/-0.2	4.5/4.3/-0.2	5.1/4.9/-0.2	2.8/2.7/-0.1
Height	5.5/5.4/-0.1	7.8/7.0/**-0.8**	7.8/5.8/**-2.0**	5.3/5.1/-0.1

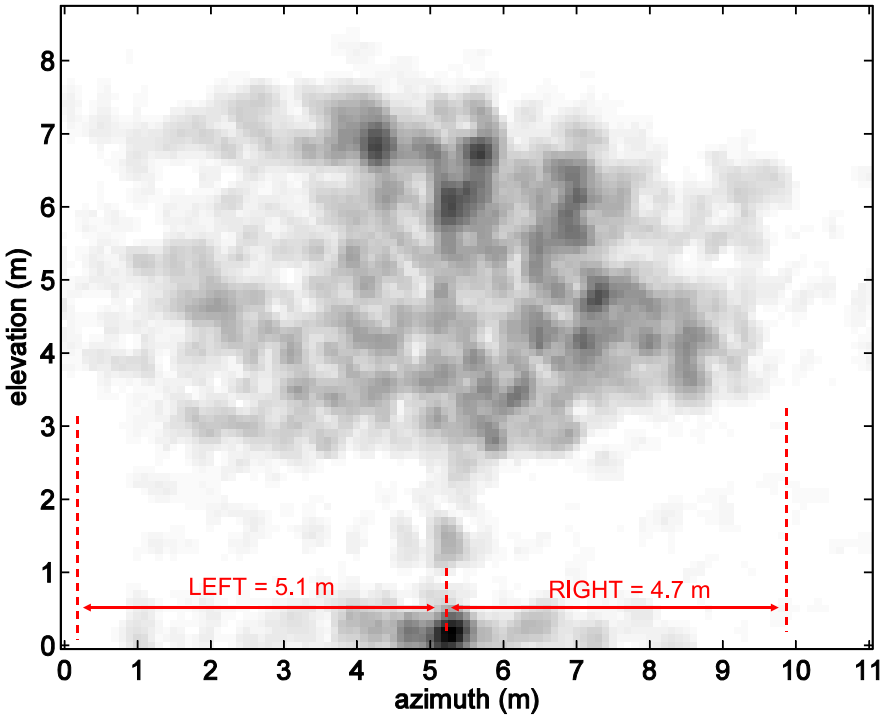

(a) Front view

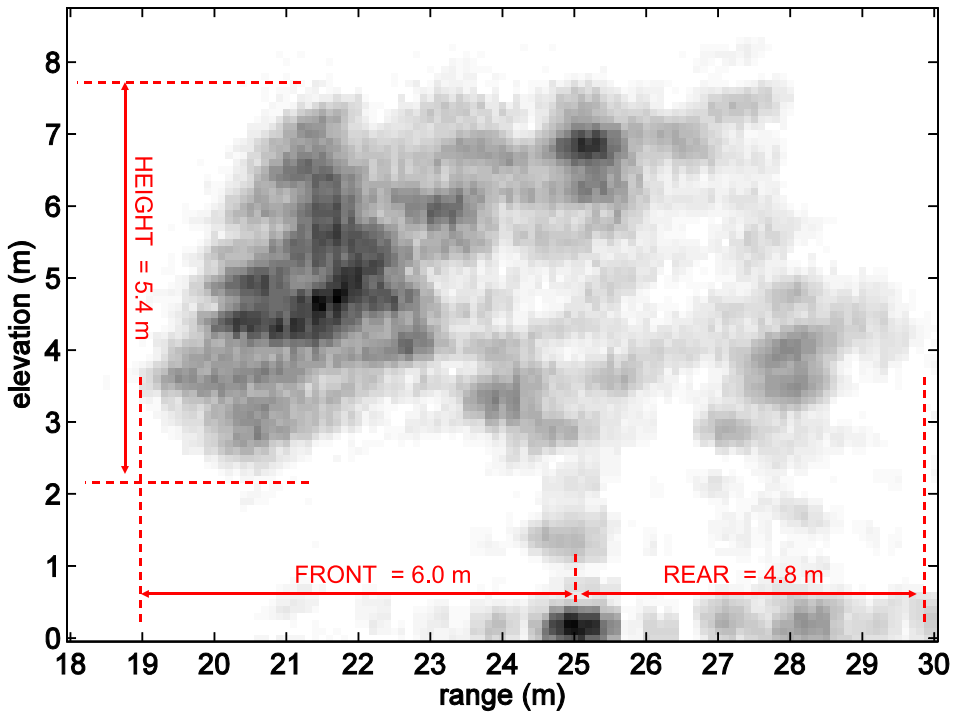

(b) Side view

Figure 6.4: Tree 1 foliage measurements

are small, often only one or two tenths of a meter, and the large errors have reasonable explanations. With one exception, the large errors (boldfaced) fall into the categories of tree 3 measurements or rear measurements. Tree 3 measurements contain error because, as previously observed, tree 3 is poorly reconstructed. The reason some of the rear measurements are off is simply because of insufficient penetration depth. The other instance of a high error is the tree 2 height. Here, it is very possible that the top of this tree is outside of the radar beam, which would be caused by stationing the radar too close.

In sum, the radar measurements tend to underestimate the physical tree dimensions slightly which may be a result of the noise thresholding and a lack of volume scattering from the peripheral leaves. With explained exceptions, the error values show small variance, ranging from 0.0 to 0.4 m. Considering the amount of discretion involved in the measurement acquisition process, these values demonstrate very good consistency.

6.1.3 Trunks

From Section 3.4.2 we learned that trunk scattering is categorized into three types: specular reflections from the trunk surface, corner reflections from the intersection of the trunk with the ground, and multi-path reflections from off the ground.

The trunks for all trees are compared in Fig. 6.5. These images are 1 m range slices so that each trunk is better isolated. The general trend in these images is that the trunk base is very bright while the midsection is dim and, in some cases, splotchy. In particular, notice the trunk base in Fig. 6.5(a) which is easily the brightest feature in the image. The brightness of the trunk base is a result of the strong corner reflections.

Further testing is required to understand the details of the specular and multi-path scattering. Because these trunks are normal facing, the specular reflections from the trunk midsection is visible, but this may change with an alternate orientation. Multi-path reflections may be the cause of the midsection appearing splotchy, but this is difficult to determine with only the few tests that have been performed.

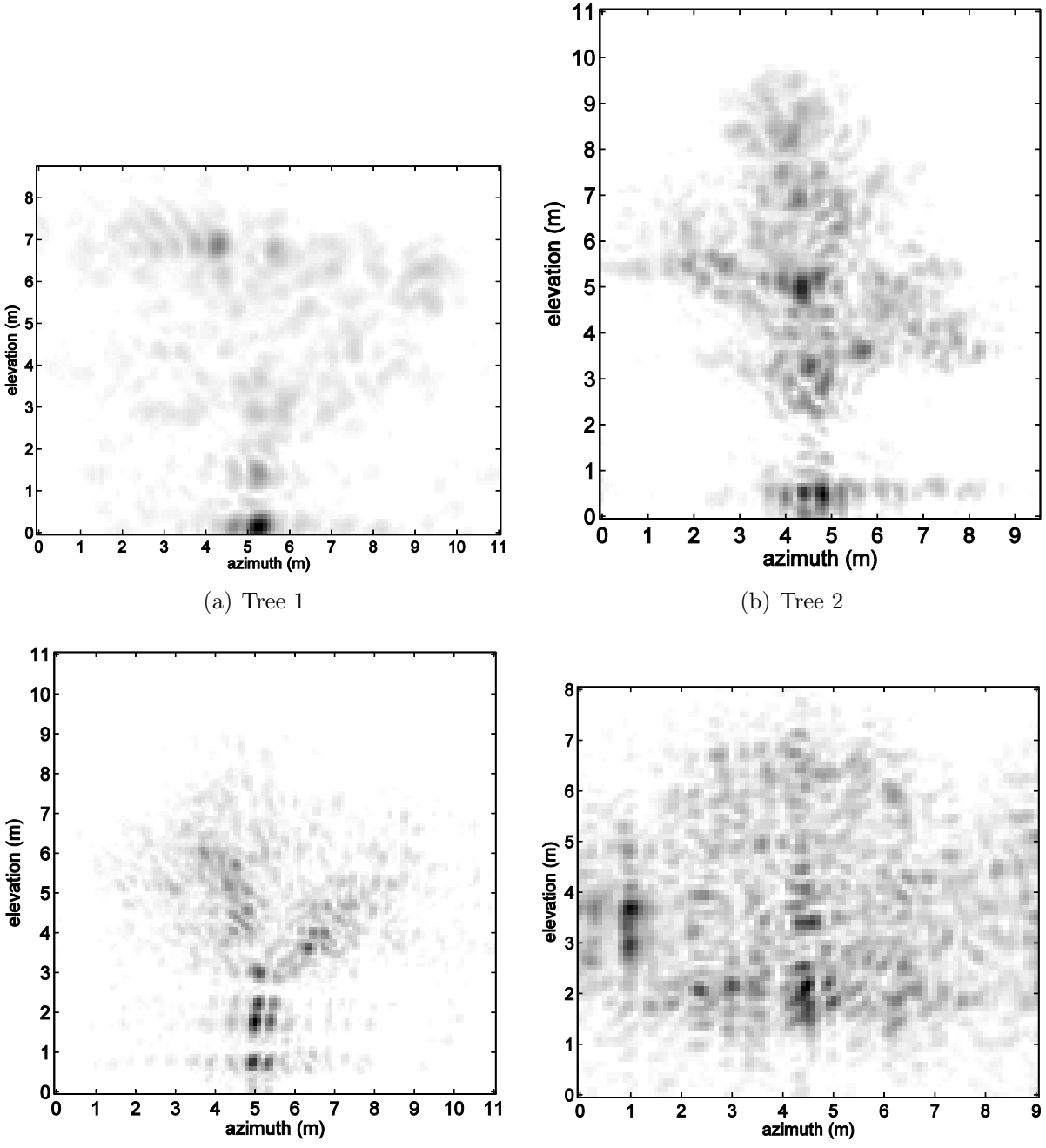

(a) Tree 1

(b) Tree 2

(c) Tree 3

(d) Tree 4

Figure 6.5: Trunks of all trees. Images consist of approximately 1 m range slice.

6.2 Repeatability Study

Repeatability is studied by comparing results from the second and third experiments, which are associated with the same physical tree but offset by 90°. Because the perspectives are right angles from each other, the imagery is easily compared by switching the azimuth and range axes. This study is used to demonstrate the system's reliability and to understand a dependency on azimuth incidence angle. To demonstrate reliability, similarity in feature location, feature representation, and foliage measurements is evaluated.

There may be differences resulting from the change in incidence angle. For example, previous discussions have already suggested that branch responses are orientation dependent. The foliage, on the other hand, is not orientation dependent since it is a volume scatterer. However, a change in its response would indicate that it deviates from the volume scattering model to some degree. The occurrence of any of these differences is useful knowledge.

During this comparison, two ideas are important to keep in mind. First, the images are not corrected for attenuation. This means that different parts of each tree are attenuated based on the respective incidence angle. Second, tree 3 is poorly reconstructed which hinders the effectiveness of this study.

This comparison begins with Fig. 6.6. In this figure, the first column contains east-facing views and the second column contains south-facing views. For rows, the first contains tree 2 imagery, the second contains tree 3 imagery, and the third contains optical imagery. The optical imagery is included as a reference. Remember that this study is about the resemblance of the two radar observations so the resemblance to the optical images is not as important. In this figure, we expect to find a resemblance between (a) and (c) as well as between (b) and (d). Unfortunately, these images contain many large differences. For example, (c) has a very pronounced backbone-like feature which may be some type of aliasing. Also, (d) has a disintegrating-like texture as the foliage extends outward. Finally, both (c) and (d) are missing large chunks of signal and therefore the overall dimensions are off. On the other hand, a number of similarities are observable. One is that (a) and (c) share the protruding foliage clump on the right side. Ones shared by (b) and (d) include: sharing a bright reflection just above and right of the trunk, the trunks having a rightward tilt, and

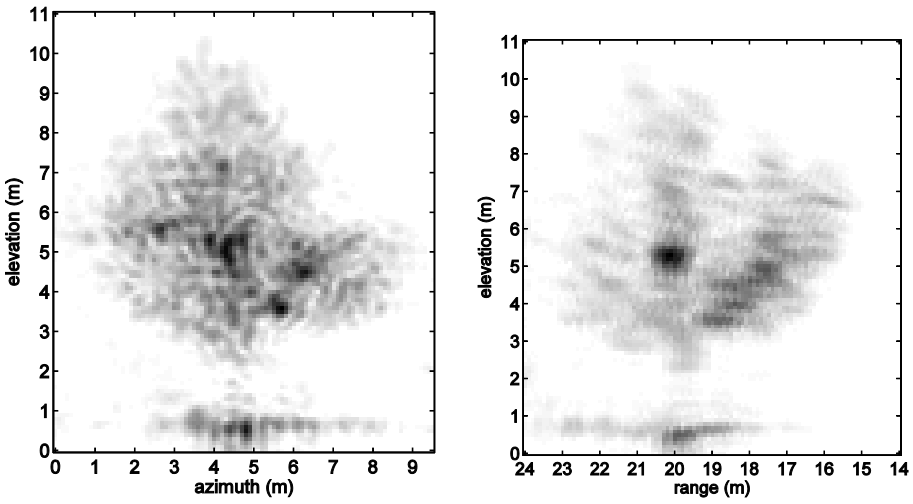

(a) Tree 2 east face

(b) Tree 2 south face

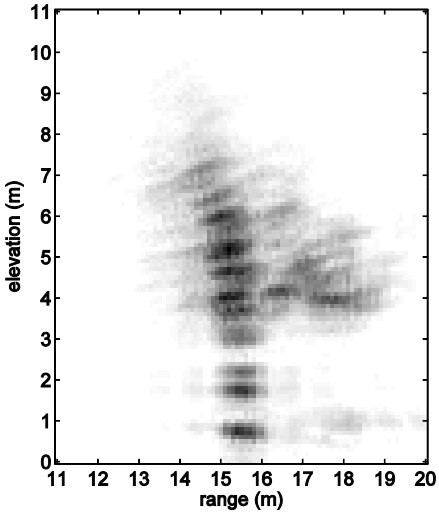

(c) Tree 3 east face

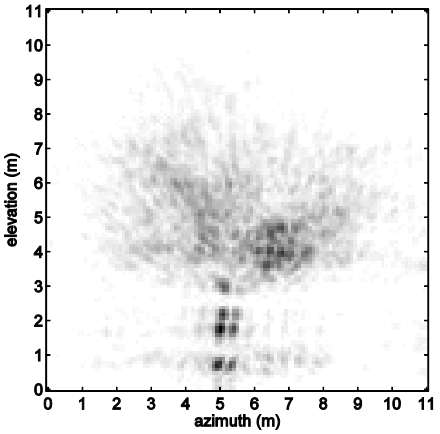

(d) Tree 3 south face

(e) Optical east face

(f) Optical south face

Figure 6.6: Side view comparison of trees 2 and 3

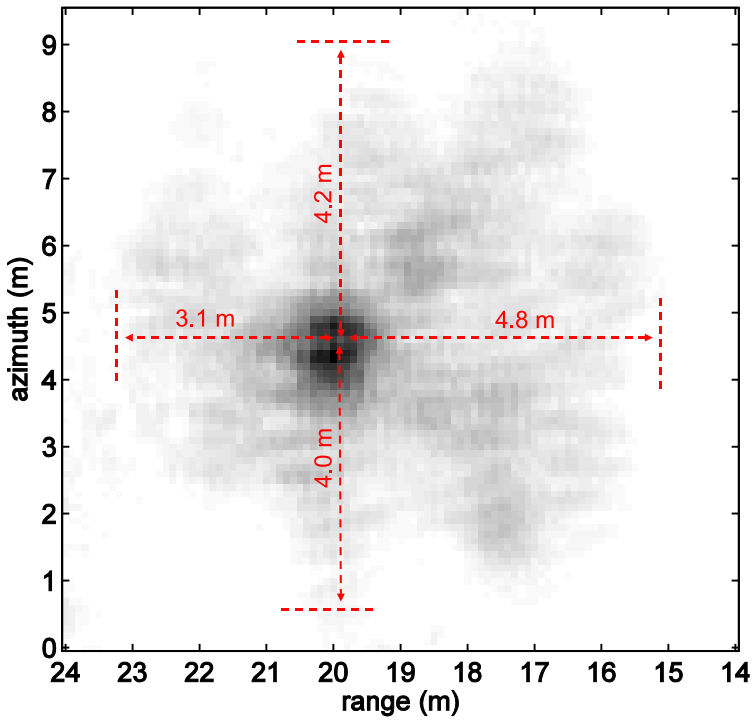

(a) Tree 2 top view

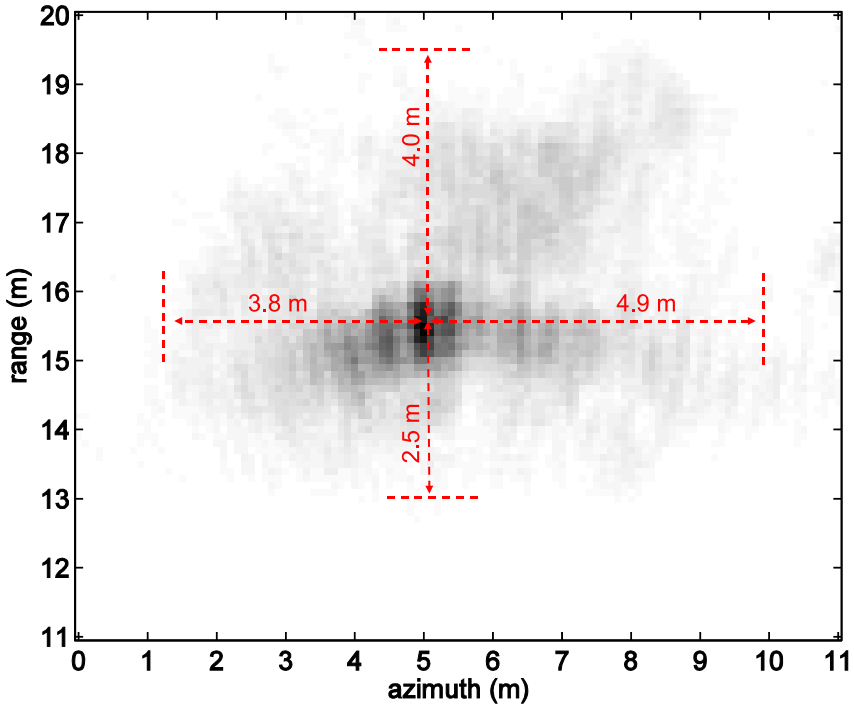

(b) Tree 3 top view

Figure 6.7: Top view comparison of trees 2 and 3

to some extent, reproducing the gap in the upper right foliage (seen clearly in the optical image).

Moving on, Fig. 6.7 contains top views of each tree. Unlike the previous figure, no optical image is available for comparison. The images are oriented so that north is toward the top of the page (causing the azimuth and range axes to disagree). While at first glance these images appear very different, there is an interesting observation to be made. That is, the degree of similarity improves moving toward the north side. For instance, notice the capture of the protruding foliage in the north-east corner. Also, except for the south, the measurements are broadly similar. The west measurement is off only due to insufficient penetration for tree 2. This observation re-enforces our belief that the tree 3 distortions are a result of the radar being stationed too closely in range.

Unfortunately, there are too many distortions present in tree 3 for this study to be effective. For better results, experiments should be performed with at least 20 m of range. Also, it would be worth while to correct for attenuation as illustrated in the following section.

6.3 Attenuation Study

In this section, the attenuation model developed in Section 3.1.4 is used to calculate attenuation data for one of the test trees. Since this data is 3D, it has an advantage over traditional attenuation measurements. Typically, attenuation is measured by placing antennas on both sides of a volume. This setup provides only an attenuation rate and does not account for local fluctuations in attenuation behavior. Conversely, the 3D attenuation data is calculated on a per voxel (3D pixel) basis using 3D empirical data. This is more appropriate for trees since a tree is rarely uniform in density. Generally, the center of a tree has a lower concentration of leaves and a higher concentration of branch material; while the perimeter of a tree is the reverse.

A few assumptions are made about the physical tree during these calculations as a result of using an uncalibrated radar. One assumption is that the physical tree possesses balanced density (though it need not be uniform). Another assumption is that the extinction and scattering cross-sections (σ_e and σ_s) are proportional to each other throughout the tree. These assumptions are explained as the discussion progresses.

In Section 3.1.4, attenuation is modeled by

$$L(z,\phi,\theta) = \exp\left(-\int_0^z \kappa_e(z',\theta,\phi)dz'\right). \tag{6.1}$$

While this equation describes the theory, several modifications must be applied before it can be useful for this application. For example, it must accommodate a discrete voxel space, be expressed in terms of known variables, and account for the multiple observations made by the antennas.

To accommodate a discrete voxel space, the integral is changed to a summation and the polar coordinates are converted to rectangular voxel coordinates

$$L(i,j,k) = \exp\left(-\frac{1}{\cos(\phi)\cos(\theta)}\sum_{k'=0}^{k}\kappa_e(i',j',k')\right) \tag{6.2}$$

where $i' = \frac{k'}{k}i$, $j' = \frac{k'}{k}j$, $\phi = tan^{-1}(\frac{i}{k})$, and $\theta = tan^{-1}(\frac{j}{k})$. The cosine terms in the denominator result from the change in summation limits (from z to k).

Values for κ_e are not directly available, but κ_e can be related to P_r through the radar equation if we assume $\kappa_s = a\kappa_e$ where a is a proportionality constant. This relationship is given by

$$\kappa_e = AP_r \tag{6.3}$$

where

$$A = \frac{(4\pi R^2)^2}{P_t A_r G_t a G_s}$$

and G_s is the scatterer gain. Substituting Eq. (6.3) into Eq. (6.2) yields

$$L(i,j,k) = \exp\left(-\frac{A}{\cos(\phi)\cos(\theta)}\sum_{k'=0}^{k}P_r(i',j',k')\right) \tag{6.4}$$

where A is moved out of the summation since it is a constant value.

Because the system employs a moving antenna to form the synthetic aperture, the blockage experienced by each voxel is from more than a single direction. Specifically, blocking voxels form a pyramid shape which is oriented so that the pyramid base comprises the

antenna scanning pattern and the pyramid tip comprises the incident voxel. This behavior does not change Eq. (6.4) as long as P_r is understood to be the average value of the pyramid slice at the given depth. To recognize this discrepancy, P_r is changed to P'_r. Thus the final form given to the attenuation loss factor L is

$$L(i,j,k) = \exp\left(-\frac{A}{\cos(\phi)\cos(\theta)}\sum_{k'=0}^{k} P'_r(i',j',k')\right). \tag{6.5}$$

Determining an appropriate value for A requires a method for measuring error. This method is as follows. Equation (6.5) is applied to the original tree image (P_{rv}) to generate an unattenuated tree image (P_r) for some value of A. The P_r image data is averaged along azimuth and elevation and plotted against range (see Fig. 6.8(d)). Error is then determined by measuring the squared-error between this P_r curve (which represents range-averaged attenuation-removed voxel values) and a zero-slope curve (which represents a uniform-density zero-attenuation tree model). This method is repeated for a range of A values and the one which produces the least error is selected.

A few comments regarding this method follow: First, an assumption is made that the physical tree is symmetrically balanced so that there is no increasing or decreasing trend in density. This assumption is required for the zero-slope model to apply. Note this does not require the density to be uniform throughout, however. Secondly, there is a slight inaccuracy in assuming that the range axis is equivalent to penetration depth z. The differences are that the scanner's viewing angle is slightly up-looking and the tree does not have a flat incident surface. However, this should have only a small effect on the result. Thirdly, the P_r averaging incorporates only the foliage voxels and not the empty voxels surrounding the tree which would greatly bring down the average. This is accomplished by tediously constructing 3D mask to mirror the foliage volume.

Removing Attenuation

Attenuation is removed by dividing L out of the original image data P_{rv} using the equation

$$P_r(i,j,k) = P_{rv}(i,j,k)L^{-2}(i,j,k). \tag{6.6}$$

Note that these labels, P_r and P_{rv}, are the same as those used in Eqs. (2.7) and (3.9). In those equations, P_{rv} represents the received power from an embedded volume scatterer and P_r represents the received power from an unobstructed scatterer. The 2 in the exponent is used since attenuation is two-way. Expanding the previous equation results in

$$P_r(i,j,k) = P_{rv}(i,j,k)\ \exp\left(\frac{2A}{\cos(\phi)\cos(\theta)}\sum_{k'=0}^{k} P'_r(i',j',k')\right). \tag{6.7}$$

At first glance, this equation may seem circular since P_r appears on both sides; however, the P_r on the left refers to the incident voxel while the P_r on the right refers to the blocking voxels. Therefore, this equation works fine as long as it is used recursively so that the blocking voxels are calculated prior to the incident voxel. In other words, the order of voxel calculations must proceed from front to back.

Case Study 1: Honeylocust

These calculations are performed on Tree 1 and the results are provided in Fig. 6.8. Tree 1 is selected because it demonstrates the best total visibility. Figures 6.8(b) and (d) contain the range averaged curves for the original (P_{rv}) and compensated (P_r) trees respectively. The P_{rv} curve shows a downward trend which indicates a decrease in received power and the presence of attenuation. On the other hand, the P_r curve follows a straight line, indicating that attenuation is not present. Observe that the P_r tree image (shown in (c)) appears more balanced. However, the foliage clump in the rear is still brighter than it should be and as expected the noise at the back of the tree has been accentuated. Finally, (e) provides squared-error as a function of A. This plot contains A-values ranging from 0.9x10^{-3} to 1.4x10^{-3} and demonstrates a trough which bottoms out at A=1.24x10^{-3}.

Attenuation L is calculated using the P_{rv} and P_r data and by rearranging Eq. (6.6):

$$L(i,j,k) = \left(\frac{P_{rv}(i,j,k)}{P_r(i,j,k)}\right)^{1/2}. \tag{6.8}$$

Applying this equation results in a 3D attenuation map for which side and top views are provided in Fig. 6.9. Observe that attenuation accumulates at different rates depending

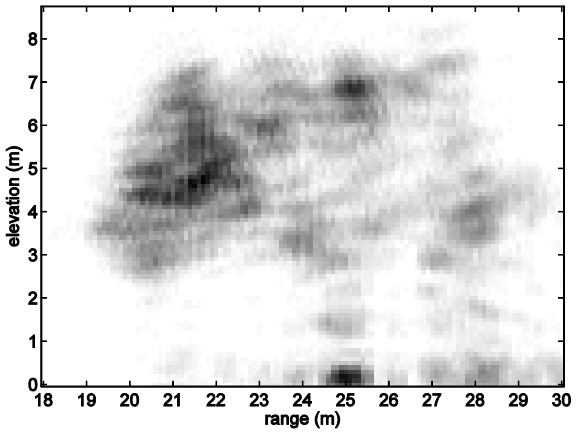

(a) Tree image before attenuation is removed (P_{rv})

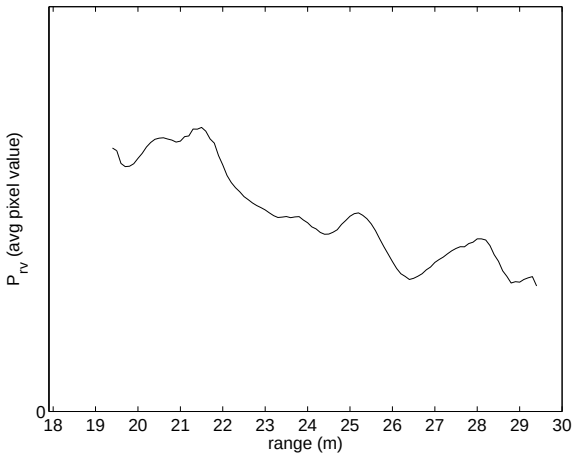

(b) P_{rv}(avg) versus range

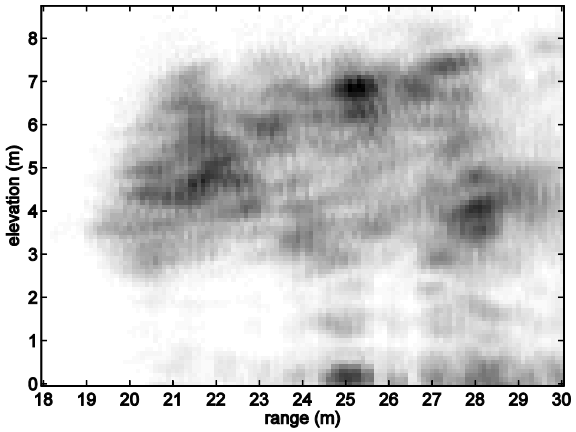

(c) Tree image after attenuation is removed (P_r)

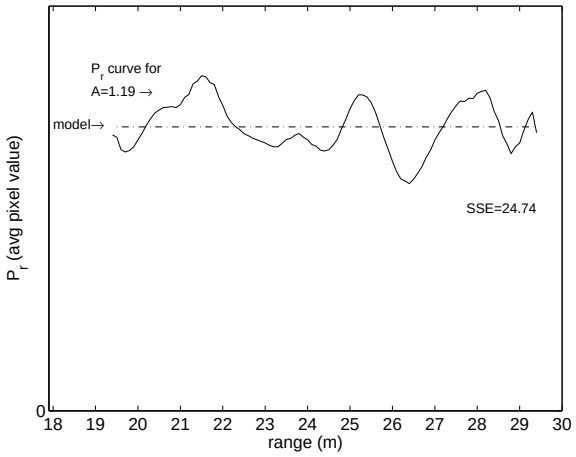

(d) P_r(avg) versus range. The dotted line represents the model for which error is measured against.

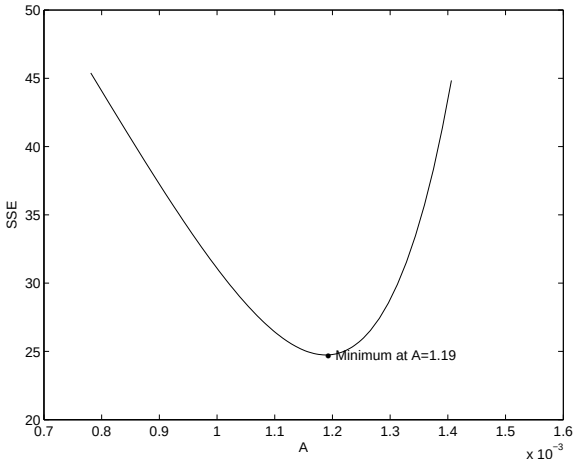

(e) Squared error as a function of the A modeling constant

Figure 6.8: Results from removing attenuation

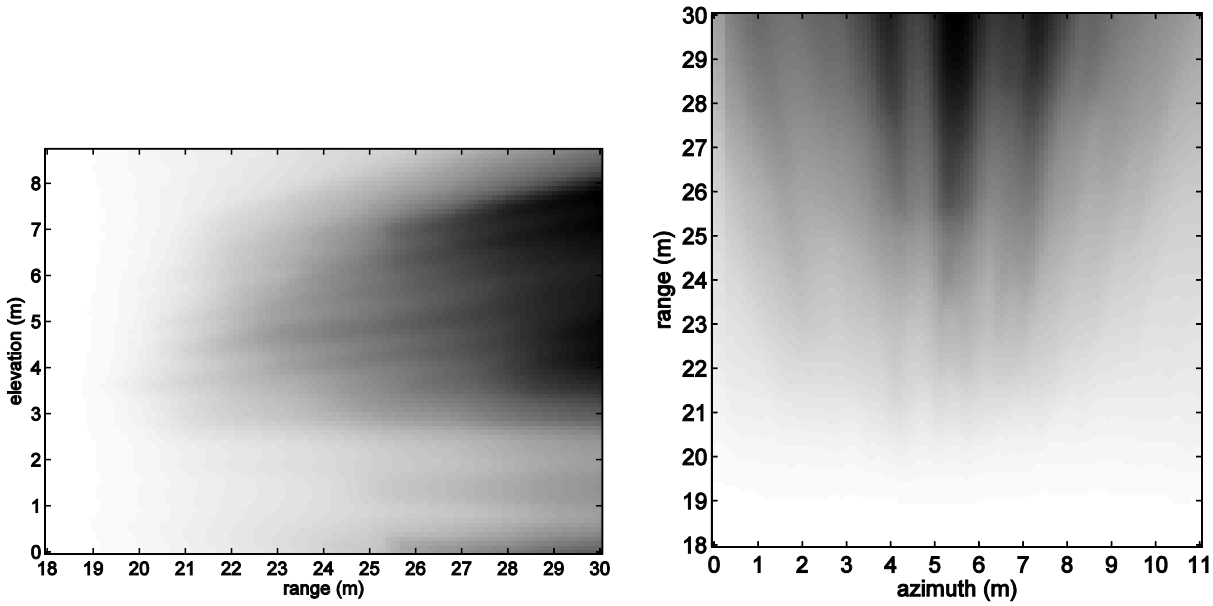

(a) 3D attenuation map L (side view)

(b) 3D attenuation map L (top view)

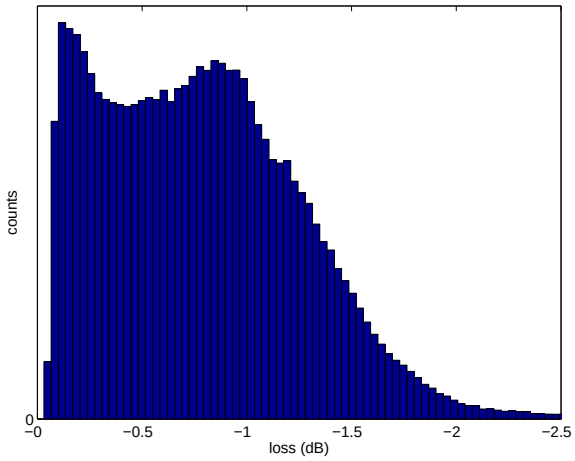

(c) Histogram of 3D attenuation values

Figure 6.9: Attenuation data for tree 1. Values reach up to approximately 1.7 dB at the rear of the tree.

on where the dense parts of the tree are and also that the perspective of the radar is very evident.

Figure 6.9(c) contains a histogram of 3D attenuation values. This representation is more effective than plotting the attenuation values against range, since range does not exactly correspond to penetration depth z (as discussed earlier). The histogram indicates that attenuation values reach up to approximately -1.7 dB (or -3.4 dB when considering both directions) at the rear of the tree.

Calculating $\boldsymbol{\sigma_v}$

Backscattering cross-section σ_v is related to P_r through the radar equation of Eq. (2.7) and is thus calculated by

$$\sigma_v = \frac{(4\pi R^2)^2}{P_t A_r G_t} P_r. \tag{6.9}$$

Unfortunately, this calculation is only possible with a calibrated radar since it relies on knowledge of radar parameters such as transmit power P_t and antenna gain G_t. At most, we know that σ_v is related to P_r by a constant value and that the image in Fig. 6.8(c) represents a scaled version of σ_v from which we can identify trend behavior.

If values of σ_v were available, we could approximate individual backscattering cross-sections for leaf and branch (σ_l and σ_b) using

$$\sigma_v = \sigma_l \rho_l + \sigma_b \rho_b. \tag{6.10}$$

Acquiring density values ρ_l and ρ_b requires counting individual leaves and branches in the physical tree; however, this information was not available.

Case Study 2: Spruce

The previous calculations are effective only if the physical tree is reasonably balanced in density (in range) and if the tree image exhibits total visibility. While the imagery for the spruce (tree 4) does not exhibit total visibility (and thus the previous calculations cannot be effectively applied) some general observations are made here for the purpose of comparing the attenuation behavior of a contrasting foliage type.

(a) Honeylocust leaflets (tree 1)

(b) Spruce needles (tree 4)

Figure 6.10: Honeylocust and spruce foliage samples

Fig. 6.10 provides photos of leaf samples from the honeylocust (corresponding to tree image 1) and the spruce (corresponding to tree image 4). Two factors are expected to strongly influence the amount of attenuation, or backscatter, experienced for each tree: leaf size and foliage density. A small leaf size should have a negative effect on backscatter and lead to low attenuation. This is because leaves which are much smaller than the incident wavelength produce mostly Rayleigh scattering for which backscatter decreases with target size (see Fig. 3.1). Foliage density, on the other hand, has a positive effect on backscatter and lead to high attenuation (see Eq (3.4)). A honeylocust leaflet is about ten times larger than a spruce needle with an area of about 2 to 5 cm^2 compared to 0.2 to 0.5 cm^2 respectively. However, the spruce has a larger overall foliage density. From the radar imagery (Figs. 5.2 and 5.5) it is easy to see that attenuation in the spruce is much greater due to the decreased depth of penetration. This indicates that the spruce's foliage density has a larger effect on the total backscatter than do the size of its needles.

6.4 Airborne-SAR Correlation Study

As promised, a computation is performed in which a 3D tree image is taken through a number of geometric transformations to convert the ground-based frame of reference to a 2D-airborne-SAR frame of reference (see Fig. 2.8 for a diagram of the airborne-SAR acquisition

geometry). The purpose of this computation is to: (1) provide traceability for tree features from 2D to 3D, and (2) establish that the knowledge gained from the 3D system is applicable to airborne applications.

The necessary transformations are determined by considering the differences between the 3D system and an airborne system. Three fundamental differences include incidence angle, image dimensionality, and operating range while operating frequency is matched for both systems. Operating range is disregarded because it only influences SNR, not the scattering behavior. Accordingly, this computation only accounts for changes in incidence angle and dimensionality. To account of the change in incidence angle, attenuation is removed using the perspective of the 3D ground-based system and then restored using the new airborne perspective. To account of the change in dimensionality, 3D to 2D projection is performed. To agree with airborne methods, this projection ensures that similar range measurements are kept together. These transformations are explained in more detail next.

A weakness of this computation is that it does not account for changes in scattering behavior resulting from the change in elevation incidence angle. For example, since a trunk is less normal facing from overhead, it returns less specular reflections. Also, the core branching has a relatively fixed orientation which may be more favorable to upward scattering. Nevertheless, these differences are not anticipated to affect the results to a significant extent.

6.4.1 Implementing the Computation on Tree 1

To reiterate, the steps in this computation are the following:

1. Remove attenuation using the perspective of the 3D ground-based system.

2. Restore attenuation using the elevated perspective of an airborne SAR system.

3. Project from 3D to 2D while keeping similar range measurements together.

This computation is implemented on tree 1 and each stage is documented in Fig. 6.11. Side views are used in this figure because they illustrate the attenuation behavior. Note that the images in the figure are thresholded to make them more viewable while the images used

as inputs to the computation are not thresholded so that the dimmer areas of the tree are brought out. I note that shadowing on the ground from the tree has not been included in the transformed 3D-SAR image.

The process of attenuation removal is detailed in Section 6.3. For a voxel located at (i, j, k), attenuation removal is given by

$$P_r(i,j,k) = P_{rv}(i,j,k)\ \exp\left(\frac{2A}{\cos(\phi)\cos(\theta)}\sum_{k'=0}^{k} P'_r(i',j',k')\right) \tag{6.11}$$

where P_{rv} is the original image data and P_r is the attenuation-removed image data. This equation is applied to each voxel in the original image beginning at the front. The resulting unattenuated image is shown in Fig. 6.11(b).

Attenuation restoration is performed in a reverse manner as attenuation removal. For this operation, Eq. (6.7) is rearranged to give

$$P_{rv}(i,j,k) = P_r(i,j,k)\ \exp\left(-\frac{A}{\cos(\phi)\cos(\theta)}\sum_{k'=0}^{k} P'_r(i',j',k')\right) \tag{6.12}$$

where A is carried over from the remove equation. Notice the reversal of P_r and P_{rv} and also the change in sign in the exponential term. One other change is how the blocking voxels P'_r are determined. Besides a change in incidence angle, there is also a change in the scanning pattern. Specifically, the scanning pattern changes from 2D to 1D which leads to a triangle shape for P'_r opposed to a pyramid shape.

Similar to attenuation removal, this equation is applied to each voxel. However, this procedure is not recursive, which is evident by the fact that the term being solved is found only on the left side of the equation. That means that the blocking voxels are composed of old, not new, values and the algorithm is not required to begin at the front of the tree.

The result of the attenuation restoration step is found in Figure 6.11(c) where an incidence angle of 50° is used. Notice that the top front region of the tree is fairly unaffected while the features in the bottom rear have experienced more attenuation. For example, the rear clump has dimmed slightly and the trunk has dimmed considerably.

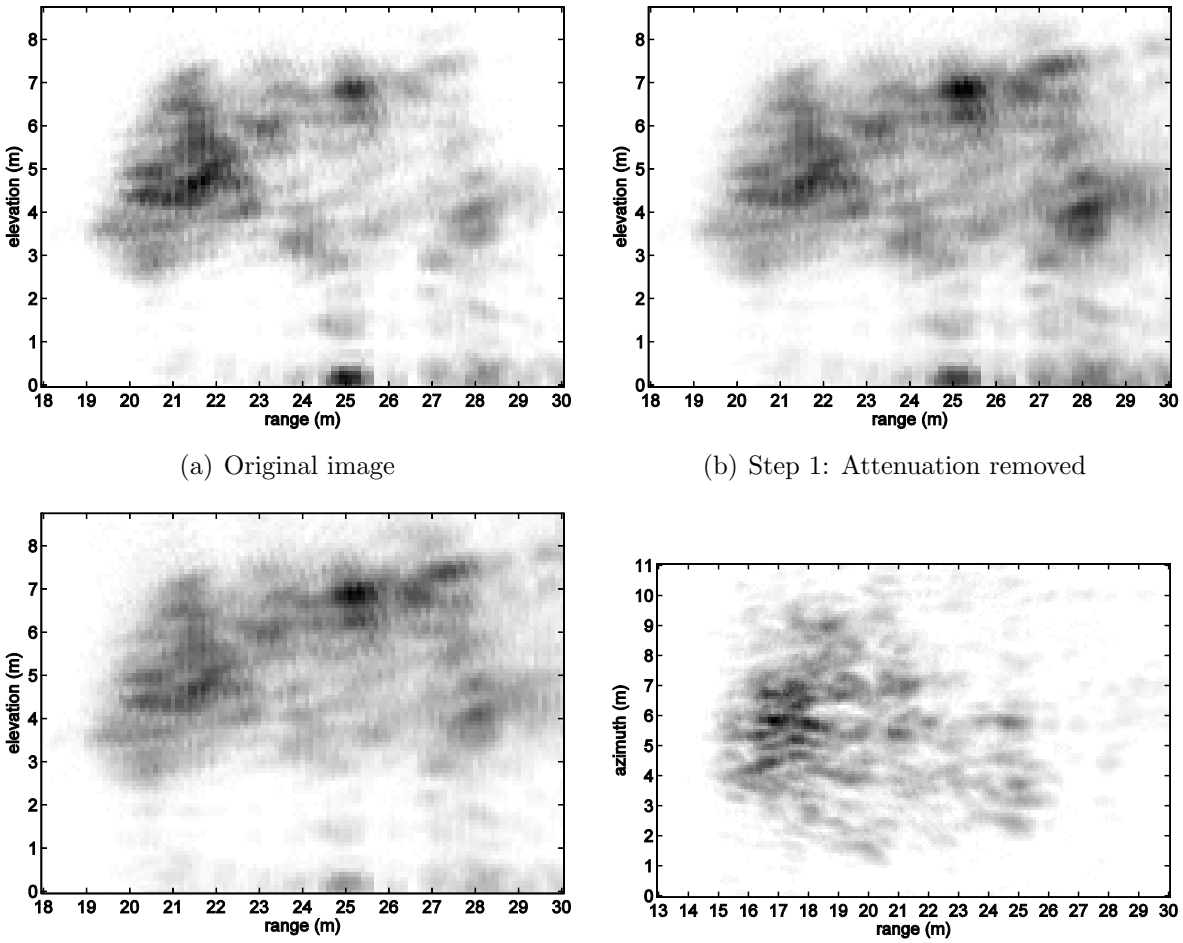

(a) Original image

(b) Step 1: Attenuation removed

(c) Step 2: Attenuation restored

(d) Step 3: Projected to 2D

Figure 6.11: Imagery representing the various stages in the airborne computation

The 3D to 2D projection is accomplished by summing the image data along similar range measurements, thus reducing the image to range and azimuth. To visualize the range measurements, imagine diagonal lines passing through the image perpendicular to the incidence angle.

Fig. 6.11(d) is the result of this step. Notice the axes have changed and are now range versus azimuth. Because of the projection, many of the features are embedded together and much of the 3D information is lost. For instance, the trunk's location is no longer apparent.

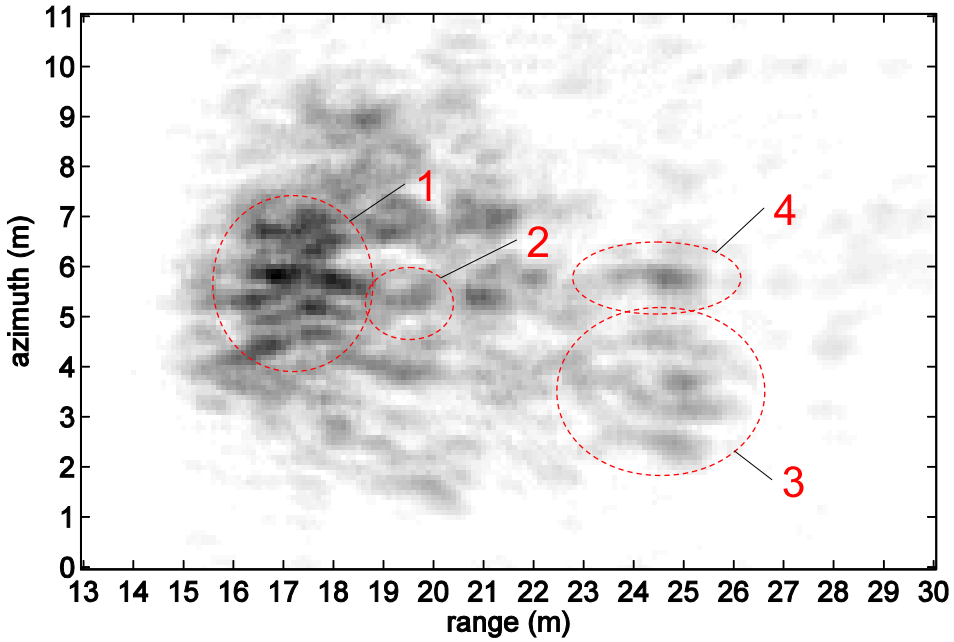

(a) 2D computed image

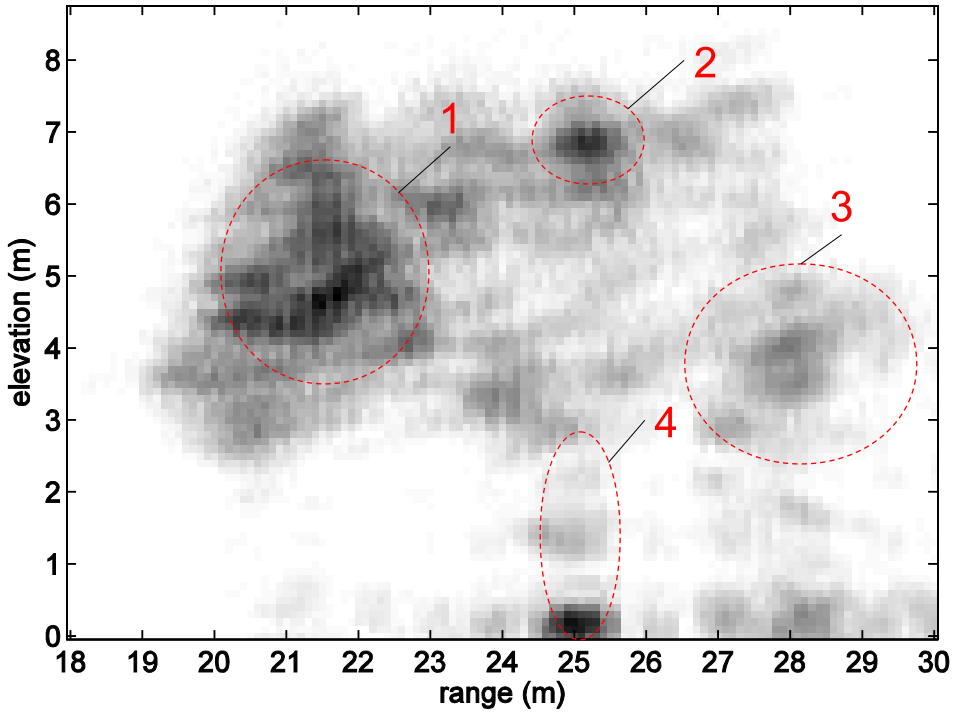

(b) 3D original image

Figure 6.12: Traceability for the computed airborne image. Four common features are identified in the 2D computed image and the 3D original image.

6.4.2 Decomposition and Traceability

Before moving onto the comparison of the transformed 3D image and a conventional 2D-SAR image, let us be sure that we understand the composition of this image. Figure 6.12 is used to assist with this. In this figure, four common features are identified in the original and computed images.

Feature 1 is the bright area within the front foliage. The front foliage is normally bright because of its positioning, but this particular area seems to have a higher density. This feature remains near the front of the reflection in the airborne image.

Feature 2 is a bright point-like reflection further back in the tree. This feature is entirely lost in the transformed image because it is combined with several meters of foliage. This is a good example of the ambiguity that is inherent in airborne imagery when attempting to image 3D features.

Feature 3 is the rear low-hanging clump of foliage which is very bright for how far back into the tree it is. Earlier it was suggested that this brightness is attributed to the radar perspective (the radar can see it by looking up from underneath the foliage) in which case the attenuation algorithms would compensate for the brightness. While this area remains somewhat pronounced, it has dimmed slightly.

Feature 4 is the trunk. Trunks are often difficult to observe using airborne SAR since they are obstructed by the overhead foliage. Observing a trunk requires a low frequency to penetrate deeply into the foliage. Even if the signal reaches the trunk, the trunk image is often embedded within the foliage, which makes it difficult to identify. In Fig. 6.12(a), the trunk is barely visible. Also, it is found in the farthest range measurement, though this is not always the case. A trunk's placement depends on tree geometry, incidence angle, and penetration depth.

6.4.3 Comparison to Real Airborne Imagery

To show the resemblance between the computed image and real airborne imagery, some examples of real airborne imagery are provided in Fig. 6.13. Figure 6.13(b) and Fig. 6.13(c) contain images from Willard Bay, Utah using the μASAR (the same module used in the 3D ground-based system). During data collection, the airplane flew at an al-

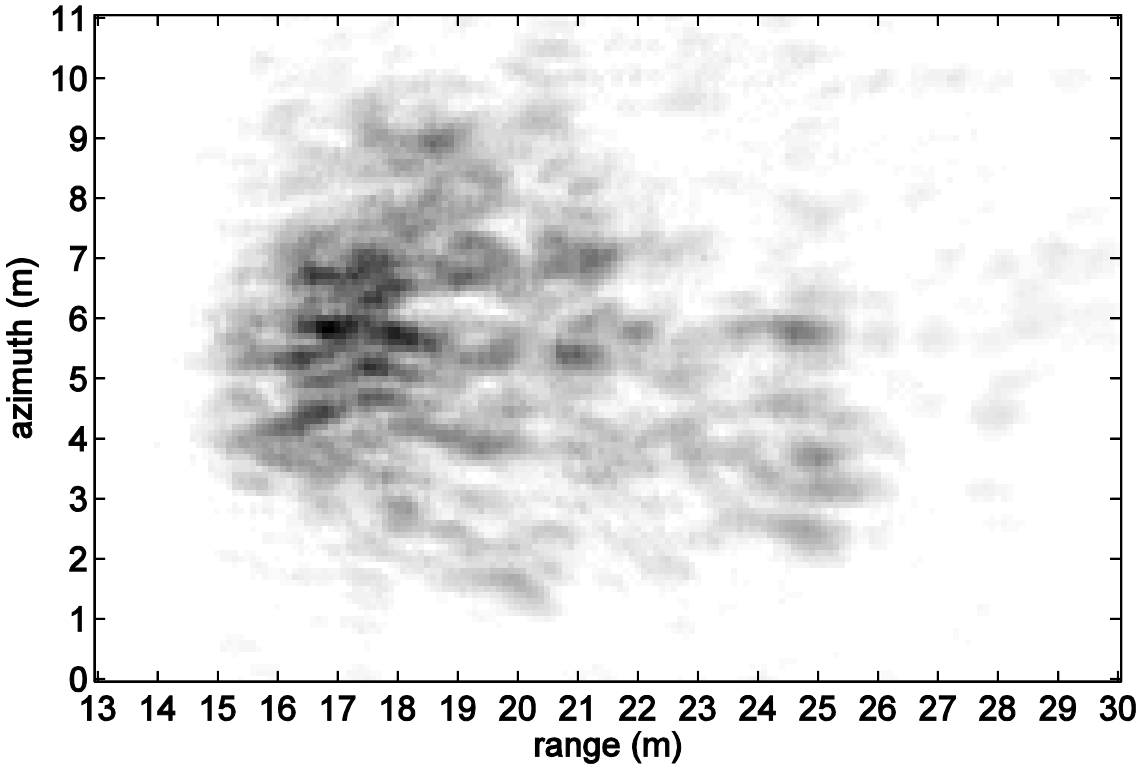

(a) Computed tree

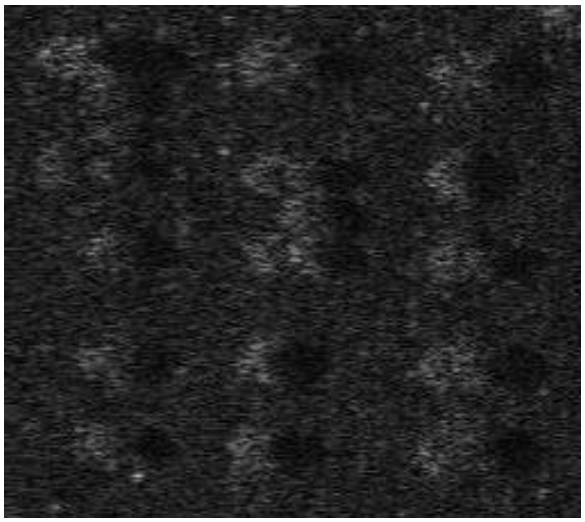

(b) Fifteen trees in C-band

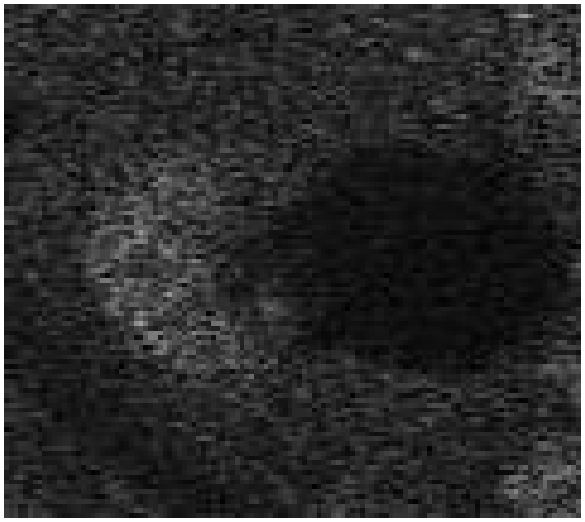

(c) Single tree close up in X-band

Figure 6.13: Comparison between the computed image and real airborne imagery acquired from Willard Bay, Utah

titude of about 1000 m with an incidence angle of approximately 50° using a 200 MHz bandwidth. Figure 6.13(b) contains a field of 15 or so trees and is imaged in C-band, the same as the 3D system. The calculated resolution of the airborne system is 1.2 m in cross-track and 0.25 m in along-track or azimuth. Figure 6.13(c) contains a single tree generated using X-band. This image is included because it is higher resolution and easier to analyze, but keep in mind that the frequency change may affect the scattering response to a degree; for instance, the penetration depth is less. Finally, Fig. 6.13(a) contains the computed image pulled from Fig. 6.11(d).

In an ideal situation, the airborne imaged tree and the ground imaged tree are the same physical tree as that would allow for a more rigorous comparison. It is also helpful if the observed trees share a similar species, shape, and size. However, in this comparison, none of these are the case.

One similarity between the computed image and the airborne images is the behavior of the layover effect. The layover effect causes the parts of the tree with the nearest range measurement to be placed farthest to the left and to often experience the least amount of attenuation. On the other hand, the parts of the tree with the farthest range measurements are placed farthest to the right and often experience the most attenuation. This behavior is what causes the tree image to be strong on the left and weak on the right. However, the signal peak is normally not on the very left-most edge of the overall reflection, but is slightly toward the center. This is due to range cross-sections being smaller at the edge of the tree.

One difference is the computed tree is longer in range than many of the airborne-SAR-generated trees. A reason a tree may appear longer is if the depth of signal penetration is greater. If this is the case, it suggests that the foliage from the honeylocust tree is less dense than these trees at Willard Bay. Not all of the airborne trees are narrow, however. Take for instance the top middle tree, which demonstrates exceptional resemblance to the computed tree. This particular tree is similar in shape, attenuation pattern, and appears to contain a trunk at a similar location.

Another difference is the lack of a shadow. A shadow is created by the contrast between the ground that is visible and the ground that is obstructed by the tree. The computed image does not contain a shadow because the ground was never visible from the

beginning due to the shallow incidence angle. However, the shadow location is predictable: based on the geometry of the tree and the incidence angle of 50°, it would extend from approximately 26 to 35 m.

Overall, there is a strong resemblance between the computed image and real airborne images. The computed tree is longer than many of the airborne trees, but this difference seems to be attributed to a difference in foliage density. A recommendation for future work is to perform both imaging technologies on a common tree so that discrepancies in tree physical attributes can be disregarded and the comparison can be more rigorous.

6.5 Chapter Summary

In this section, the 3D SAR imagery was analyzed. With the exception of one experiment, 3D reconstruction was very effective. For example, the imaged trees showed good resemblance to the physical trees, they had adequate separation from background noise and interference, the foliage was true to shape—to the point where subtle contours in the perimeter foliage were observable—effects of attenuation were evident, and they demonstrated good depth of penetration.

The image representations of the leaves, branches, and trunks were observed. The leaves were too small to be resolved individually, but the overall foliage was represented well. Measurements revealed that the radar tended to underestimate the physical dimensions only slightly and with small variance. The branches were also too small to be resolved, but in some instances, they appeared to generate specular returns resulting from favorable geometries. The trunks *were* resolved and consisted of a bright base and a dimmer, slightly distorted midsection. The bright base was a result of corner reflection and the midsection was a combination of specular surface reflections and multi-path reflections.

A repeatability study was conducted by comparing the results for the second and third experiments which imaged the same tree from different azimuth angles. The purpose of this study was to demonstrate the system's reliability and to understand a dependency on azimuth incidence angle. Unfortunately, there were too many distortions incorporated in tree 3 for this study to be effective. For better results, experiments should be performed with at least 20 m of range.

Attenuation for the leaves and branches was studied using the 3D image data and some approximations. Opposed to traditional attenuation measurements, which assume a generalized attenuation rate, this data was calculated empirically on a per voxel basis and is more appropriate for trees, since a tree has unpredictable variances in density. This data can be used to generate values for σ_v if a calibrated radar is used.

Finally, data for one of these 3D tree images was used to compute an airborne-SAR-generated 2D tree image. The computed image showed strong resemblance to real airborne imagery. This study allowed for a deeper analysis of an airborne image including decomposing it into its 3D components.

Chapter 7

Conclusion

The high-resolution ground-based 3D SAR system presented in this thesis appears to be a powerful tool for studying microwave-vegetation interactions and provides several distinct improvements over traditional 2D SAR. 2D SAR systems are unable to discriminate depth and a single resolution cell is an integration in depth of various parts of the tree including near foliage, far foliage, tree structure, and underlying soil. On the other hand, the 3D system discriminates between layers in the vegetation at various depths where a single resolution cell is a 3D voxel so that individual inclusions (down to the branch level) are studied independently. The added resolution capabilities of this system enable more precise backscatter measurements and improved model validation.

Much of the observed scattering behavior from the vegetation inclusions is consistent with current vegetation models (as presented in Chapter 3). For trunks, corner reflections from the trunk-ground intersection provide the strongest contribution. The specular returns from the trunk midsection are relatively weak even though it is normal facing to the radar. These reflections are expected to be stronger for larger trunks due to a greater target-to-wavelength ratio and a flatter incident surface.

For branches, backscatter is small and is only significant in a few instances where geometry is favorable. Small branches blend in with the foliage and are not visible while medium-to-large branches are visible only at locations where geometry is favorable. Very large branches are not observed in these experiments (since only small trees were scanned) but are expected to exhibit similar characteristics to a trunk if the branch is normal facing. It would be of interest to image large branches and view them from a variety of incidence angles.

For leaves, backscatter is characterized by the group return which is described by volume scattering. Due to their large number and varied orientation, the leaves provide a strong, reliable return which appears to be independent of incidence angle. Local variations in backscatter strength indicate variations in density. The SAR system provides a 3D density map from which density and attenuation can be derived. Traditional attenuation measurement techniques assume uniform density [25] for the depth of the measurement; however a knowledge of the 3D density distribution enables more accurate measurements. Because radar calibration is not performed, attenuation calculations rely on a series of approximations.

An experimental airborne-SAR computation is performed where the 3D image data is converted to 2D-airborne-SAR image data. This reveals a high correlation between the backscattering behavior observed by the ground-based-SAR system and that of an airborne-SAR system. Because of this correlation, we have an additional means of studying airborne imagery. Given a 3D image as a reference, an airborne tree image can be reversed-engineered so that its composition can be better studied.

7.1 Future Work

Due to the preliminary nature of the current work, only a minimal number of experiments have been performed and there remains much research to be done. Future experiments should provide for more diversity in the areas of tree selection and radar parameter selection. Regarding tree selection, experiments should include trees which are of different species and possess different geometric properties. Also, trees should be imaged during different seasons to observe the effects of water content and foliage occupancy. Experiments should include a variety of microwave frequencies, incidence angles, and polarizations. Changes in microwave frequency affect the scattering behavior of vegetation in many ways including the visibility of the leaves, branches, and trunks and the attenuation behavior of the foliage. Changes in incidence angle affect the scattering behavior of the fixed orientation features, especially the trunk. The current work attempted to observe a change in azimuth incidence angle but there were too many distortions found in tree 3 for the study to be effective. A study on the

effects of changes in elevation incidence angle would also be interesting and would provide useful insight into tree scattering behavior.

While the resolution of the current system is considered exceptional by current standards, it only provides for resolvability on some inclusions. With improved resolution, a system could achieve resolution on medium and small sized branches as well as provide more detail to the trunk and foliage mass. Resolution can be improved by one of two ways: increasing transmit frequency or increasing scanning aperture size. Since frequency is tied to attenuation behavior and affects tree visibility, the choice of frequency may be limited. In that case, the size of the scanning aperture may need to be increased. Considering that the current scanning system is relatively large and difficult transport, increasing the scanning aperture may require some creativity. For example, the system may be stationary or require on-site assembly. Another alternative is to integrate data sets which are acquired from multiple observation angles using an *irregular sampling* algorithm.

Performing radar calibration would enable direct calculation for figures such as backscattering cross-section σ_v, extinction coefficient κ_e, and attenuation rate L. These figures are necessary for validation of current vegetation scattering models. To assist in the calculation of these figures, physical measurements of the test trees should be taken including: leaf, branch, and trunk size; leaf, branch, trunk, and soil water content (or permittivity); leaf and branch orientation; and leaf and branch density.

Further analysis should be performed on the correlation between 3D ground-based-SAR imagery and airborne-SAR imagery (as explored in Section 6.4).

Bibliography

[1] S. Saatchi, J. Soares, and D. Alves, "Mapping Deforestation and Land use in Amazon Rainforest by using SIR-C Imagery," *Remote Sensing of Environment*, vol. 59, no. 2, pp. 191–202, 1997. 1

[2] E. Rignot, W. Salas, and D. Skole, "Mapping Deforestation and Secondary Growth in Rondonia, Brazil, using Imaging Radar and Thematic Mapper Data," *Remote Sensing of Environment*, vol. 59, no. 2, pp. 167–179, 1997. 1

[3] M. Zribi, L. Hegarat-Mascle, O. Taconet, D. Vidal-Madjar, M. Boussema, and Z. Belhadj, "Estimation of Spatial and Temporal Evolution of Vegetation and Surface Moisture from ERS2 Radar in a Semi-Arid Region," in *Geoscience and Remote Sensing Symposium, 2001. IGARSS'01. IEEE 2001 International*, vol. 5. IEEE, 2001, pp. 2109–2111. 1

[4] I. Woodhouse, J. van der Sanden, and D. Hoekman, "Scatterometer Observations of Seasonal Backscatter Variation over Tropical Rain Forest," *Geoscience and Remote Sensing, IEEE Transactions on*, vol. 37, no. 2, pp. 859–861, 1999. 1

[5] M. Imhoff, A. Milne, T. Sisk, W. Lawrence, and K. Brennan, "Mapping Vegetation Structure for Biodiversity Analysis using Synthetic Aperture Radar," in *Geoscience and Remote Sensing, 1997. IGARSS'97. Remote Sensing-A Scientific Vision for Sustainable Development., 1997 IEEE International*, vol. 4. IEEE, 1997, pp. 1624–1626. 1

[6] M. Sgrenzaroli, A. Baraldi, G. De Grandi, H. Eva, and F. Achard, "A Novel Approach to the Classification of Regional-Scale Radar Mosaics for Tropical Vegetation Mapping," *Geoscience and Remote Sensing, IEEE Transactions on*, vol. 42, no. 11, pp. 2654–2669, 2004. 1

[7] L. Hess, J. Melack, S. Filoso, and Y. Wang, "Delineation of Inundated Area and Vegetation along the Amazon Floodplain with the SIR-C Synthetic Aperture Radar," *Geoscience and Remote Sensing, IEEE Transactions on*, vol. 33, no. 4, pp. 896–904, 1995. 1

[8] T. Le Toan, A. Beaudoin, J. Riom, and D. Guyon, "Relating Forest Biomass to SAR Data," *Geoscience and Remote Sensing, IEEE Transactions on*, vol. 30, no. 2, pp. 403–411, 1992. 1

[9] D. Lu, "The Potential and Challenge of Remote Sensing-Based Biomass Estimation," *International Journal of Remote Sensing*, vol. 27, no. 7, p. 1297, 2006. 1

[10] T. Jackson, D. Chen, M. Cosh, F. Li, M. Anderson, C. Walthall, P. Doriaswamy, and E. Hunt, "Vegetation Water Content Mapping using Landsat Data Derived Normalized Difference Water Index for Corn and Soybeans," *Remote Sensing of Environment*, vol. 92, no. 4, pp. 475–482, 2004. 1

[11] M. Karam, A. Fung, R. Lang, and N. Chauhan, "A Microwave Scattering Model for Layered Vegetation," *Geoscience and Remote Sensing, IEEE Transactions on*, vol. 30, no. 4, pp. 767–784, 1992. 1, 2, 30

[12] F. Ulaby, "Radar Response to Vegetation," *Antennas and Propagation, IEEE Transactions on*, vol. 23, no. 1, pp. 36–45, 1975. 1

[13] M. Imhoff, M. Story, C. Vermillion, F. Khan, and F. Polcyn, "Forest Canopy Characterization and Vegetation Penetration Assessment with Space-borne Radar," *Geoscience and Remote Sensing, IEEE Transactions on*, no. 4, pp. 535–542, 1986. 1

[14] J. Lopez-Sanchez, J. Fortuny-Guasch, S. Cloude, and A. Sieber, "Indoor Polarimetric Radar Measurements on Vegetation Samples at L, S, C and X band," *Journal of electromagnetic waves and applications*, vol. 14, no. 2, pp. 205–231, 2000. 1, 3

[15] E. Attema and F. Ulaby, "Vegetation Modeled as a Water Cloud," *Radio Science*, vol. 13, no. 2, pp. 357–364, 1978. 2, 27

[16] J. Way, J. Paris, M. Dobson, K. McDonals, F. Ulaby, J. Weber, L. Ustin, V. Vanderbilt, and E. Kasischke, "Diurnal Change in Trees as Observed by Optical and Microwave Sensors: the EOS Synergism Study," *Geoscience and Remote Sensing, IEEE Transactions on*, vol. 29, no. 6, pp. 807–821, 1991. 2

[17] M. Karam, A. Fung, and Y. Antar, "Electromagnetic Wave Scattering from Some Vegetation Samples," *Geoscience and Remote Sensing, IEEE Transactions on*, vol. 26, no. 6, pp. 799–808, Nov 1988. 3, 30

[18] L. Allan and G. McCormick, "Measurements of the Backscatter Matrix of Dielectric Bodies," *Antennas and Propagation, IEEE Transactions on*, vol. 28, no. 2, pp. 166–169, 1980. 3

[19] S. J. Preston, "Design and Feasibility Testing for a Ground-based, Three-dimensional, Ultra-high-resolution, Synthetic Aperture Radar to Image Snowpacks," Master's thesis, Brigham Young University, Provo, UT, August 2010. 3, 39, 41

[20] M. A. Richards, *Fundamentals of Radar Signal Processing.* New York: McGraw-Hill, 2005. 8, 17

[21] E. Zaugg and D. Long, "Generalized Frequency-Domain SAR Processing," *Geoscience and Remote Sensing, IEEE Transactions on*, vol. 47, no. 11, pp. 3761 –3773, Nov. 2009. 15

[22] K. Eldhuset, "Ultra High Resolution Spaceborne SAR processing," *Aerospace and Electronic Systems, IEEE Transactions on*, vol. 40, no. 1, pp. 370–378, 2004. 17

[23] F. Ulaby, R. Moore, and A. Fung, *Microwave Remote Sensing: Active and Passive. Volume 1-Microwave Remote Sensing Fundamentals and Radiometry.* Norwood, MA: Artech House Inc., 1981. 24, 25

[24] ——, *Microwave Remote Sensing: Active and Passive. Volume 2-Radar Remote Sensing and Surface Scattering and Emission Theory.* Norwood, MA: Artech House Inc., 1982. 27

[25] P. Johannesson, "Wave Propagation Through Vegetation at 3.1 GHz and 5.8 GHz." 30, 31, 90

[26] Y.-C. Lin and K. Sarabandi, "Electromagnetic Scattering Model for a Tree Trunk above a Tilted Ground Plane," *Geoscience and Remote Sensing, IEEE Transactions on*, vol. 33, no. 4, pp. 1063 –1070, Jul 1995. 30

[27] C. Matzler and A. Sums, "Microwave Radiometry of Leaves," in *Microwave Radiometry and Remote Sensing Applications: Proceedings of the Specialist meeting held in Florence, Italy, 9-11 March, 1988*, vol. 1988. VSP, 1989, p. 133. 31

[28] W. Carrara, R. Goodman, and R. Majewski, "Spotlight Synthetic Aperture Radar-Signal processing algorithms(Book)," *Norwood, MA: Artech House, 1995.*, 1995. 39

[29] Agilent, "Planar Near-field Scanners," http://http://contact.tm.agilent.com/data/static/eng/tmo/catalogs/vxichanpart/prodpages/plannfs.html, 2000. 40

[30] U. of London, "NSI Planar Near-Field Antenna Measurement Scanner," http://www.elec.qmul.ac.uk/antennas/facilities/NSIScanner.html, 2008. 40

[31] A. Yaghjian, "An Overview of Near-Field Antenna Measurements," *Antennas and Propagation, IEEE Transactions on*, vol. 34, no. 1, pp. 30–45, 1986. 40

[32] V. Liepa, K. Sarabandi, and M. Tassoudji, "A Pulsed Network Analyzer Based Scatterometer," vol. 3, 1989, pp. 1826–1828. 41

[33] M. Sato, Z. Zhou, T. Hamasaki, and W. Boerner, "Development of a Ground-Based Synthetic Aperture Radar (GB-SAR) System and its Applications to Environment Monitoring and Disaster Prevention," in *ESA Special Publication*, vol. 586, 2005, p. 20. 41

[34] Z. Zhou and S. Cloude, "The Development of a Ground Based Polarimetric SAR Interferometer (GB-POLInSAR)," in *Geoscience and Remote Sensing Symposium, 2005. IGARSS'05. Proceedings. 2005 IEEE International*, vol. 2. IEEE, 2005, pp. 1097–1100. 41

[35] A. Martinez-Vazquez, J. Fortuny-Guasch, and U. Gruber, "Monitoring of the Snow Cover with a Ground-Based Synthetic Aperture Radar," *EARSeL eProceedings*, vol. 4, no. 2, pp. 171–178, 2005. 41

[36] D. Tarchi, N. Casagli, R. Fanti, D. Leva, G. Luzi, A. Pasuto, M. Pieraccini, and S. Silvano, "Landslide Monitoring by using Ground-Based SAR Interferometry: An Example of Application to the Tessina Landslide in Italy," *Engineering Geology*, vol. 68, no. 1-2, pp. 15–30, 2003. 41

[37] M. Edwards, D. Madsen, C. Stringham, A. Margulis, B. Wicks, and D. Long, "microASAR: A Small, Robust LFM-CW SAR for Operation on UAVs and Small Aircraft," in *Geoscience and Remote Sensing Symposium, 2008. IGARSS 2008. IEEE International*, vol. 5, July 2008, pp. V –514 –V –517. 98, 119

[38] M. C. Edwards, "Design of a Continuous-Wave Synthetic Aperture Radar System with Analog Dechirp," Master's thesis, Brigham Young University, Provo, UT, August 2009. 98, 119

[39] A. M. Products, "Product Manuals by Type," http://www.applied-motion.com/support/manuals, 2010. 119

Appendix A

Scanner Component Descriptions

This appendix provides detailed descriptions of the individual components of the ground-based SAR system. These descriptions include information such as manufacturer name, part numbers, dimensions, and specifications. Descriptions are given to the components enumerated in Section 4.3 as well as the limit switches, cabling, communication protocol.

A.1 MicroASAR

The μASAR is a flexible, robust SAR system developed by Artemis Inc. in cooperation with BYU students. It is a LFM-CW (linear frequency modulated continuous wave) system designed for low-power operation. It is completely contained in one compact aluminum enclosure measuring 22.1 x 18.5 x 4.6 cm and weighs less than 3.3 kilograms. An enclosed digital subsystem generates the LFM chirp, writes received data to a Compact Flash card, and performs rudimentary pre-storage processing such as pre-summing and LFM de-chirping.

A second card slot records communications from an RS-232 input (this input is used by the ground-based system's software for sending position data). Any recognizable packets received on this input are time-stamped and written out to the card. These packets are batch written, meaning that they are held in internal memory until 10 kilobytes have accumulated. Because of this, it is good practice to send an additional 10 kilobytes of empty data before turning off the module to ensure that all relevant packets have been written out to the card.

Table A.1: MicroASAR System Specifications

Modulation Type	LFM-CW
Operating Frequency Band	C-band
Transmit Center Frequency	5428.76 MHz
Signal Bandwidth	80-160 MHz (variable)
PRF	7-14 kHz (variable)
Transmit Power	30 dBm
Supply Power	<35 W
Supply Voltage	+15 to +26 VDC
Dimensions	22.1 x 18.5 x 4.6 cm
Weight	3.3 kg

Additional information on the μASAR can be found here [37, 38].

A.2 Antenna Mount

The antenna mount (shown in Fig. A.1) supports two antennas as well as a small radar module. It has a mounting face of 1.2 ft^2 and has been tested to support loads up to 10 lbs. Screw holes for the antennas are located in the top corners and allow for horizontal or vertical attachment enabling four polarimetric configurations: HH, VV, HV, and VH. The radar module mounts below the antennas.

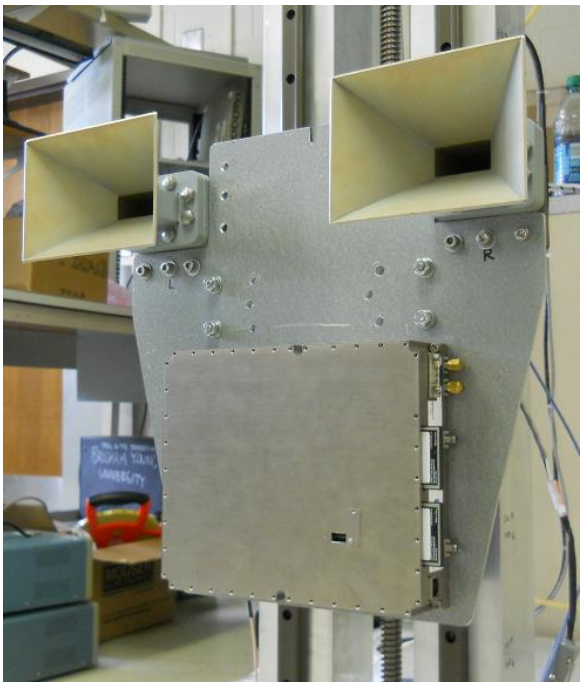

Figure A.1: Photo of the scanner's antenna mount with the antennas and μASAR mounted

A.3 Horn Antennas

The horn antennas (make and model: Waveline, 5999) have physical apertures of 9.8 cm x 13.2 cm and a frequency range of 4.90 to 7.05 GHz, which accommodates the μASAR's center frequency of 5.4 GHz. Their 3 dB beam widths in both planes are approximately 30 degrees, giving them effective apertures of approximately 10 cm x 10 cm. Figure A.2 provides a diagram of a horn antenna.

A.4 Stepper Motors

Stepper motors use toothed electromagnets, controlled by a microcontroller, to divide a full rotation into a large number of steps. As shown in Fig. A.3, a set of electromagnets

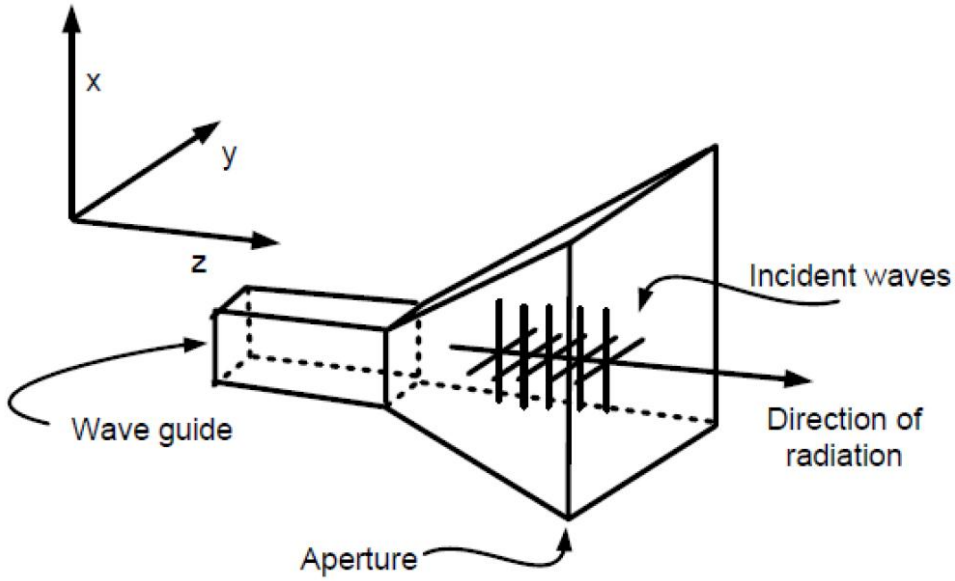

Figure A.2: Diagram of a horn antenna

encircle a gear shaped rotor. When a magnet is energized, the rotor's teeth are lined up to the nearest teeth on the magnet. By energizing the magnets consecutively and one at a time, the rotor is turned incrementally in one direction. Each increment is referred to as a step and is equal to the radial length of one tooth divided by the number of magnets. One criticism of stepper motors is that torque rapidly decreases when velocity increases.

These particular stepper motors (make and model: Applied Motion Products, STM23S-3RE) feature a drive and motor integrated into one compact unit (Fig. A.4). They have an electronic gearing feature which permits a range of step sizes: 200 to 51200 steps per revolution. The current setting for this parameter is 4000, which matches the optical encoder.

The motors contain an optical encoder which provides resolution of 4000 counts per revolution (same as step resolution). The encoder position is available upon request. Used in conjunction with the acme lead screws, which have five threads per inch, the encoder resolution translates into a linear resolution of 1.27 μm per revolution.

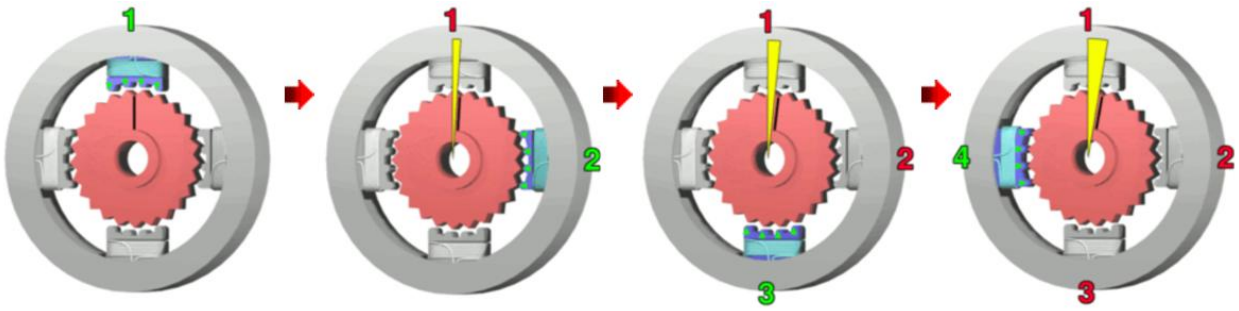

Figure A.3: Progression of one stepper motor cycle. See text for discussion.

Figure A.4: STM23S-3RE stepper motor

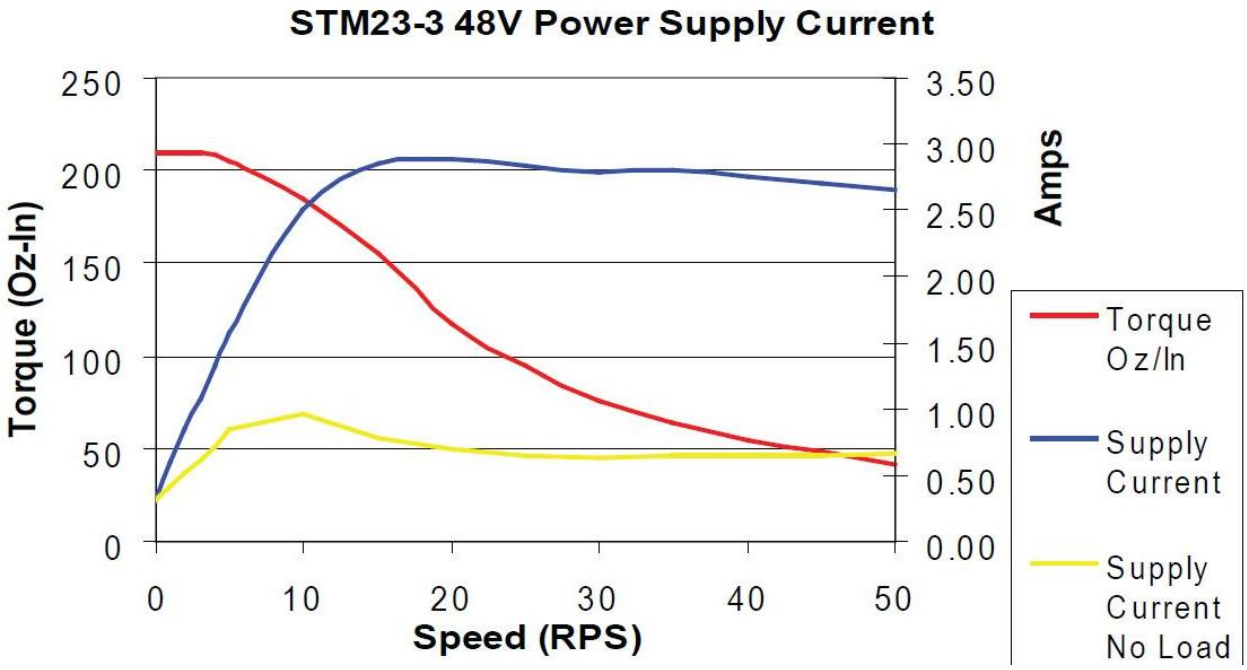

Figure A.5: Torque and amperage versus velocity for the stepper motors

The motors operate on 12 to 70 VDC and provide up to 210 oz-in of torque. The amount of available torque is dependent on the input voltage and velocity of the motor. Fig. A.5 shows torque as a function of velocity for an input voltage of 48 volts. From 0 to 4 rps the torque remains at approximately 210 oz-in, but past there the torque begins to decrease, becoming half at about 22 rps.

The motors accept analog and digital signals as well as RS-485 serial commands. Serial commands are used by the scanner software to instruct the drives. The analog inputs are used to monitor the status of the limit switches where a change of status immediately disables the motor's motion in the given direction.

A.5 Acme Lead Screws

The acme lead screws (make and part number: Thomson BSA, M23S12-XCT7505-72") are used to translate the radial motion of the motors to translational motion. These screws are made of stainless steel, are 6 ft long, have a major diameter of .75 inches, a minor diameter of 0.53 inches, a thread distance of 0.2 inches, and an accuracy up to 0.003 in/ft. The accompanying nuts have an anti-backlash technology to prevent slipping when motion is halted, which is especially useful when motion is opposing gravity. An image of the screw and nut is given in Fig. A.6(a).

The acme thread form (illustrated in Fig. A.6(b)) compares with forms such as square, V, and buttress. Square threads are the most efficient, but the most difficult to machine, and are therefore the most expensive. Acme threads closely resemble square threads but are less expensive.

A.6 Limit Switches

Four limit switches protect the boundaries of the two axes and define the extent of the scan area. The switches are wired into the motors' analog inputs in a *normally closed* configuration. When a limit is hit, the circuit opens, causing motion in the given direction to halt; motion in the opposing direction, however, remains unaffected. The motors' limit switch settings are accessed with the "DL" command. A single limit switch is shown in Fig. A.7.

A.7 Cabling

Cabling includes data and power lines to the motors and radar. All data lines use CAT5E cabling. CAT5E is known for high signal integrity and is commonly used for data transmission. The motors share the same data line and as a result, all communications between the motors and the host must be addressed. The radar has a dedicated data line.

Power lines use shielded, 18 gauge wire. Shielding reduces noise by preventing cross-talk between parallel wires. Eighteen gauge wire has a current rating of 2.3 amps. The μASAR draws between 1 and 2 amps of current and has a dedicated power line. Each motor is capable of drawing 3 amps of current (though they rarely draw near that amount). Since they share the same circuit, driving both motors simultaneously exceeds the cable's current rating and is not recommended.

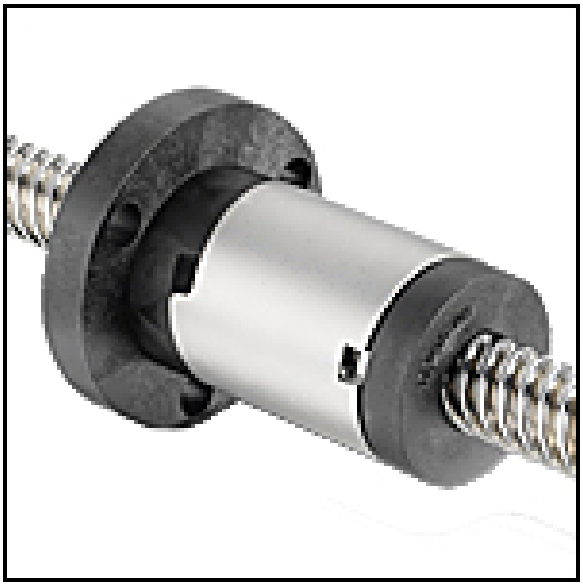

(a)

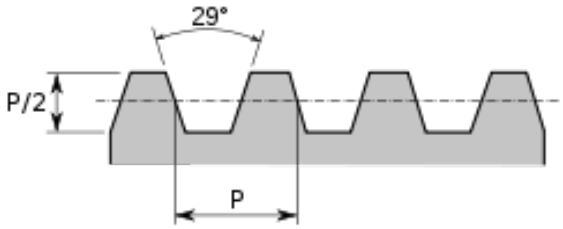

(b)

Figure A.6: (a) Acme lead screw and nut (make and part number: Thomson BSA, M23S12-XCT7505-72) and (b) acme thread form

All lines use stranded opposed to solid conductor wire, providing more durability for repeated flexing.

The platform's pluggable interface is shown in Fig. A.8. The two power inputs are on the left; the one for the radar is marked red and the one for the motors is marked green. The data inputs for the radar and motors are RS232 and USB-B respectively. The USB-B input is immediately converted to RS-485 to accommodate the motor inputs.

A.8 Communication Protocol

The stepper drives accommodate various serial protocols. The current settings are:

- Baud rate: 9800 baud
- Data word: 1 start bit; 8 data bits; 1 stop bit; 0 parity bits

Communication with the stepper drives is two-way. The drives receive *SCL command packets* and reply with SCL response packets. All SCL packets are strings prefixed with a drive address and terminated with a carriage return character.

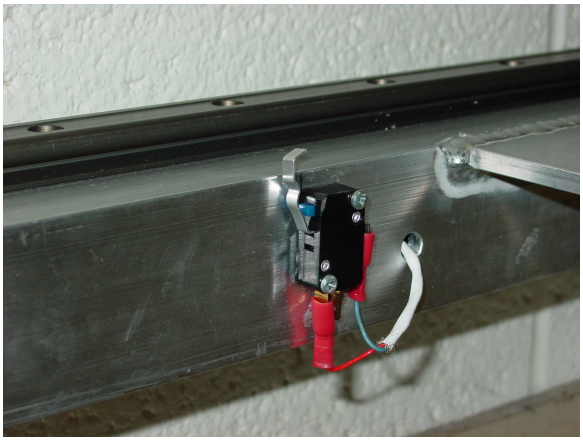

Figure A.7: Photo of one of four limits switches; mounted at left end of the scanners horizontal base

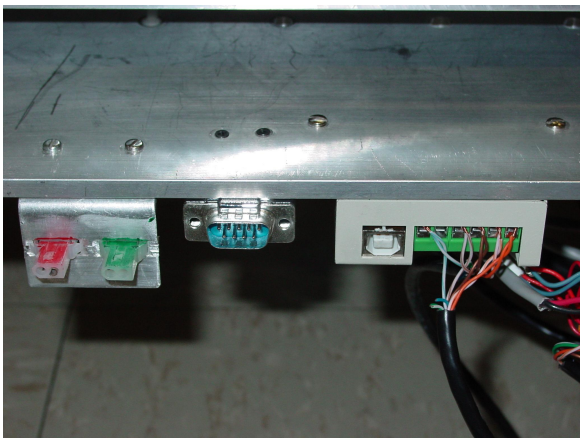

Figure A.8: Photo of the scanners pluggable cable interface. From left to right: radar power (red), motor power (green), radar data (RS232), motor data (USB-B).

SCL command strings consist of a two letter command name immediately followed by a parameter. Each time a character is received by the drive, an internal timer is reset to 200 ms. If this timer times out before the current command is terminated with a carriage return, the command times out.

SCL response strings are one of three types: acknowledgments to accepted commands, responses to data requests, and errors. More information about the communication protocol or about the SCL language can be found in the Applied Motion manuals (see Appendix C).

A.9 System Controller Software

The operation of the ground-based system is controlled by a software controller. The responsibilities of this controller include: programming the stepper motors, sending movement commands, tracking the relative position of the scanner, relaying position data to

the radar unit, and constructing and executing large scale movement patterns. Essentially, this program acts as a position controller for the scanner with a few additional housekeeping responsibilities.

The controller runs on a PC host computer and communicates with the scanner components via serial connections. The controller provides a graphical user interface (GUI) which is easy to use and provides all of the necessary controls to operate and troubleshoot the scanner.

Before a scan can be run, the following preparatory steps are required:

1. Serial connection made between the host computer and motors.
2. Serial connection made between the host computer and radar.
3. 20-70 VDC supplied to the motors.
4. 28 VDC supplied to the radar.
5. Scan parameters selected.

If a user attempts to run a scan when one of these steps are not completed, with the exception of 4 and sometimes 2, the software will prevent a scan from starting and generate an error message. The reason why steps 2 and 4 are not always detected is because communication with the μASAR is only one way. As a result, it is imperative to manually verify these connections prior to each scan.

See Appendix B for more information about the software including a walk-through of the GUI.

Appendix B

Instructions for using the Scanner Control Software

The scanner's software controller is responsible for managing the scanner's position and automating full scan routines. It is written in C++ using the QtCreator SDK (software development kit) and runs on a PC host. It provides a friendly graphical user interface (GUI) which provides all of the necessary controls to operate and troubleshoot the scanner.

B.1 Getting Started

The following components are required prior to running the software:

- *GBSAR_Controller.exe* executable
- *qextserialport* library files
- Windows PC with 2 USB ports
- USB A/B cable (printer cable)
- RS-232 adapter
- RS-232 cable
- 2 power supplies units rated at 50 VDC and 3 amps

To install the software, copy the GBSAR_Controller executable file and the qextserialport library files onto your Windows machine and be sure to set the environmental PATH variable to indicate where the library files are located. The QtCreator libraries are cross-platform, but the software has only been tested on Windows.

Prior to running the software, be sure that the following connections are made to the scanner's pluggable interface:

- Power for motors: 20-70 VDC
- Power for μASAR: 28 VDC
- Data for motors: USB-B
- Data for μASAR: RS-232

Power can be supplied using two power supply units. Be sure that each unit is able to supply the required voltage and at least 3 amps of current. The data connection to the μASAR is made using a USB A/B cable (a printer cable). The data connection to the motors is made using a standard RS-232 cable and USB to RS-232 adapter.

The software prevents a scan from starting if the motors are not connected. However, since the software does not receive any communications from the μASAR, it does not prevent a scan from starting if the μASAR is not connected. As a result, it is imperative to manually verify these connections prior to each scan.

B.2 User Interface

The software's GUI can be used to set up parameterized scans, monitor scan progress, provide manual controls, and provide troubleshooting capabilities. To define some terminology, a *scan* consists of a given number of passes across a *scan area* at given increments, a *pass* consists of a given number of samples at given increments, and a *sample* consists of a pause and a data transmission.

B.2.1 *Choose Ports* Dialog

When the program is launched, the user is presented with the *Choose ports* dialog (Fig. B.2.1). Here, the user indicates which ports the motors and μASAR will use for data transmissions. The dialog only displays currently available ports, so both serial cables need to be plugged in prior to this point. Once *OK* is pressed, the main interface appears on the screen.

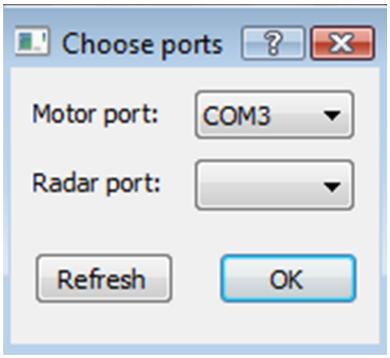

Figure B.1: *Choose Ports* dialog

B.2.2 Main Tab

The *Main* tab (Fig. B.2.2) provides an environment for the user to create, execute, and monitor scans. The tab consists of three buttons and two display boxes.

The *Create Scan* button opens the *Set up* dialog which contains the scan parameters. After the scan parameters are selected, they appear in the *Scan Parameters* display box and the *Run* button becomes enabled.

The *Run* button initiates a scan defined by the entries in the *Scan Parameters* display box. While a scan is in progress, this button is replaced by *Pause* and *Stop* buttons. The *Pause* button performs a soft stop, meaning that the scanner halts after completing the current command. Also, the scan can be resumed by pressing the button a second time. The *Stop* button performs a hard stop, meaning that the scanner halts in mid-execution of the current command and the scan is aborted.

The *Flush* button is provided to accommodate the μASAR with its storage management. It should be pressed at the completion of a scan or anytime before removing the Flash card after data has been written to it.

The *Recent Positions* display box displays the previously visited positions and can be used to monitor scan progress. Also, this box provides a means to backtrack progress or recover from interruptions (see Section B.3. To resume a scan from one of the previous positions, click on one of the position entries and confirm your action with the software. The scanner then travels to the requested position and resumes scanning.

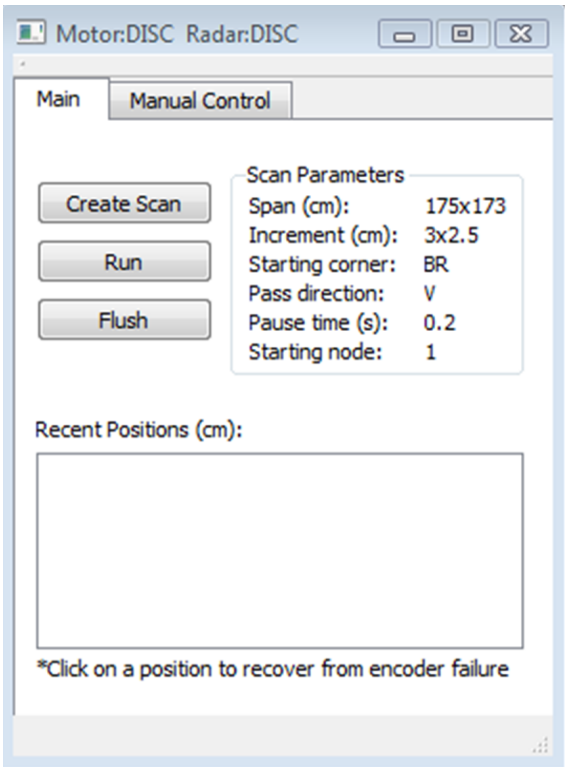

Figure B.2: *Main* tab

B.2.3 Manual Control Tab

The *Manual Control* tab (Fig. B.2.3) provides more direct control over the scanner. It consists of a directional pad, an SCL command input, and a response window.

The directional pad provides manual control of the scanner's movement and its four direction keys can be *pressed* or *clicked*. If a key is pressed, the scanner remains in motion until the key is released. If a key is clicked, the scanner remains in motion until the key is clicked a second time. Due to power considerations, simultaneous motion in two directions is prevented.

The SCL command input accepts valid SCL commands and delivers them to the motors. If a command requires a return value, it is displayed in the *Response* display box.

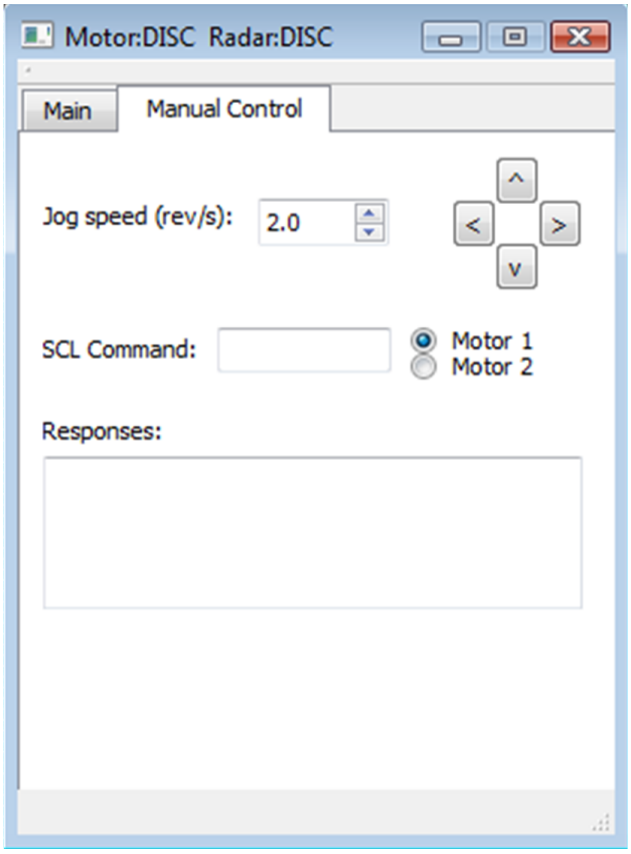

Figure B.3: *Manual Control* tab

B.2.4 Settings Dialog

The *Settings* dialog (which opens when the *Create Scan* button is pressed from the *Main* tab) shown in Fig. B.2.4 provides inputs for the scan parameters. *Span* defines the total scan area, *increment* defines the spatial sampling period, *velocity* defines the motor velocity in revolutions per second, *starting corner* defines the orientation of the scan area, *pass direction* defines the direction of the passes (or the fast axis) and *pause* defines the amount of time the scanner spends resting at each sample location (to collect backscatter). Information about the scan—such as number of passes, samples per pass, and estimated scan time—is displayed at the bottom of the dialog.

The *Continue from previous* check box provides the option of continuing from the previous scan. Be sure to select the same scan parameters and an appropriate *start node* (*start node* is the position index of the next position to be visited). Essentially, this option just prevents the encoders from being reset. Use this option in the case of a software crash.

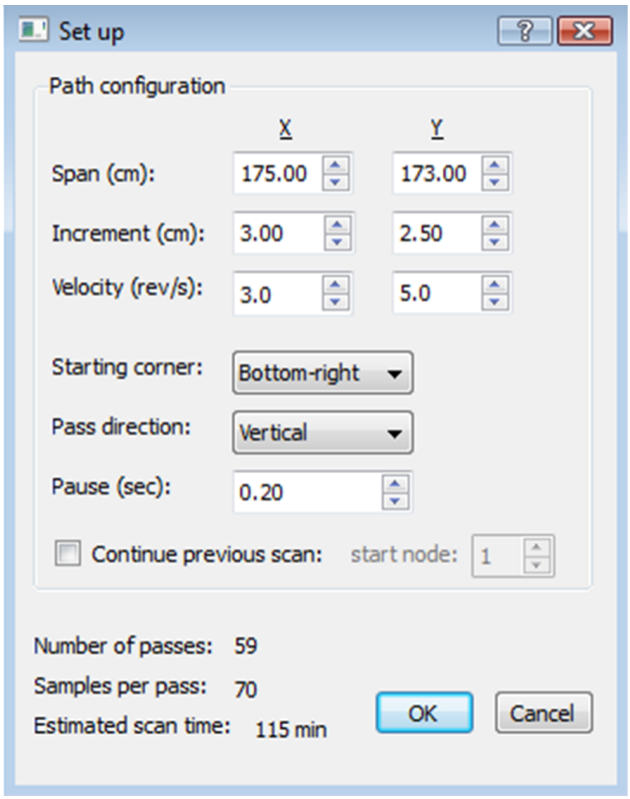

Figure B.4: *Settings* dialog

B.3 Recovery Scenarios and Procedures

Due to the length of a scan, there is ample opportunity for an interruption to occur as a result of a failure such as a power loss, a software crash, or a cable disconnection. This section provides some scenarios where the progress of a scan is interrupted and describes the steps that can be taken to recover from the interruption without having to restart the scan from the beginning.

The software is stopped

If a scan's progress is stopped (because the user pressed *Stop* or there was an error) the scan can be resumed by clicking on one of the position entries in the *Recent Positions* display box.

The software is shut down

If the software shuts down due to a crash or the laptop losing power, a scan can be resumed by reloading the software, re-entering the scan parameters, checking the *Continue from previous* check box, and selecting an appropriate *start node*. As long as the motors have remained powered, the software will recover the current position values.

The motors lose power

If the motors lose power during a scan, the software detects that they are no longer sending acknowledgments and terminates the scan. When the motors are powered back on, the software recognizes that the encoders have been reset and prompts the user to choose if they would like to set the encoders to the values held by the software. After clicking *Yes*, the scan can be resumed by clicking on any of the entries in the *Recent Positions* display box. If for some reason the software does not offer a prompt, the encoders can be set manually through the SCL command input. To obtain the correct encoder values, multiply the most recent position entry from the *Recent Positions* display box by 7,874 steps/cm.

If power loss occurs during motion then the software will not hold the correct position values. In this case, the unknown position value must be measured with the glued-on measuring tape.

The motors and software lose power

If the motors and the laptop hosting the software both lose power simultaneously, it is up to the user to determine the current position and position index. If the software was able to close normally, it will have saved a communication log to a file from which the most recent position can be obtained. Otherwise, the position can be measured with the glued-on measuring tape. Once the current position has been determined and the software has been reloaded, use the *Continue from previous* option in the *Settings* dialog.

The μASAR loses power

If the μASAR loses power during a scan, the software will not be aware and will continue to run. If it is noticed that the μASAR has lost power, pause (or stop) the scan

and extract the data from the two Flash cards. Do not turn the μASAR back on since this causes the previous data to be overwritten. After reinstalling the cards, resume the scan by pressing *Continue* or by clicking one of the position entries in the *Recent Positions* display box.

A motor slips (makes a grinding sound)

Because the motors are relatively small, it is fairly easy to overburden them with excessive friction. Common sources of friction are: misalignment of the screw blocks (usually only apparent at the extreme ends of the screw) flexing due to loose parts/screws, and warping due to cold. One other source of friction is the two-thirds point on the screw where the screw has a "fat spot". Unfortunately, the encoders sometimes do not maintain reliable values after slipping occurs.

To determine if an encoder's value has been compromised, check if the scanner is stopping at the correct intervals using the glued-on measuring tape. If the encoder seems to be off, pause (or stop) the scan, determine the correct encoder value by multiplying the measuring tape value by 7,874 steps/cm, and set the encoder to this value using the SCL command input. Then resume the scan by by pressing *Continue* or by clicking one of the position entries in the *Recent Positions* display box.

If there are known points of friction, the motor velocities can be decreased or increased on the fly. The motor have a much better chance of getting through the friction point at a lower velocity.

A data cable becomes unplugged

If one of the data cables becomes unplugged several things may happen. If the disconnection occurs in front of one of the serial adapters, the software immediately detects a port error and waits until the connection is re-established.

If the disconnection occurs at one of the motors, the software detects that they are no longer sending acknowledgments and terminates the scan. Once the connection is re-established the scan can be resumed by clicking on any of the entries in the *Recent Positions* display box.

If the disconnection occurs at the μASAR the software will not be aware and will continue to run. When it is noticed that the disconnection has occurred, pause (or stop) the scan, reconnect the cable, and resume the scan by pressing *Continue* or by clicking one of the position entries in the *Recent Positions* display box.

Appendix C

Technical Helps for Using the Scanning Platform

C.1 Troubleshooting Tips

This section provides suggestions for some common troubleshooting scenarios.

Horizontal motor is slipping on velocities lower than usual

Try these steps in order:

1. Increase the supply voltage.
2. Ensure that the center screw block is tightly fastened.
3. Test the alignment of each screw block. To do this: remove the block, run the scanner to the very end of the screw, then reinstall the block. Insert spacers if necessary.
4. Remove screws from the rear rail.

Horizontal motor is slipping at approximately two-thirds down-track

This is an unavoidable issue. The cause is a manufacturing imperfection and the screw is slightly fatter at that location. The only remedies are to lower the velocity or to use the hand-crank.

Scanner is not moving and motor is making a clicking sound

Check if the coupler attached to the motor shaft has decoupled.

A motor is not responding

Check power and data connections. Check for an error code transmission in the software's history window. Check the motors' status LEDs. Reboot the software.

μASAR is not recording position data

Check power and data connections to the μASAR. Ensure that flush packets are sent.

Status LEDs indicate a limit switch trigger when no switch is pressed

The limit switch setting in the motors should be set to *normally closed*. To check this setting, type the SCL command *DL* and a value of 2 should be returned. Also, check for a disconnected wire on the limit switch.

C.2 Stepper Motor Error LEDs

The STM motors provide two (red and green) status LEDs to indicate their current status including the presence of errors. During an error the LEDs repeat the corresponding sequence of flashes.

Code	Error
solid green	no alarm, motor disabled
flashing green	no alarm, motor enabled
1 red, 1 green	motor stall (optional encoder only)
1 red, 2 green	move attempted while drive disabled
2 red, 1 green	ccw limit
2 red, 2 green	cw limit
3 red, 1 green	drive overheating
3 red, 2 green	internal voltage out of range
4 red, 1 green	power supply overvoltage
4 red, 2 green	power supply undervoltage
5 red, 1 green	over current / short circuit
6 red, 1 green	open motor winding
7 red, 1 green	serial communication error

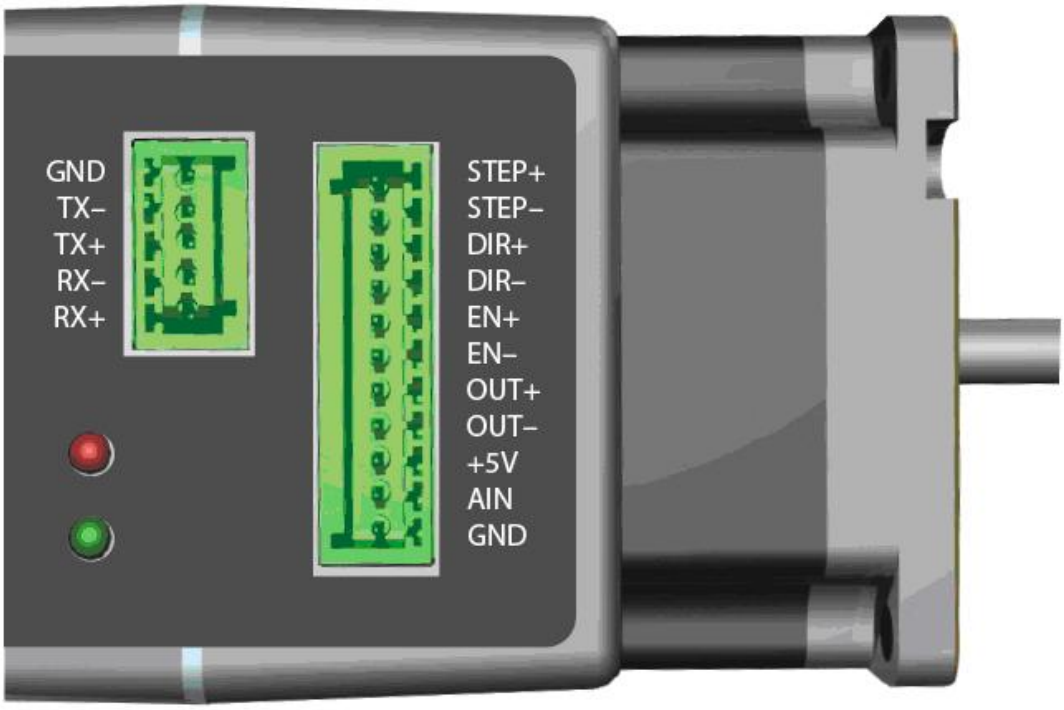

Figure C.1: LED error codes for the STM 23S-3RE

C.3 Connecting the USB-COMi-M Serial Adapter to the Stepper Motors

The stepper motors provide a two-way RS-485 interface which allows multiple devices to use a similar shared bus. The USB-COMi-M serial adapter interfaces between USB and RS-485 and is the recommended adapter by Applied Motion Products. An illustration of the wiring connections between the USB-COMi-M and a single stepper motor is provided in the following figure.

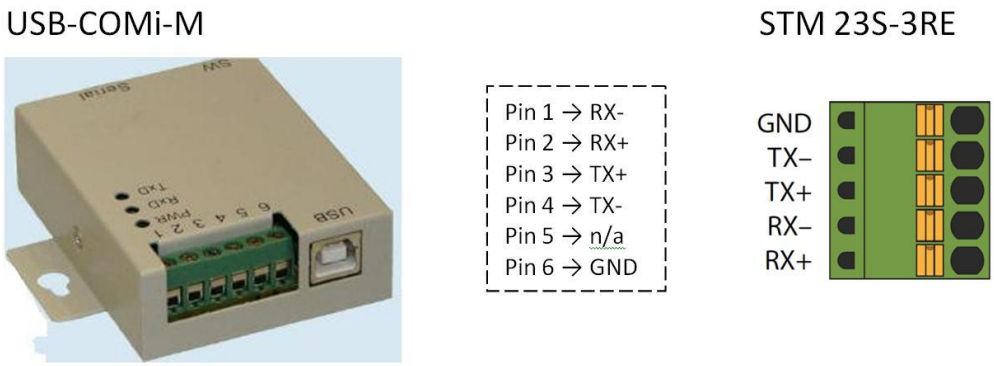

Figure C.2: Wiring the USB-COMi-M serial adapter to the STM 23S-3RE motors

C.4 Connecting Limit Switches to the Stepper Motors

Two limit switches should be installed for each motor/scanning axis: one for the CCW direction (pulling toward motor) and one for the CW direction (pushing away from motor). The following schematic illustrates the connections between a single stepper motor and two limit switches. The switches can be configured as *normally open* or *normally closed*, just be sure that the motors' *DL* setting reflects this choice. Note that the stepper motors provides a 5V output that can be used as the power supply.

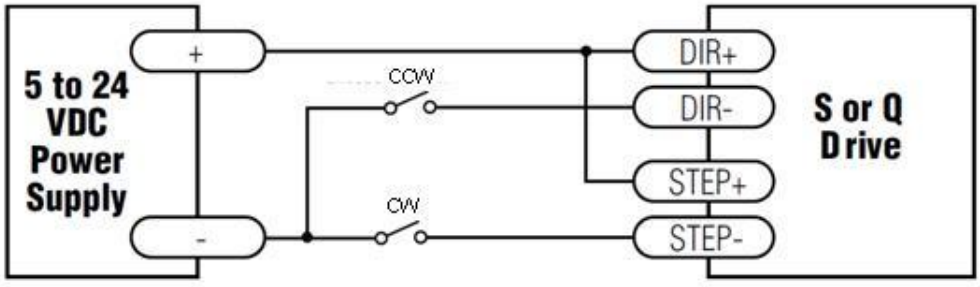

Figure C.3: Wiring the limit switches to the STM 23S-3RE motors (from Host_Command_Ref_D.pdf)

C.5 SCL Command Summary

This appendix contains a set of tables that list the more common SCL commands available with the stepper motors. The tables are divided into Motion commands, Configuration commands, I/O commands, and Immediate commands. Each table contains number of columns that give information about each command.

- "Command" provides the two-letter command code.
- "Description" provides the command name.
- "Range" provides the range of acceptable input values.
- "SA" designates which commands are saved in non-volatile memory when the SA (Save) command is sent to the motor.

These commands can also be found in the following manual:
http://www.appliedmotion.com/ampinfo/manuals/Host_Command_Ref_D.pdf

Table C.1: Motion commands

Command	Description	Range	SA
AC	Accel Rate	0.167 - 5461.167 (rps/s)	•
AM	Accel Max	0.167 - 5461.167 (rps/s)	•
CJ	Commence Jogging		
DC	Distance for FC, FM, FO, FY	0 - 2,147,483,647 (steps)	•
DE	Decel Rate	0.167 - 5461.167 (rps/s)	•
DI	Distance or Position	2,147,483,647 (steps)	•
EG	Electronic Gearing	200 - 51200 (steps/rev)	•
EP	Encoder Position	2,147,483,647 (counts)	
FD	Feed to Double Sensor	see manual	
FE	Follow Encoder	3,4; H,L,R,F	
FL	Feed to Length		
FM	Feed to Sensor with Mask Dist	1-4; H/L/R/F	
FO	Feed to Length & Set Output	1; H/L	
FP	Feed to Position		
FS	Feed to Sensor	1-4; H,L,R,F	
FY	Feed to Sensor with Safety Dist	1-4; H,L,R,F	
HW	Hand Wheel	3,4; H,L,R,F	
JA	Jog Accel rate	0.167 - 5461.167 (rps/s)	•
JC	Velocity mode second speed	0.0042 - 80 (rps)	•
JD	Jog Disable		
JE	Jog Enable		
JL	Jog Decel rate	0.167 - 5461.167 (rps/s)	•
JM	Jog Mode	1	•
JS	Jog Speed	0.0042 - 80 (rps)	•
PS	Pause		
SH	Seek Home	1-4; H,L,R,F	
SP	Set Absolute Position	2,147,483,647	
SS	Send String	up to 4 characters	
VC	Velocity for Speed Change (FC)	0.0042 - 80 (rps)	•
VE	Velocity Setting (Feed Commands)	0.0042 - 80 (rps)	•
VM	Velocity Max	0.0042 - 80 (rps)	•

Table C.2: Configuration commands

Command	Description	Range	SA
BR	Baud Rate	1 - 5	•
CC	Change Current	0 - 5.0 (amps)	•
CD	Idle Current Delay	0.00 - 10.00 (sec)	•
CF	Anti-resonance Filter Frequency	1 - 2000 (Hz)	•
CG	Anti-resonance Filter Gain	0 - 32767	•
CI	Change Idle Current	0 - 4.49 (amps)	•
CM	Control mode	1,2,7,10,11,12-18,21,22	•
DA	Define Address	see manual	•
DL	Define Limits	1, 2 or 3	•
EF	Encoder Function	0, 1, 2, or 4	
ER	Encoder Resolution	4000 (counts/rev)	•
HG	4th Harmonic Filter Gain	0 - 32767	•
HP	4th Harmonic Filter Phase	125	•
MD	Motor Disable		
ME	Motor Enable		
PB	Power up Baud Rate	1 - 5	•
PC	Power up Current	0 - 5.0 (amps)	•
PF	Position Fault	0 - 100 (%)	•
PI	Power up Idle Current	0 - 4.49 (amps)	•
PM	Power up Mode	1 - 7	•
PR	Protocol	1 - 63 (binary word)	•
SA	Save Non-Volatile Parameters		
SF	Step Filter Frequency	0 - 16000 (Hz)	•
TD	Transmit Delay	0 - 32767 (msec)	•

Table C.3: I/O commands

Command	Description	Range	SA
AD	Analog Deadband	0 - 255 (mV)	•
AF	Analog Filter	0 - 32767	•
AG	Analog Velocity Gain	32767	•
AI	Alarm Input usage	1, 2 or 3	•
AO	Alarm Output usage	1, 2 or 3	•
AP	Analog Position Gain	0 - 32767	•
AS	Analog Scaling	0 - 7	•
AT	Analog Threshold	0.000 - 5.000 (volts)	•
AV	Analog Offset	5.000 (volts)	•
AZ	Analog Zero (Auto Zero)		
BD	Brake Disengage Delay time	0 - 32.767 (sec)	•
BE	Brake Engage Delay time	0 - 32.767 (sec)	•
BO	Brake Output usage	1, 2 or 3	•
DL	Define Limits	1, 2 or 3	•
FI	Filter Input	0 - 32767 (cycles)	
MO	Motion Output	1 - 8	•
SI	Enable Input usage	1, 2, 3, 4 or 5	•
SO	Set Output	1; H or L	
WI	Wait on Input	1-4; H,L,R,F	
WT	Wait Time	0.00 - 320.00 (sec)	

Table C.4: Immediate commands

Command	Description	Range	SA
AL	Alarm Code		
AR	Alarm Reset (immediate)		
BS	Buffer Status		
CE	Comm Error		
CS	Change Jog Speed	80 (rps)	•
CT	Continue		
IA	Immediate Analog value		
ID	Immediate Distance request (hex)		
IE	Immediate Encoder request (hex)		
IF	Immediate Format	H or D	
IH	Immediate High Output	1	
IL	Immediate Low Output	1	
IO	Immediate output status request	0 or 1	
IP	Immediate position request (hex)		
IS	Input Status request		
IT	Immediate Temperature		
IU	Immediate DC Bus Voltage		
IV	Immediate Velocity	0 or 1	
IX	Immediate Position Error		
MN	Model Number		
RE	Re-start or Reset		
RL	Register Load	see manual	
RS	Request Status		
RV	Revision Level request		
SC	Request Status (hex)		
SJ	Stop Jogging		
SK	Stop & Kill Buffer		
ST	Stop Motion		

C.6 Technical Resources

STM23 Hardware Manual:
STM23_Hardware_Manual.pdf [39]
SCL Software Manual:
Host_Command_Ref_D.pdf [39]
Applied Motion Technical Support:
1-800-525-1609
support@applied-motion.com
Paper on the μASAR:
Matthew Edwards Master's Thesis [38]
"microASAR: A Small, Robust LFM-CW SAR for Operation on UAVs and Small Aircraft" [37]